A Continuum Model for Material Separation Theory and Computation

By

Andrew Tobias Baldwin
Bachelor of Science in Computational Physics (University of California in Davis) 2004
Master of Science in Physics (University of California in Davis) 2006

Dissertation

Submitted in Partial Satisfaction of the Requirements for the Degree of

Doctor of Philosophy

in

Civil and Environmental Engineering

in the

Office of Graduate Studies

of the

University of California

Davis

Approved:

Mark M. Rashid
(Chair)

Yannis F. Dafalias

Amit Kanvinde

Committee in Charge
2011

UMI Number: 3482101

UMI®
Dissertation Publishing

UMI 3482101

ProQuest®

ProQuest LLC.
789 East Eisenhower Parkway
P.O. Box 1346
Ann Arbor, MI 48106 - 1346

Dedicated to Voltron for always keeping me safe from the evil king Zarkon.

Contents

Andrew Tobias Baldwin
September 2011
Civil Engineering

A Continuum Model for Material Separation   Theory and Computation

Abstract

In this dissertation an overview of the fracture mechanics field and cohesive zone models is first provided. Discussion continues with a description of a new fracture mechanics model, the Continuum Geometric-Decohesion Model. Analytical and numerical results for an explanatory example problem are then explored in detail. A brief overview of the Finite Element Method and a related new numerical approximation method called the Partitioned Element Method is given. Next a convex subdivision algorithm (titled Half-Space Traversal Convex Subdivision) to be used with the Partitioned Element Method is explained in detail. Finally, potential avenues of research are discussed with relation to the Continuum Geometric-Decohesion Model and the Partitioned Element Method.

Acknowledgments and Thanks

I would like to acknowledge the Physics department of the University of California in Davis for the support provided me during my time in Davis. In particular want to thank Professor Richard Scalettar for the guidance and assistance given throughout my time conducting research at the Physics department, and to thank Professors David Pellett and Rena Zieve for their help launching my graduate student career. I also want to thank Norman Paris and Christopher Varney for the constructive technical discussions we shared while performing research.

I would like to thank the Civil and Environmental Engineering department of the University of California in Davis for the welcoming and care given to me while pursuing my doctorate. Specifically, I would like to thank Professor Mark Rashid for the extensive advice and aid supplied to me during my stay in the Civil and Environmental Engineering department.

Thanks to all my friends and family the good times we've shared and for making life in Davis more pleasant.

0.1   Common Mathematical Notation

In this dissertation, unless noted otherwise, the following notational scheme is used:

Boldface lower and upper case letters (e.g. $\boldsymbol{v}$ and $\boldsymbol{A}$) will distinguish vectors and 2nd-order tensors respectively. Letter sub-indices on regular typeface letters signify a component of the corresponding vector or tensor (e.g. v_i as the ith component of $\boldsymbol{v}$), and number sub-indices indicate the Cartesian direction components of the associated vector or tensor. Hatted vectors (e.g. $\hat{\boldsymbol{v}}$) will denote the unit vector of the given vector, defined by

$$\hat{\boldsymbol{v}} = \frac{\boldsymbol{v}}{||\boldsymbol{v}||} \tag{0.1}$$

where $||\boldsymbol{v}||$ is the Euclidean norm of $\boldsymbol{v}$. A regular typeface letter of the same letter as a previously defined vector indicates the Euclidean norm of the vector (i.e. $v = ||\boldsymbol{v}||$).

A sub-index comma denotes a derivative with respect to the variable that follows (where a number is shorthand for the corresponding coordinate direction), meaning

$$\boldsymbol{v}_{,a} = \frac{d\boldsymbol{v}}{da} \tag{0.2}$$

$$\boldsymbol{v}_{,1} = \frac{d\boldsymbol{v}}{dx_1} \tag{0.3}$$

A nabla will indicate a gradient operator as

$$\nabla f = \frac{\partial f}{\partial x_i}\hat{\boldsymbol{x}}_i \tag{0.4}$$

$$\nabla \boldsymbol{v} = \frac{\partial v_j}{\partial x_i}\hat{\boldsymbol{x}}_i\hat{\boldsymbol{x}}_j \tag{0.5}$$

Dotted quantities (e.g. $\dot{\boldsymbol{T}}$) specify a time derivative of the given object, such that

$$\dot{\boldsymbol{A}} = \frac{d\boldsymbol{A}}{dt} \tag{0.6}$$

Further, the Einstein summation convention is adopted, designating

$$u_i v_i = \sum_i u_i v_i \tag{0.7}$$

Thus, the Hadamard product of 2nd-order tensors (represented by $\circ$) can be given by the identity

$$\boldsymbol{A} \circ \boldsymbol{B} = A_{ij} B_{ij} \tag{0.8}$$

In addition, the determinant of a 2nd-order tensor $\boldsymbol{A}$ will be indicated by bracketing vertical bars (e.g. $|\boldsymbol{A}|$).

Finally, calligraphic letters (e.g. $\mathcal{B}$) will indicate regions (1D, 2D, or 3D) in Euclidean space, while a partial prefix before a region (e.g. $\partial\mathcal{B}$) is the boundary of that region. Bracketing vertical bars surrounding calligraphic letters (e.g. $|\mathcal{B}|$) will indicate the size of the indicated region (length, area, or volume for 1D, 2D, or 3D regions respectively).

Chapter 1

Fracture Mechanics

Material fracture is a major source of failure of many engineering systems. Imperfections in manufacture or assembly, harsh service environments, material defects, and damage in service can cause cracks to form in even the best designed parts and structures. As such, cracks are of critical concern for a host of engineering fields (including aerospace, automotive, marine, materials, nuclear, pavement, and structural engineering), and thus for the engineering systems that they support as well. Indeed, many of the catastrophic engineering failures in history were the result of fractures (Figs. 1.1-1.6 recount some of the more famous failures due to cracks). Yet, experimental approaches (sophisticated, educated trial and error) often prove too costly to be a practical approach for design. Yet scant few other options were available, as standard continuum analyses prove inarticulate when seeking to describe bodies with cracks. In response to this troubling state of affairs, many phenomenological methods have been rallied under the banner of fracture mechanics.

For a phenomenological fracture mechanics model to be universally applicable, it must be able to address both nucleation and propagation of cracks. Clearly, during typical engineering design the formation of cracks must be dissuaded at every possible turn. But, crack initiation does not necessarily lead to immediate, or even imminent, engineering failure. Worryingly, the initiation of a fracture may not even appreciably affect material performance. Moreover,

complete prevention of cracks is rarely possible in production, and practically impossible in service. Thus, further care must be taken to limit the paths and rate of propagation; this way fracture can be planned for and caught in inspection and maintenance schedules and relatively low cost repairs can be made to halt further crack extension and prevent disaster.

Regrettably, the continuum material science theories available to us produce unbounded strain and, to the extent allowed in the material model, stress fields around cusps (sharply inflected edges) in a material body. These geometrically produced infinite discontinuities are present regardless of the magnitude and form of the applied load (as long as it is finite). Any rational, physically motivated model with local rupture criteria would require every material to break down under infinite strain or stress, but standard continuum mechanics models indicate this occurs for **any** loading. As such, fracture mechanics models must either abandon a physical interpretation of the near-cusp strain and/or stress fields, provide non-local rupture criteria, or provide a means to regularize them. Without one of these augmentations an unphysical or non-predictive model would result.

Still, the standard continuum mechanical models prove usefully accurate for a wide variety of engineering bodies that do not have sharp re-entrant features. So, fracture augmentations must take care not to upset the validity of the solution at large by localizing its region of effect to the fronts of crack; ideally the stress and strain fields in most of the body are left virtually unchanged. Even if the bulk state is of little concern for an engineering application, cracks often propagate as many microcracks that coalesce into a large rupture. The interaction between the cracks must be little influenced by the fracture augmentation such that coalescence is properly modeled (making localization a key feature again).

Utilizing localized regularization or non-local rupture criteria, a fracture mechanics model can be used in conjunction with the underlying continuum model to provide a full fatigue and failure model. Such models can correctly produce both deformation as well as topological changes in the bodies being simulated (including any non-fracture damage mechanics the underlying continuum model might hold). In short, a fully functioning fracture mechanics

model must describe crack genesis and propagation while maintaining the predictive power of the continuum model it hopes to augment.

Fig. 1.1: The Versailles railway disaster occurred on May 8th, 1982 in Meudon Bellevue, France during the inauguration ceremonies of the Paris to Saint-Germain railroad. The lead car in a train was derailed after one of its axles fractured, and the ensuing crash along with the resulting fire took the lives of 55 of the travelers. This caused the Ouest railway company to stop its policy of locking their passengers into the coaches during railway travel.

Fig. 1.2: The Boston molasses flood took place in the North End neighborhood of Boston on January 15th, 1919 when a Purity Distilling Company storage tank burst open. A 40 foot wave poured through the streets, sweeping some buildings from their foundations and crushing others; the onrush of molasses killed 21 and injured 150. While the cause of failure (beyond shoddy construction) is not known for certain, evidence points to the tank being weakened (by a fatigue crack) to the point it could not bear the requisite loads.

Fig. 1.3: While working in the Ekofisk oil field on March 27th, 1980 the Norweigan semi-submersible drilling rig Alexander Kielland capsized. The drilling rig was not being used for drilling, but was operating as living quarters for offshore workers when one of the bracings cracked then failed. With no structural redundancy built into the drilling rig it quickly capsized, killing 123 of its residents.

Fig. 1.4: On April 28$^{\text{th}}$, 1988 the Boeing 737-297 used for Aloha Airlines flight 243, flying between Hilo and Honolulu in Hawaii, had the top of its first class cabin tear away. Although the plane was (incredibly) safely landed after the explosive decompression, 65 of the riders were injured and one flight attendant was blown out of the cabin. The accident was caused by a crack that formed in the fuselage and was not caught during maintenance (compounding fatigue due to corrosion resulting from exposure to salt and humidity).

Fig. 1.5: As the space shuttle Columbia re-entered the Earth's atmosphere on February 1$^{\text{st}}$, 2003 it disintegrated over Texas. During launch, 16 days earlier, a piece of foam from the main propellant tank broke off and struck the left wing of the shuttle. The thermal tiles on the left wing were ruptured, allowing the thermal protection system to fail; the left wing, and then the entire shuttle, broke apart when subjected to the heat caused by the extreme compression of gases resulting from hypersonic flight during atmospheric re-entry.

Fig. 1.6: During the evening rush hour on August 1st, 2007 the I-35W Mississippi River bridge in Minneapolis, Minnesota abruptly collapsed, killing 13 and injuring 145. The bridge's failure was attributed to understrength gusset plates that cracked, then ultimately failed catastrophically. To exacerbate the design problem, the bridge was under higher than average load due to construction taking place that day.

1.1   Continuum Mechanics Problem Statement

Consider a body geometry with reference configuration $\mathcal{B}$ that is a subset of $\mathbb{R}^3$ (it can be easily converted to $\mathbb{R}^2$ if desired) with a boundary given by

$$\partial\mathcal{B} = \partial_{\boldsymbol{p}}\mathcal{B} \cup \partial_{\boldsymbol{u}}\mathcal{B} \tag{1.1}$$

$$\varnothing = \partial_{\boldsymbol{p}}\mathcal{B} \cap \partial_{\boldsymbol{u}}\mathcal{B} \tag{1.2}$$

where $\partial_{\boldsymbol{p}}\mathcal{B}$ is the part of $\partial\mathcal{B}$ on which the Piola traction vector $\boldsymbol{p}$ is specified as $\bar{\boldsymbol{p}}$, and $\partial_{\boldsymbol{u}}\mathcal{B}$ is the part of $\partial\mathcal{B}$ on which the displacement vector $\boldsymbol{u}$ is specified as $\bar{\boldsymbol{u}}$. The the first Piola-Kirchoff stress tensor is related to the Cauchy stress by the equation

$$\boldsymbol{P}_{ij} = \boldsymbol{\sigma}_{ik} J \boldsymbol{F}_{jk}^{-1} \tag{1.3}$$

where $\boldsymbol{F}$ is the deformation gradient tensor, and the Jacobian J is the determinant of $\boldsymbol{F}$. And so the Piola traction vector is given by

$$\boldsymbol{p} = \boldsymbol{P} \cdot \boldsymbol{n} \tag{1.4}$$

The strong form of the continuum mechanics boundary value problem is

$$\nabla \boldsymbol{P}(\boldsymbol{X}) + \rho \boldsymbol{b}(\boldsymbol{X}) = 0 \qquad\qquad \forall \boldsymbol{X} \in \mathcal{B} \tag{1.5}$$

$$\boldsymbol{u}(\boldsymbol{X}) = \bar{\boldsymbol{u}}(\boldsymbol{X}) \qquad\qquad \forall \boldsymbol{X} \in \partial_{\boldsymbol{u}}\mathcal{B} \tag{1.6}$$

$$\boldsymbol{p}(\boldsymbol{X}) = \bar{\boldsymbol{p}}(\boldsymbol{X}) \qquad\qquad \forall \boldsymbol{X} \in \partial_{\boldsymbol{p}}\mathcal{B} \tag{1.7}$$

where ρ is the reference mass density of the body, $\boldsymbol{b}$ is the body force per unit mass, $\boldsymbol{n}$ is the surface normal of the boundary of the body, and $\boldsymbol{X}$ is a position in the reference configuration. A point in the reference configuration refers is related to a corresponding material location at time t through $\boldsymbol{x} = \boldsymbol{X} + \boldsymbol{u}(\boldsymbol{X}, t)$.

Let a trial space be defined as

$$\mathbb{W} = \left\{ w | w(\boldsymbol{X}) = 0 \ \forall \boldsymbol{X} \in \partial_{\boldsymbol{u}}\mathcal{B}, w \in H^1(\mathcal{B}) \right\} \tag{1.8}$$

where H^1 indicates the first Sobolev space [1.26, 1.27] that includes all functions that have an existing 1st-order weak derivative and an associated $L_2(\mathcal{B})$ norm (meaning they are square-integrable inside $\mathcal{B}$). Then the strong form equation (1.3) can be rephrased as

$$\int_{\mathcal{B}} (\boldsymbol{P} \circ \nabla \boldsymbol{w} - \rho \boldsymbol{b} \cdot \boldsymbol{w}) \, dV = \int_{\partial_{\boldsymbol{p}}\mathcal{B}} (\boldsymbol{p} \cdot \boldsymbol{w}) \, dA \qquad\qquad \forall \boldsymbol{w} \in \mathbb{W} \tag{1.9}$$

The weak form of the continuum mechanics boundary value problem (1.9) has proven invaluable for achieving solutions to continuum mechanics problems.

1.2   Elastic Fracture Mechanics

In the early 20th century, it became well recognized that loads required for failure by fracture in a tensile stress test regularly exceed those required in service by a significant margin. Quickly it became clear that the cracks present in service situations were responsible for the discrepancy; cracks act as stress concentrators, causing the stress at the front of a crack to be much larger than what would be present in the absence of a crack. By taking into account the geometry of the body, one can estimate the intensified stress strength produced by the presence of the crack(s) [1.9, 1.15, 1.28]. So, it was hoped that all one needs in order to correctly predict failure is a rupture criterion (or possibly criteria to account for different modes of fracture).

Then, using a materials science approach, the average magnitude of the intermolecular bond strength for crystalline materials was calculated. And, having assumed this as the mode of cohesion in the material, estimates for the required internal stress and/or strain needed for rupture were generated. However, taking this tack still provided a load strength needed for rupture that was many times the strength observed experimentally [1.21, 1.20, 1.25]. Moreover, in an almost paradoxical finding, it was shown that a sharp crack (one whose surface consists of two bounding surfaces with a common edge) in a continuous medium intensifies the stress by a factor of ∞ [1.30, 1.31]! Instead of dealing with this mathematical oddity, it was justified by saying an actual crack tip would have a rounded tip with the radius of curvature on the order of the intermolecular spacing for the material; the intensified stress would therefore be very large but finite. This might be considered a dangerous line of thought, since no theory of **continuum** material should be expected to model features at the molecular scale.

In fact, the failure of continuum mechanics models to well approximate the stress and strain fields around crack tips is not an especially surprising outcome. Continuum mechanics is an approximation of physical bodies that are truly made up of many discrete interacting particles, and the representation of a crack as a sharp geometric feature is an approximation

of the somewhat rough microscopic features of cracks. Moreover, experiments have shown that microscopic features typically dominate local crack shape and greatly effect overall crack propagation. Clearly, augmentation(s) of continuum theories are required to accurately predict rupture, which is an inherently microscopic process.

In an attempt to reconcile these observations, A. A. Griffith pioneered the modern field of fracture mechanics by introducing a theory of minimum energy to explain crack growth in elastic regimes [1.6, 1.7]. This approach proves useful for explaining crack growth in elastic regimes, and allows the wielder to ignore the infinite stresses and strains produced by the sharp geometry of a crack. The trick lies in rephrasing the problem in terms of energies (instead of local material response).

Now, in order to employ Griffith's approach to fracture mechanics, the energy components of the elastic body in question need to be identified. A linear-elastic body $\mathcal{B}$ (with external boundary $\partial\mathcal{B}$) includes the strain energy

$$U = \frac{1}{2} \int_{\mathcal{B}} C_{ijkl} e_{ij} e_{kl} dv \tag{1.10}$$

where $\boldsymbol{C}$ is the modulus tensor. Also included is the work being done on the system by any external agents, which is

$$W = \int_{\partial\mathcal{B}} \boldsymbol{u} \cdot \boldsymbol{t} \, da + \int_{\mathcal{B}} \boldsymbol{u} \cdot \rho\boldsymbol{b} \, dv \tag{1.11}$$

where $\boldsymbol{t}$ as the Cauchy traction vector. The Cauchy stress tensor ($\boldsymbol{T}$) is related to the Piola-Kirchoff stress tensor by

$$\boldsymbol{P} = |\boldsymbol{F}| \boldsymbol{T} \left(\boldsymbol{F}^{-1}\right)^{T} \tag{1.12}$$

wherein the deformation gradient $\boldsymbol{F} = \partial\boldsymbol{x}/\partial\boldsymbol{X}$ is used.

So, to provide a rupture criterion for Griffith's method, the principle of conservation of

energy is invoked. This implementation considers the infinitesimal extension of a pre-existing crack. The energy of the system before and after crack extension is calculated in order to determine how much the energy decreases. The formation of new exterior surfaces in a body intrinsically requires energy to occur. So, if the amount that the body's energy is decreased, dubbed the strain energy release rate

$$G = (\dot{W} - \dot{U})/\dot{A} \tag{1.13}$$

is greater than the fracture toughness of the material

$$G \geq G_{\mathrm{c}} \tag{1.14}$$

then the prospective crack extension is predicted to occur. The fracture toughness G_{c} is determined material-dependent energy absorption per. unit crack surface coefficient. For a system with linearly elastic constitutive equations Griffith's approach is commonly referred to as linear-elastic fracture mechanics, and has been used and expanded extensively within the fracture mechanics field.

If a stress and strain interpretation is still desired, then Griffith's method can be rephrased to look to the relative strength of the divergent stress fields for the determination of crack growth. To decide the relative strength of singularities in the stress field, G. R. Irwin introduced the stress intensity factor [1.12, 1.11]: the coefficient of the singular term in the functional form of the stress field. Stress intensity factors are particularly powerful because they can be universally defined for cracks that are locally planar, whether they are undergoing either a tensile loading (mode I), in-plane shear loading (mode II), or anti-plane shear loading (mode III). The general form for all stress intensity factors is

$$\sigma_{ij} = \frac{1}{\sqrt{2\pi r}} f_{ij}(\theta) \tag{1.15}$$

where r is the radial distance out from the tip/edge of the crack, and f_{ij} can have a different form for each of the loading modes. In turn, G. R. Irwin showed that the stress intensity factor and the strain energy release rate are correlated. The strain energy release rate (1.13) can in fact be written in terms of the stress intensity factors as

$$G = \frac{\kappa + 1}{2\mu} \left(\frac{1}{4} \left(K_I^2 + K_{II}^2 \right) + K_{III}^2 \right) \tag{1.16}$$

In which case the rupture criterion (1.14) similarly becomes

$$\frac{1}{4} \left(K_I^2 + K_{II}^2 \right) + K_{III}^2 \geq K_c^2 \tag{1.17}$$

Another useful approach for calculating the strain energy release rate for elastic materials (importantly, even non-linearly elastic materials) is the J-integral developed by J. R. Rice [1.18]. The J-integral is defined as

$$J = \int_{\partial \mathcal{J}} \left(\rho_U n_j - t_i u_{i,1} \right) ds \tag{1.18}$$

where the crack is straight and is moving in the $\hat{x}_j$ direction, $\partial \mathcal{J}$ is **any** closed curve starting on the bottom face and stopping on the top face (moving only through the material) that surrounds the crack tip, and $\boldsymbol{n}$ is the outward normal to the region $\mathcal{J}$.

The J-integral can prove easier to calculate than either of the aforementioned approaches in some cases, but it is particularly of use for approximating plastic deformation (which is functionally equivalent to non-linear elasticity when no unloading occurs). Moreover, if the integration path $\partial \mathcal{J}$ is sufficiently distant from expected crack extension avenues, then $\partial \mathcal{J}$ can remain static throughout the crack growth process. The static nature of the integration path greatly simplifies the calculations required during crack extension, further expanding the utility of the J-integral approach. However, since J-integral values are difficult to measure experimentally, the results are sometimes converted (using an empirical factor) to a crack

tip opening displacement calculation.

The J-integral method offers greater flexibility than its elastic fracture mechanics counterparts, and enjoys widespread adoption to this day.

1.3   Quasi-Brittle Fracture Mechanics

While linear-elastic fracture mechanics proves useful for analyzing some brittle materials, it is inapplicable for the simulation of ductile fracture. In fact, for many elastic-seeming, brittle materials it turns out that elastic fracture mechanics often produces disappointing correlations with experimental results. Clearly plasticity is a key factor in rupture, and must be accounted for in general-purpose fracture mechanics models. G. R. Irwin and E. O. Orowan independently proposed a plastic zone theory to help extend the usefulness of elastic fracture mechanics [1.10, 1.16]. Plasticity is too complicated to be implemented throughout the material body, so in both their theories a small region of plasticity is introduced only around the tip/edge of the crack in question. As an added bonus, the plastic zone can ensure that stresses at the crack tip are capped at the yield stress due to plastic deformations. Moreover, the plastic zone interpretation is widely supported by experimental data that shows ductile deformations around the tip/edge of cracks (even in many brittle materials).

The plastic zone theory introduces an energy G_p that is dissipated through plastic deformation of the material, and provides an additional energy barrier before fracture. So, the strain energy release rate (1.13) becomes

$$G = (\dot{W} - \dot{U})/\dot{A} - G_\mathrm{p} \tag{1.19}$$

Unfortunately, the amount of energy dissipation that occurs in the plastic zone is extremely difficult to calculate. To sidestep this, Irwin and Orowan showed that one can approximate the surface energy density arising from plasticity by having a surface traction applied along the crack surface. The methods and constitutive equations of brittle fracture remain

unchanged beyond the surface traction; hence, the moniker quasi-brittle fracture for these models. The adjective quasi-brittle can also be thought of as reflecting the partial adoption of plasticity into an elastic model.

Following this approach, G. I. Barenblatt attempted to model the plasticity present near crack tips/edges using localized surface traction [1.1, 1.2]. The term cohesive zone is often used to describe a phenomenological traction applied to a crack surface, and the surface tractions themselves are called cohesive or closing tractions. Barenblatt reasoned that these cohesive tractions on the crack surface were the result of intermolecular bonds; yet these bonds were extremely difficult to measure experimentally, and the stress and displacement fields are equally difficult to solve for theoretically. All is naught for not, as he posits the idea of autonomy: that the cohesive forces and fracture process must depend only on the material properties and state local to the crack front.

Under the assumption that explicit modeling of the intermolecular bonds was infeasible, Barenblatt introduced a modulus of cohesion K, toto provide a rupture criterion. The modulus of cohesion represents the resistance of the material to crack extension due to the collective force of all cohesive tractions. The formulation for crack extension is the reminiscent of Irwin's method (1.17), except that the modulus of cohesion K replaces the critical stress intensity factor K_c.

$$\frac{1}{4}\left(K_\mathrm{I}^2 + K_\mathrm{II}^2\right) + K_\mathrm{III}^2 \geq K^2 \tag{1.20}$$

Here the stress intensity factors here are related to the closing tractions rather than the fields they regularize (that will no longer have singular parts from which to derive stress intensity factors). Also, differing from the linear-elastic fracture mechanics approach, when stresses due to applied loads are less than the modulus of cohesion the intermolecular bonds will close the crack (unless irreversibility in the traction-separation law is postulated).

Shortly thereafter, D. S. Dugdale attempted to model quasi-brittle fracture with a zone of

perfect plasticity occurring around a crack front [1.5, 1.32]. He reasoned that the plastic zone that manifests around the crack tip/edge is what allows the stresses in real materials to avoid growing without bound. In the Dugdale model the crack front plastic zone is considered to extend a distance d ahead of the crack. This is achieved computationally by extending the crack the distance d (creating a crack surface extension $\partial \mathcal{D}$), adding a cohesive zone to the new surface $\partial \mathcal{D}$, and analyzing the resultant body.

In Dugdale's model the traction field is a constant value s_D taken to be the uniaxial yield stress of the bulk material across the surface $\partial \mathcal{D}$, and through it the ensuing stress field in the body is regularized. The length of the plastic zone d is determined so as to ensure the divergent stress field in the material is exactly cancelled. So, the Dugdale model provides a nicely gentle hand, and the distance d thus goes to 0 when the body is fully unloaded. The result of applying this cohesive zone is equivalent to a zone of rigid perfectly plastic material extending a distance d into the material along the path of crack extension [1.4]; to match Dugdale's conceptual intention, the area $\partial \mathcal{D}$ does not exist in the body being modeled.

Now, the Dugdale model returns us to the energy approach for its rupture criterion. To evaluate this rupture criterion the J-integral approach (1.18) is often used. While it is not exact, using the J-integral can provide a good estimate for the strain energy release rate provided that the plastic region is small compared to the region enclosed by the J-integral path Γ. As cracks progress in the body, the plastic zones tend to become larger and act increasingly dissimilar from non-linear elasticity. So, for large or extending cracks the efficacy of the J-integral approach, and the models it supports, are substantially reduced. Since crack extension is a realm the J-integral is otherwise rather well suited for, this is a particularly significant weakening.

Clearly there is still room for improvement in the fracture mechanics field, and accordingly it has grown substantially in past and recent years with many significant and novel approaches to fracture mechanics. Another classical method of note is the Hutchinson-Rice-Rosengren model, which produces an analytic asymptotic solution for fields near the crack

front using the deformation theory of plasticity [1.8, 1.19]. The continuum damage mechanics class of methods have damage parameters that are added to the constitutive equations, and these parameters provide a rupture criterion by adding strain hardening or softening. When the damage parameters reach a threshold value the allowed stress goes to zero, simulating destruction of the material [1.13, 1.14]. Another method is peridynamics, which enlists of a continuum network of 2-force members that connect all material points to each other with diminishing force as distance increases. Associated damage parameters determine when these bonds break and rupture occurs [1.22, 1.23, 1.24]. Yet another group of methods is bridging scale decomposition. They use micromechanics models for the material immediately surrounding the crack, and then link the micromechanical results to the continuum mechanics model that governs the bulk material [1.17, 1.3, 1.29]. In this dissertation however, discussion will be limited to the approach founded on the work of D. S. Dugdale and G. I. Barenblatt that was discussed in this chapter: cohesive zone models.

Bibliography

[1.1] G. I. Barenblatt. On equilibrium cracks formed in brittle fracture. *Doklady Akademii Nauk Soyuz Sovetskikh Sotsialisticheskikh Respublik (Presidium of the Russian Academy of Sciences)*, 127:47–50, 1959.

[1.2] G. I. Barenblatt. The mathematical theory of equilibrium cracks in brittle fracture. *Advances in Applied Mechanics*, 7:55–129, 1962.

[1.3] J. Q. Broughton, F. F. Abraham, N. Bernstein, and E. Kaxiras. Concurrent coupling of length scales: Methodology and application. *Physical Review B*, 60:2391–2403, 1999.

[1.4] F. Costanzo and D. H. Allen. A continuum thermodynamic analysis of cohesive zone models. *International Journal of Engineering Science*, 33:2197–2219, 1995.

[1.5] D. S. Dugdale. Yielding of sheets containing slits. *Journal of the Mechanics and Physics of Solids*, 8:100–104, 1960.

[1.6] A. A. Griffith. The phenomena of rupture and flow in solids. *Philosophical Transactions of the Royal Society of London, Series A, Containing Papers of a Mathematical or Physical Character*, 221:163–198, 1921.

[1.7] A. A. Griffith. The theory of rupture. *Proceedings of the 1st International Congress of Applied Mechanics*, pages 55–63, 1924.

[1.8] J. W. Hutchinson. Singular behavior at end of a tensile crack in a hardening material. *Journal of the Mechanics and Physics of Solids*, 16:13–31, 1968.

[1.9] C. E. Inglis. Stresses in a plate due to the presence of cracks and sharp corners. *Transactions of the Institution of Naval Architects*, 55:219–230, 1913.

[1.10] G. R. Irwin. Fracture dynamics. *Proceedings of the American Society for Materials Symposium on Fracturing of Metals*, pages 147–166, 1948.

[1.11] G. R. Irwin. Analysis of stress and strain near the end of a crack traversing a plate. *Journal of Applied Mechanics*, 24:361–364, 1957.

[1.12] G. R. Irwin. Relation of stresses near a crack to the crack extension force. *Proceedings of the 9th International Congress of Applied Mechanics*, pages 245–251, 1957.

[1.13] L. M. Kachanov. On the time to rupture under creep conditions. *Izvestiya Rossiiskoi Akademii Nauk (Bulletin of the Academy of Science of Russia)*, 8:26–31, 1958.

[1.14] L. M. Kachanov. Rupture time under creep conditions. *Problems of Continuum Mechanics*, pages 202–218, 1961.

[1.15] N. I. Muskhelishvili. Sur l'intégtation de l'Équation biharmonique (on the integration of the biharmonic equation). *Izvestiya Rossiiskoi Akademii Nauk (Bulletin of the Academy of Science of Russia)*, 13:663–686, 1919.

[1.16] E. O. Orowan. Fundamentals of brittle behaviour in metals. *Conference on Fatigue and Fracture of Metals at the Massachusetts Institute of Technology*, pages 139–167, 1950.

[1.17] H. Rafii-Tabar, L. Hua, and M. Cross. A multi-scale atomistic-continuum modelling of crack propagation in a two-dimensional macroscopic plate. *Journal of Physics: Condensed Matter*, 10:2375–2387, 1998.

[1.18] J. R. Rice. A path independent integral and the approximate analysis of strain concentration by notches and cracks. *Journal of Applied Mechanics*, 35:379–386, 1968.

[1.19] J. R. Rice and G. F. Rosengren. Plane strain deformation near a crack tip in a power-law hardening material. *Journal of the Mechanics and Physics of Solids*, 16:1–12, 1968.

[1.20] W. Rosenhain and S. L. Archbutt. On the inter-crystalline fracture of metals under prolonged application of stress. *Proceedings of the Royal Society of London A*, 96:55–68, 1919.

[1.21] W. Rosenhain and D. Ewen. The inter-crystalline cohesion of metals. *Journal of the Institute of Metals*, 10:119–139, 1913.

[1.22] S. A. Silling. Reformulation of elasticity theory for discontinuities and long-range forces. *Journal of the Mechanics and Physics of Solids*, 48:175–209, 2000.

[1.23] S. A. Silling, M. Epton, O. Weckner, J. Xu, and E. Askari. Peridynamic states and constitutive modeling. *Journal of Elasticity*, 88:151–184, 2007.

[1.24] S. A. Silling and R. B. Lehoucq. Convergence of peridynamics to classical elasticity theory. *Journal of Elasticity*, 93:13–37, 2008.

[1.25] A. G. Smekal. Technische festigkeit und molekulare festigkeit (technical strength and molecular sterngth). *Naturwissenschaften (The Science of Nature)*, 10:799–804, 1922.

[1.26] S. L. Sobolev. Sur un théorème d'analyse fonctionnelle (on a theorem of functional analysis). *Matematicheskii Sbornik*, 4:471–497, 1938.

[1.27] S. L. Sobolev. On a theorem of functional analysis. *American Mathematical Society Translations*, 34:39–68, 1963.

[1.28] G. I. Taylor and A. A. Griffith. The use of soap films in solving torsion problems. *Proceedings of the Institution of Mechanical Engineers*, 93:755–789, 1917.

[1.29] G. J. Wagner and W.-K. Liu. Coupling of atomistic and continuum simulations using a bridging scale decomposition. *Journal of Computational Physics*, 190:249–274, 2003.

[1.30] K. Wieghardt. Über da spalten und zerreissen elastischer körper (on splliting and cracking of elastic bodies). *Zeitschrift für Mathematik und Physik (Journal of Mathematics and Physics)*, 55:60–103, 1907.

[1.31] K. Wieghardt, A. Sommerfeld, and H. P. Rossmanith. On splitting and cracking of elastic bodies. *Fatigue and Fracture of Engineering Materials and Structures*, 18: 1371–1405, 1995.

[1.32] Y. P. Zheltov and S. A. Khristianovitch. On the mechanism of hydraulic fracturing of an oil-bearing stratum. *Izvestiya Akademii Nauk Soyuz Sovetskikh Sotsialisticheskikh Respublik (Bulletin of the Academy of Science of the USSR)*, 5:3–41, 1995.

Chapter 2

Cohesive Zone Models

The cohesive zone models derive their name from the closing traction that they apply to the existing crack surfaces in an engineering body. Generally speaking, closing tractions are phenomenological rather than physical tractions, and cannot be measured experimentally. However, they are indispensable supplements for modeling fracture within continuum theories. One possible interpretation for closing tractions is that they are a mechanism to transfer stresses between the crack surfaces. Such connections actually occur in crack regions that consist of many microvoids separated from each other by remaining connecting fibers. Another possible interpretation is that regions with cohesive tractions represent an approximation of particular forms of plastic zones that occur near crack fronts. Often these interpretations fall short, however, for they do not represent the extent and versatility of which cohesive zone models are capable or they do not acknowledge the inherent weakness in continuum models that closing tractions attempt to fix.
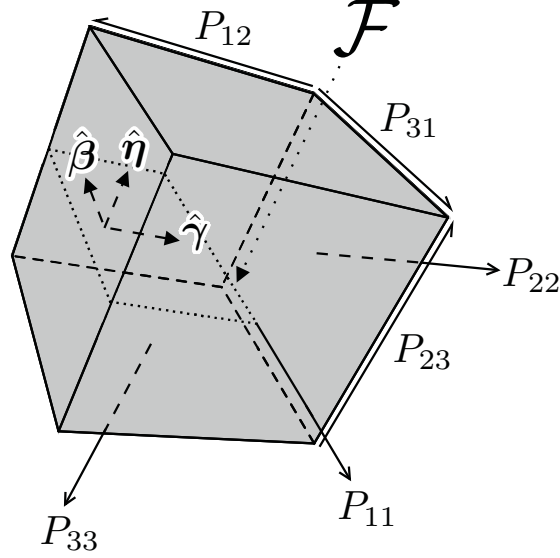
2.1   Fracture Definition

Fig. 2.1: An infinitesimal piece of a body $\mathcal{B}$ that contains a fracture $\mathcal{C}$ represented in its reference
configuration. While a cube and edge crack are used for clarity, the infinitesimal piece of
the body and the crack within it can take any shape in practice.

To describe fracture mechanics models that modify the properties of crack surfaces, a stan-
dard crack surface definition must be created. For clarity, a body $\mathcal{B}$ with a single crack front
will be considered here, but the development can be extended to multiple cracks if desired.
Now, in the reference configuration, let the given body have an exterior boundary $\mathcal{E}$ and an
interior boundary $\mathcal{C}$ (which is the considered crack surface). Before fracture, the exterior
boundary will be the entire body boundary, such that

$$\partial \mathcal{B} = \mathcal{E} \tag{2.1}$$

Let the part of the crack surface boundary that lies within the body in the reference config-
uration be called the crack front $\mathcal{F}$. The crack front thus has the properties

$$\mathcal{E} \cap \mathcal{F} = \varnothing \tag{2.2}$$

and

$$\mathcal{F} \subseteq \partial \mathcal{C} \tag{2.3}$$

where the crack front or tip is the entire crack-surface boundary for cracks that are contained
within the interior of a body. So, the body's boundary in the deformed configuration is given
as

$$\partial \mathcal{B} = \mathcal{E} \cup (\mathcal{C} \backslash \partial \mathcal{C}) \cup \mathcal{F} \tag{2.4}$$

Next, let the condition

$$\boldsymbol{X} \in (\mathcal{C} \backslash \mathcal{F}) \qquad\qquad \forall t > \tau \tag{2.5}$$

for all points

$$\boldsymbol{X} \in (\mathcal{C} \backslash \mathcal{F}) \qquad\qquad t = \tau \tag{2.6}$$

be imposed on the crack surface in the reference configuration, where t is the time of evalua-
tion. This condition enforces the common expectation that no portions of the crack surface
recombine, and that no material transfers from one side of a crack to the other. However,
the crack front in this description is allowed to change in time. As the crack extends, the
crack front will move through the body, changing position and shape as it bounds the new
crack surface. So, the space that was formerly part of the crack front will become part of the

crack surface, and will no longer be able to change in time in the reference configuration.

At a position $\boldsymbol{X}$ on the crack front, let the local surface normal at a position $\boldsymbol{X}$ on the crack surface be given by $\boldsymbol{\eta}(\boldsymbol{X})$. Here, the sign of the surface normal can be chosen by any scheme, so long as $\hat{\boldsymbol{\eta}}$ is continuous on $\mathcal{C}$. The local in-plane unit vectors at a point $\boldsymbol{X}$, denoted by $\hat{\boldsymbol{\gamma}}(\boldsymbol{X})$ and $\hat{\boldsymbol{\beta}}(\boldsymbol{X})$, are perpendicular to each other, and are both perpendicular to $\hat{\boldsymbol{\eta}}(\boldsymbol{X})$. Here, the vector $\hat{\boldsymbol{\gamma}}$ will be chosen such that it points in the direction of the path along the crack surface with the minimum distance to the crack front. For notational simplicity the local surface direction vectors subscripts will be used as

$$v_\gamma = \boldsymbol{v} \cdot \hat{\boldsymbol{\gamma}} \tag{2.7}$$

Finally, let the expression $\mathcal{C}(a)$ represent the region of the crack surface where the minimum distance along the crack surface to the crack front is a. Thus, the expression $\mathcal{C}(0)$ is equivalent to the crack front $\mathcal{F}$.

Now, to have a single surface in the reference configuration describe a full crack surface, further stipulations must be made. A crack surface in the deformed configuration can be described as two material surfaces that share a common boundary line, namely the crack front $\mathcal{F}$. To accommodate two surfaces in the deformed configuration as one surface in the reference configuration, the stress and displacement fields in the reference configuration need to be dual-valued on $\mathcal{C}$; one value of each field on each side of the crack surface. As such, the limits

$$\lim_{h \to 0^\pm} \boldsymbol{T}(\boldsymbol{X} + h\hat{\boldsymbol{\eta}}, t) \to \boldsymbol{T}^\pm(\boldsymbol{X}, t) \qquad \forall \boldsymbol{X} \in \mathcal{C} \tag{2.8}$$

$$\lim_{h \to 0^\pm} \boldsymbol{u}(\boldsymbol{X} + h\hat{\boldsymbol{\eta}}, t) \to \boldsymbol{u}^\pm(\boldsymbol{X}, t) \qquad \forall \boldsymbol{X} \in \mathcal{C} \tag{2.9}$$

must be obeyed, such that the dual value found on the crack surface be based on the direction of approach.

So, the stress and displacement fields must be allowed to have a step discontinuity across

$\mathcal{C}$. However, since the fields at the crack front must be continuous, it is required that

$$\boldsymbol{u}^+(\boldsymbol{X}) - \boldsymbol{u}^-(\boldsymbol{X}) = \boldsymbol{0} \qquad\qquad \forall \boldsymbol{X} \in \mathcal{F} \qquad\qquad (2.10)$$

$$\boldsymbol{T}^+(\boldsymbol{X}) - \boldsymbol{T}^-(\boldsymbol{X}) = \boldsymbol{0} \qquad\qquad \forall \boldsymbol{X} \in \mathcal{F} \qquad\qquad (2.11)$$
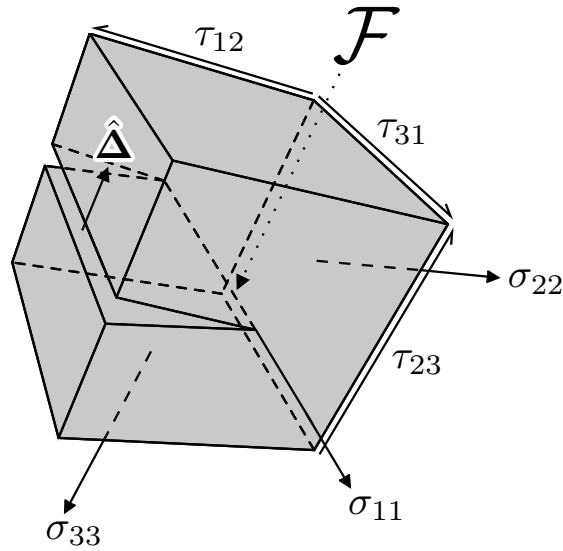
2.2   Closing Tractions

Fig. 2.2: An infinitesimal piece of a body $\mathcal{B}$ that contains a fracture $\mathcal{C}$ represented in its deformed configuration. While a cube and edge crack are used for clarity, the infinitesimal piece of the body and the crack within it can take any shape in practice.

Like the stress and displacement fields, the closing tractions $\boldsymbol{s}^\pm(\boldsymbol{X})$ in a classical cohesive zone model must be dual valued on $\mathcal{C}$. The spatial dependence of the closing tractions used in classical cohesive zone models varies greatly from model to model, but all depend on the gap vector

$$\boldsymbol{\Delta} = \boldsymbol{u}^+ - \boldsymbol{u}^- \qquad\qquad (2.12)$$

The form of the closing tractions' dependence on the gap vector typically defines the properties of a classical cohesive zone model, and will be discussed in Section 3.1. Here, some of the general properties of and restrictions on closing tractions will be explored.
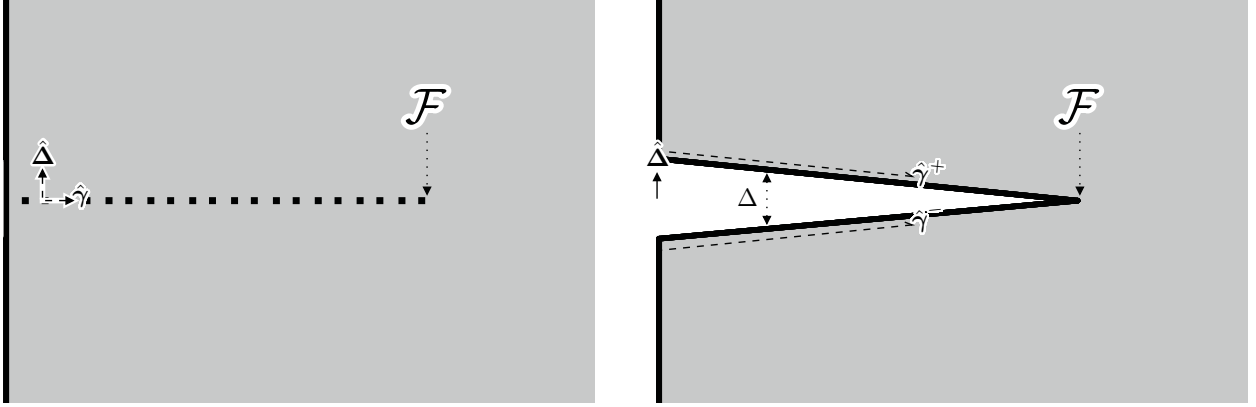

Fig. 2.3: A planar slice of an infinitesimal piece of a body $\mathcal{B}$ containing a fracture $\mathcal{C}$ in the reference configuration (left) and deformed configuration (right). While a triangular shaped fracture in a cube is used for clarity, the infinitesimal piece and the fracture it contains could take any shape in practice.

Now, within cohesive zone models a cohesive zone is applied to each crack in the body considered and the provided closing tractions regularize the stress and displacement field solutions as necessary. The regularization is enforced for any and every imposed load by having constant(s) in the functional form of the closing traction that depend on the material state. Determining these constant(s) requires analysis of the the closing tractions and the fields produced by them for a range of functional forms. This is rarely a trivial process; typically numerical methods must be employed to determine the exact form of the closing traction for a given set of loads. Full analysis can mean that point load kernel functions must be integrated to produce the relationship between material state and closing traction. Further, the process of picking regularizing closing tractions becomes more difficult as more cohesive zones are added and the interplay between sets of closing tractions becomes significant. As a result, selective insertion of cohesive zones can be critical in achieving feasible computational runtimes.

Still, there are a few physically motivated restrictions that are applied to cohesive zone closing tractions that help simplify their creation and use. First, it is desired that there be no resultant force on the body produced by the closing tractions. A reasonable restriction since fractured objects do not start moving without an external net force. For this purpose, it is sufficient but not necessary that the cohesive traction obeys

$$\boldsymbol{s}^- = -\,\boldsymbol{s}^+ \tag{2.13}$$

Further, it is desired that there be no resultant moment on the body produced by the closing tractions. Similar to before, this restriction is reasonable since fractured objects do not start rotating without an external net torque. Now, it is sufficient but not necessary that the cohesive tractions obey

$$\boldsymbol{s}^\pm \times \boldsymbol{\Delta} = \boldsymbol{0} \tag{2.14}$$

So, the formulation is given by

$$\boldsymbol{s}^+ = s\hat{\boldsymbol{\Delta}} \tag{2.15}$$

It is also desired that the closing tractions resist the separation of the crack surfaces, such that the stability of the problem is ensured. So, it is required that the closing tractions obey

$$s \leq 0 \tag{2.16}$$

In addition, it is often desired that the stress field in the body does not change discontinuously in time when rupture occurs. So, the closing tractions immediately after rupture

need be defined as

$$\lim_{t \to t_c^+} \boldsymbol{T}^{\pm}(\boldsymbol{X}, t) \to \boldsymbol{T}(\boldsymbol{X}, t) \qquad\qquad \forall \boldsymbol{X} \in \mathcal{C} \qquad\qquad (2.17)$$

where t_c is the time of crack initiation.

Next, for a physical body the closing tractions must be material frame indifferent. As such, the minimum restriction is that cohesive tractions must remain unchanged under rigid translation and rotation [2.15]. This means that all closing tractions must at least obey

$$s(\boldsymbol{\Delta}) = s(\boldsymbol{Q}\boldsymbol{\Delta}) \qquad\qquad \forall \boldsymbol{Q} \in \left\{ \boldsymbol{Q} | \boldsymbol{Q}\boldsymbol{Q}^T = 1 \right\} \qquad\qquad (2.18)$$

Finally, it is desired that the closing tractions should be dissipative during a closed cycle of external loading on the body. A reasonable restriction as energy conservation requires that no body should be able to produce indefinite amounts of energy. The energy dissipated by closing tractions is typically considered to go into micro-mechanical processes (e.g. heat) that are associated with fracture and are not explicitly accounted for by the continuum model. This is a much more difficult problem to define, since the form of the constitutive equations for the material play a significant role in the conditions for energy conservation to be upheld. As such, it is usually necessary to explore this restriction on a case by case basis, but it can typically be formulated along the lines of

$$\int_t^{t+\tau} \int_{\mathcal{C}} \left(\boldsymbol{s}^+ \cdot \boldsymbol{u}^+ + \boldsymbol{s}^- \cdot \boldsymbol{u}^- \right) da\, dt \geq 0 \qquad\qquad (2.19)$$

where $[t, t + \tau]$ is the time period required for a single cycle to occur. While not a strict physical condition, the energy restriction is a useful exploratory test for the viability of a cohesive zone model.

To be clear, it is not required that all cohesive zone closing tractions follow the restrictions (2.13) and (2.15) while external forces and moments are applied. In fact, there are some

augmentations to traditional cohesive zone formulations that reject (2.15), since the resulting closing tractions cannot simulate anistropic material behavior [2.5]. Moreover, since cohesive zone models are phenomenological in nature, they do not necessarily need to follow any of the aforementioned restrictions (or even any physical law) to produce viable results. Yet, these conditions are still frequently useful when examining cohesive zone models as telling exploratory tests for their viability.
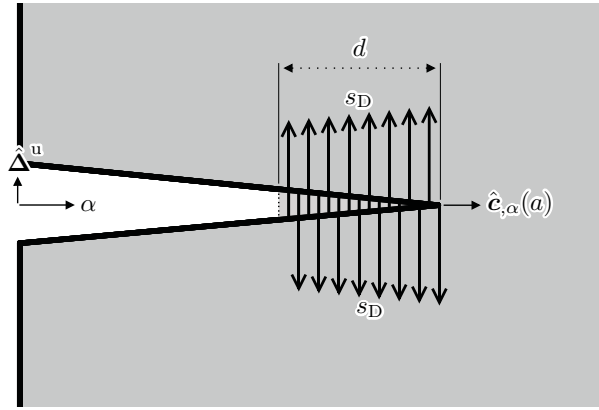
2.3 Classical Cohesive Zone Models

Fig. 2.4: A planar slice of an infinitesimal piece of the body $\mathcal{B}$ containing a fracture $\mathcal{C}$ in the deformed configuration. Along the crack surface the Dugdale closing tractions are depicted.

Now, phrasing the closing traction of the Dugdale model (Section 1.3) in preceding terminology language results in

$$\boldsymbol{s}^{\pm}(\boldsymbol{X}) = \begin{cases} \mp s_{\mathrm{D}}\hat{\boldsymbol{\Delta}} & \boldsymbol{X} \in \{\boldsymbol{X}|\boldsymbol{X} \in \mathcal{C}(\gamma), \gamma \in [0, d)\} \\ 0 & \text{else} \end{cases} \tag{2.20}$$

where d is the length of the plastic zone past the crack tip and s_{D} is the yield stress of the rigid perfectly plastic material being modeled in the plastic zone. The length of the plastic zone d is determined by calculating the stress field created by the closing tractions, then

calibrating the length until the singularity produced by the closing tractions exactly cancels the singular stress that exists in the body [2.7, 2.23].

Clearly the conditions (2.13), (2.15), (2.16), and (2.18) are all satisfied by the Dugdale model. The Dugdale model specifies the entire bulk as linearly elastic (although in some areas the linear elasticity is simulating perfect plasticity) and the closing traction is not history-dependent. Thus, any cyclic external load will not result in energy gain or loss and the condition (2.19) is also met (within the realm of applicability for this model). The time continuity condition (2.17) is ill-posed in this case, since there is no clear rupture criterion proposed with the Dugdale model. So, the Dugdale model behaves satisfactorily within its domain of applicability (and it has proven its usefulness during its lifetime of application).

For modern approaches it is still often the case that closing tractions are posited before-hand [2.3, 2.4, 2.18], and may not be an approximation of material features (e.g. plasticity) around the crack front. One such formulation produced by G. T. Camacho and M. Ortiz [2.4] is defined such that when the body being considered is undergoing loading the closing tractions are

$$s_\eta^\pm = \mp T_\eta \left(1 - \frac{\Delta_\eta}{\Delta_{\mathrm{cr}}} \right) \tag{2.21}$$

$$s_\gamma^\pm = \mp T_\gamma \frac{\Delta_\eta}{\Delta_{\mathrm{cr}}} \, \mathrm{sgn}\,(\Delta_\gamma) \tag{2.22}$$

$$s_\beta^\pm = \mp T_\beta \frac{\Delta_\eta}{\Delta_{\mathrm{cr}}} \, \mathrm{sgn}\,(\Delta_\beta). \tag{2.23}$$

And when the crack faces undergo unloading the closing tractions are

$$s_\eta^\pm = \mp T_\eta \left(1 - \frac{\Delta_i}{\Delta_{\mathrm{cr}}} \right) \frac{\Delta_\eta}{\Delta_i} \tag{2.24}$$

$$s_\gamma^\pm = \mp T_\gamma \left(1 - \frac{\Delta_i}{\Delta_{\mathrm{cr}}} \right) \frac{\Delta_\eta}{\Delta_i} \mathrm{sgn}\,(\Delta_\gamma) \tag{2.25}$$

$$s_\beta^\pm = \mp T_\beta \left(1 - \frac{\Delta_i}{\Delta_{\mathrm{cr}}} \right) \frac{\Delta_\eta}{\Delta_i} \mathrm{sgn}\,(\Delta_\beta) \tag{2.26}$$

where Δ_{cr} is the material dependent critical crack separation length (crack separation greater than the critical crack separation indicating complete fracture) and Δ_i is the value of Δ_η when the unloading process last began. Complete fracture in this case means that the closing tractions are absent and will not return. So, parts of the crack that are completely fractured can no longer be interpreted as sections of the body with approximated material properties. The initial closing traction strengths T_η, T_γ, and T_β are material constants that are determined by the user, according the nature of the cohesive zone approximation desired. When the body undergoes loading after unloading, the closing tractions follow the form they took while unloading until Δ_i is again reached.
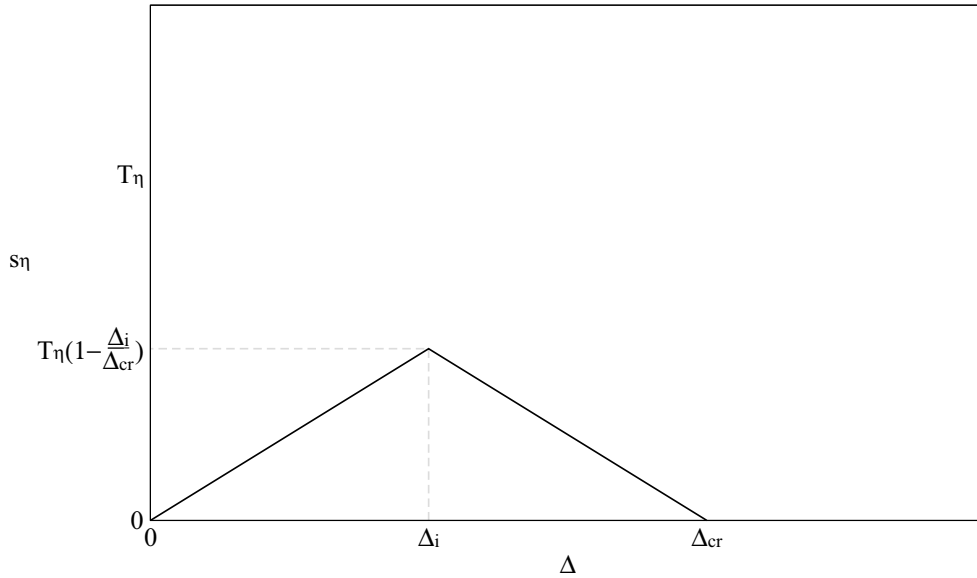

Fig. 2.5: An example traction-separation plot for the Camacho-Ortiz closing tractions (2.21)-(2.26). Here a crack has been previously loaded until the separation Δ_i has been achieved, and is now being loaded again such that the crack is taken all the way to complete fracture.

While it is apparent that this closing traction only satisfies conditions (2.13) and (2.16) generally, qualitative agreement with experimental results [2.8, 2.12] is still achieved. As mentioned earlier, this is not a surprising result, but it does help to illuminate the potential

danger in taking a physical interpretation of cohesive zones too far. Physical interpretations can provide useful insight and facilitate understanding of cohesive zone models and/or the phenomena they attempt to reproduce. However, restricting cohesive zones to those with physical interpretations will eliminate useful closing traction formulations.

It is worthwhile to note that the Camacho-Ortiz closing tractions (2.21)-(2.26) include a material dependent length scale Δ_{cr}, which determines some of the material response characteristics. Later, the concept of such a tunable parameter was termed the characteristic length [2.9]. This is not simply a mathematical tool or a way to rephrase the critical strain energy release rate, but a method to represent important material properties [2.14, 2.1, 2.13]. Specifically, when the geometry of a body is uniformly scaled up, the required traction boundary conditions to induce fracture do not stay constant (as continuum mechanics would suggest). Instead, the required load for rupture can scale down and fracture becomes possible with relatively, or even absolutely, lower applied loads. So, the characteristic length provides a scale against which to describe this scaling effect for continuum mechanics models. It can be considered a result of the type of micromechanical process(es) that occur around a crack front that ultimately lead to material separation.

Another, more complicated, set of closing tractions introduced by M. Ortiz and A. Pandolfi [2.18] is defined using an effective opening displacement

$$\Delta_{\text{eff}} = \sqrt{\Delta_\eta^2 + \lambda^2 \left(\Delta_\gamma^2 + \Delta_\beta^2 \right)} \tag{2.27}$$

where λ is a calibration constant to be decided for the material and application at hand. There is an associated history variable which is defined at time t as

$$\Delta_{\text{max}}(t) = \max_{t_{\text{h}}} \Delta_{\text{eff}}(t_{\text{h}}) \qquad\qquad t_{\text{h}} \in [\tau, t] \tag{2.28}$$

where τ is the time of crack initiation.

Now, the closing tractions are given by

$$s_\eta^\pm = \mp T(\Delta_\text{eff}) \frac{\Delta_\eta}{\Delta_\text{max}} \tag{2.29}$$

$$s_\gamma^\pm = \mp T(\Delta_\text{eff}) \lambda^2 \frac{\Delta_\gamma}{\Delta_\text{max}} \tag{2.30}$$

$$s_\beta^\pm = \mp T(\Delta_\text{eff}) \lambda^2 \frac{\Delta_\beta}{\Delta_\text{max}} \tag{2.31}$$

where the function T is given by

$$T(\Delta) = \begin{cases} T_\text{cr} \left(1 - \frac{\Delta}{\Delta_\text{cr}}\right) & \Delta < \Delta_\text{cr} \\ 0 & \Delta \geq \Delta_\text{cr} \end{cases} \tag{2.32}$$

Here T_cr and Δ_cr are also calibration constants to be decided for the given material and application.
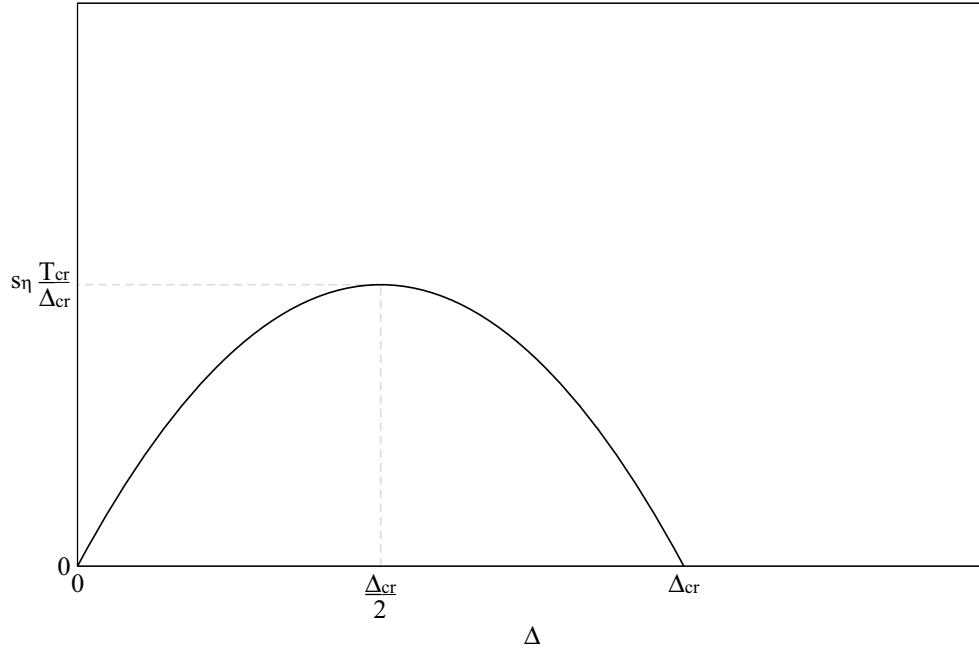

Fig. 2.6: An example traction-separation plot for the Ortiz-Pandolfi closing tractions (2.29)-(2.31). Here a crack is initiated, then loaded until complete fracture is achieved.

Next, the strong discontinuity approach [2.2, 2.21, 2.17, 2.10] has also been introduced,

which builds a cohesive zone model that does not create the closing tractions in an ad hoc manner. Instead, the displacement is separated into a continuous and discontinuous part as

$$\boldsymbol{u}(\boldsymbol{X}) = \boldsymbol{u}^{\mathrm{c}}(\boldsymbol{X}) + H(\boldsymbol{X})\boldsymbol{u}^{\mathrm{d}}(\boldsymbol{X}) \tag{2.33}$$

where $H_{\mathcal{C}}(\boldsymbol{X})$ is the unit step function defined by

$$H_{\mathcal{C}}(\boldsymbol{X}) = \begin{cases} 1 & \forall \boldsymbol{X} \in \{\boldsymbol{X} | \boldsymbol{X} + h\hat{\boldsymbol{\eta}} \in \mathcal{C}, h \leq 0\} \\ 0 & \text{else} \end{cases} \tag{2.34}$$

This means the strain can be written as

$$\boldsymbol{\epsilon}(\boldsymbol{X}) = \boldsymbol{\epsilon}^{\mathrm{c}}(\boldsymbol{X}) + H_{\mathcal{C}}(\boldsymbol{X})\boldsymbol{\epsilon}^{\mathrm{d}}(\boldsymbol{X}) + \delta_{\mathcal{C}}(\boldsymbol{X})\boldsymbol{u}^{\mathrm{d}}(\boldsymbol{X}) \tag{2.35}$$

where $\delta_{\mathcal{C}}(\boldsymbol{X})$ is defined by

$$\delta_{\mathcal{C}}(\boldsymbol{X}) = \begin{cases} \infty & \forall \boldsymbol{X} \in \mathcal{C} \\ 0 & \text{else} \end{cases} \tag{2.36}$$

with the property

$$\int_{\mathcal{B}} \delta_{\mathcal{C}}(\boldsymbol{X}) \, dv = 1 \tag{2.37}$$

such that a semblance of the Dirac delta distribution is achieved [2.17].

Unfortunately, an infinite strain is problematic for any model that has a direct relationship between the stress and strain fields; the stress will become the unphysical value of infinity along every crack surface. To alleviate this problem, a damage parameter is added to the constitutive equations of the material to induce strain softening. The damage parameter

d is introduced in the manner

$$\boldsymbol{\sigma} = \frac{1}{d}\boldsymbol{E}\boldsymbol{\epsilon} \qquad\qquad\qquad d\left(\boldsymbol{\sigma}\right) \in [d_0, \infty] \qquad\qquad (2.38)$$

where $\boldsymbol{\sigma}$ is the Cauchy stress tensor, $\boldsymbol{E}$ is Young's modulus, $\boldsymbol{\epsilon}$ is the Cauchy strain tensor, and d_0 is a finite constant determined by the material. As the strain increases, the stress will also increase, then the material will damage by d growing in a manner dependent on the particular strong discontinuity approach. So, through the relationship given in (2.38) the increase the damage parameter will cause the Cauchy stresses to be reduced. Thus, the damage parameter provides a feedback loop to keep the stresses finite (with a maximum dependent on the form of softening that occurs in the material). In this case, any fracture will require $d \to \infty$ along the crack surface in order to keep the stresses finite. Infinite damage along a crack surface is thus interpretable as complete fracture (although no topological changes take place).

However, in this formulation $\delta_{\mathcal{C}}(\boldsymbol{X})$ needs to be approximated by using

$$\delta_{\mathcal{C}}(\boldsymbol{X}) = \begin{cases} 1/k & \forall \boldsymbol{X} \in \{\boldsymbol{X} | \boldsymbol{X} + h\hat{\boldsymbol{\eta}} \in \mathcal{C}, |h| \leq k\} \\ 0 & \text{else} \end{cases} \qquad (2.39)$$

while maintaining the property

$$\int_{\mathcal{B}} \delta_{\mathcal{C}}\left(\boldsymbol{X}\right) dv = 1 \qquad\qquad (2.40)$$

This formulation prevents strong discontinuity models from having arbitrary strains at every crack surface (which would allow for strain to occur without loading). If the definition (2.36) were used, then every fracture would cause the damage parameter d to become infinite as well, and there would no longer be a definable relationship between stress and strain along the crack surfaces. Thus, the interpreted limit of complete fracture is not attainable within

the strong discontinuity model.

One interpretation of this formulation is that the stress on either side of this delta function are the closing tractions, and the material within the approximated Dirac delta is outside the body (a complete fracture has occurred there). But, since no topology changes are occurring, it is perhaps better to interpret material within the approximate Dirac delta function as a manifestation of rupturing material that immediately precedes ductile fracture [2.16, 2.20]. Still, the preferred interpretation is that the discontinuous region reduces to a cohesive zone formulation with the form of the closing tractions decided by the constitutive equations, along with the added softening parameter. In essence, the strong discontinuity approach follows the reverse path of the Dugdale model, where a set of closing tractions can be mapped to perfectly plastic constitutive behavior [2.6].

A proof of the a one-to-one correspondence between the strong discontinuity approach and the cohesive zone approach has been put forward [2.17]. This is not surprising, as any region of physically manifestable material (regardless of the severity of the finite strain it suffers) will transfer stresses from one side of its boundaries to another, and these stresses can be interpreted as closing tractions if desired. Still, there is no guarantee that all constitutive models will provide derived closing tractions that will be useful, or that they will follow the previously suggested (2.13), (2.15), (2.16), (2.17), (2.18), and (2.19) conditions. Fortunately a base of elastic constitutive equations has shown working results when augmented by the strong discontinuity approach [2.10].

Clearly, the exact form of the closing tractions can simulate a variety of material responses. Properly chosen closing tractions can approximate complicated fracture behavior that may be too difficult to implement in the bulk material. And all formulations of closing tractions can regularize the stress field to produce meaningful results.

2.4   Rupture Criterion

With the closing tractions defined in cohesive zone models, the fields in the body are properly regularized when cracks appear in the material. Yet, even with such regularized fields, the question remains: how do cracks initiate, and then propagate, in the material? In the case of cohesive zone models, the closing tractions are considered to be the force that holds the material together. The rupture criterion and the closing tractions are inexorably intertwined. Because of this no rupture criterion can be independently specified.

Since rupture is dependent only on the properties of the closing tractions, it is sometimes considered that rupture occurs when stress, greater than that provided by the closing tractions for crack surfaces with zero Δ, occurs at a point in the body. In practice there are many complications that can arise when ensuring time continuity or allowing arbitrary crack growth paths to occur in the body. Regarding these complications, there are two general cases of traction-separation laws to consider.
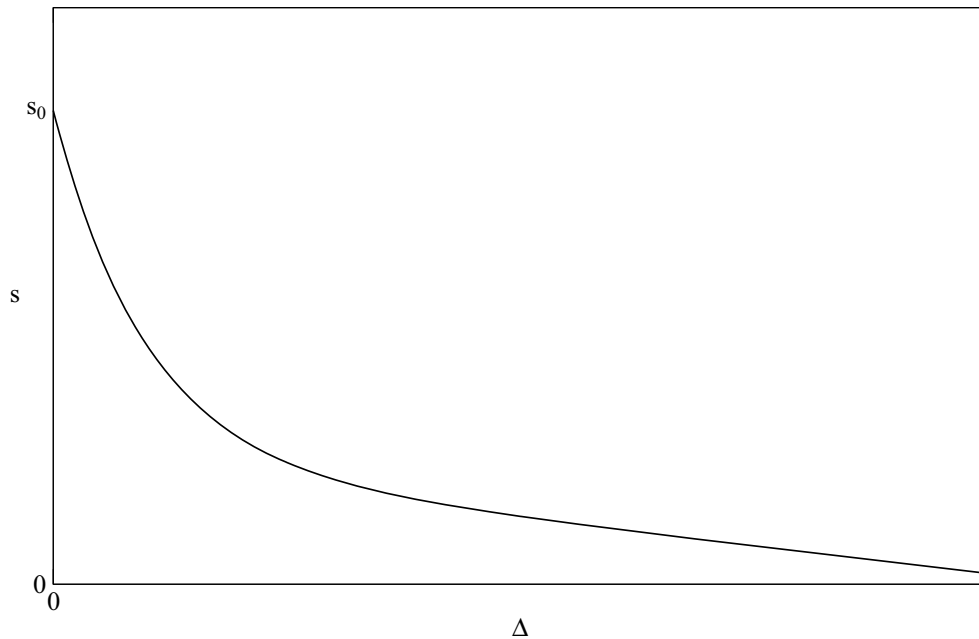

Fig. 2.7: An example initially rigid traction-separation law with initial closing traction strength s_0.

First, consider the functional form of s with respect to the magnitude of separation Δ; this

is termed the traction-separation law. Initially rigid traction-separation laws define $s \to s_0$ as $\Delta \to 0$ (Fig. 2.7), where s_0 is some finite constant. Problematically, this approach breaks down for dynamic prlbems (or where small time steps are otherwise needed) regardless of the rest of the form of the traction-separation law. Consider a situation where separation occurs and is followed by an immediate unloading of the body. The closing tractions must go to $\mathbf{0}$ in order to preserve the stability of the problem. As the time between fracture and unloading goes to zero, the stiffness of the crack face must in turn increase indefinitely. This is especially troublesome because the high stiffness cohesive tractions introduce high natural frequencies into the problem, complicating numerical solutions. These high natural frequencies lead to high frequency oscillations that can cause rapid deterioration of crack surface stiffness through quickly completed loading cycles (Fig. 2.8).
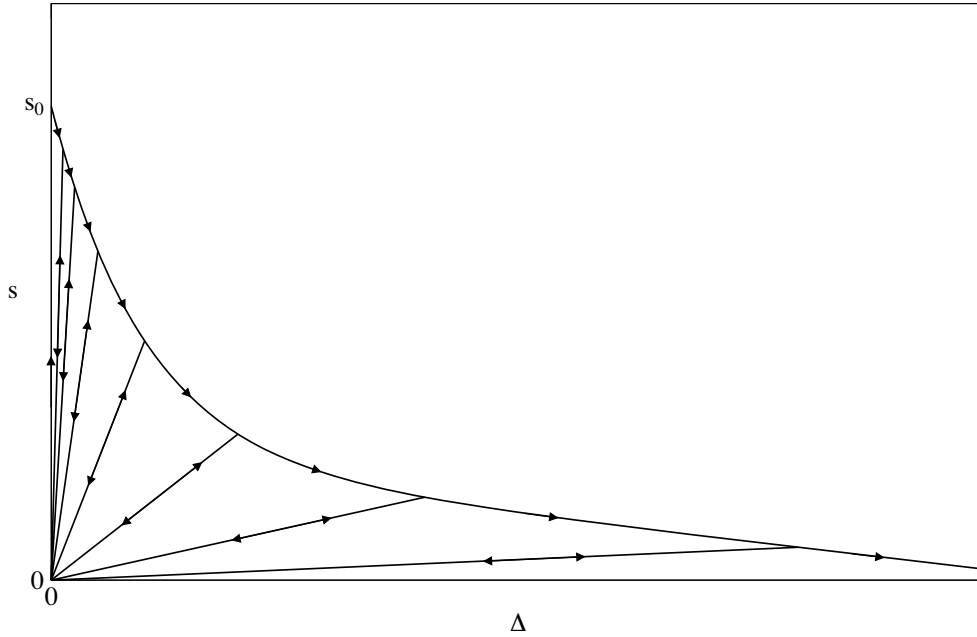

Fig. 2.8: An example load path for the traction-separation law (Fig. 2.7) that undergoes many loading cycles. The arrows indicate the (un)loading progression with time. The initial stiffness is quite large, but decreases towards 0 as time progresses.

In addition, an initially rigid traction-separation law can suffer a phenomenon known as

traction locking [2.19]. This occurs for any two- or three-dimensional initially rigid formulation that ensures time continuity and has an effective rupture criterion

$$\sqrt{(1-\lambda)\boldsymbol{T}_{\hat{m}\hat{\eta}}^2\left(\boldsymbol{X}\right) + \lambda\left(\boldsymbol{T}_{\hat{\gamma}\hat{\gamma}}^2\left(\boldsymbol{X}\right) + \boldsymbol{T}_{\hat{\beta}\hat{\beta}}^2\left(\boldsymbol{X}\right)\right)} \geq \left.s\right|_{\Delta\to 0} \qquad \boldsymbol{T}_{\hat{\eta}\hat{\eta}}\left(\boldsymbol{X}\right) \geq 0 \qquad (2.41)$$

$$\sqrt{-\lambda\boldsymbol{T}_{\hat{\eta}\hat{\eta}}^2\left(\boldsymbol{X}\right) + \lambda\left(\boldsymbol{T}_{\hat{\gamma}\hat{\gamma}}^2\left(\boldsymbol{X}\right) + \boldsymbol{T}_{\hat{\beta}\hat{\beta}}^2\left(\boldsymbol{X}\right)\right)} \geq \left.s\right|_{\Delta\to 0} \qquad \boldsymbol{T}_{\hat{\eta}\hat{\eta}}\left(\boldsymbol{X}\right) < 0 \qquad (2.42)$$

where, for notational brevity, the expression

$$\boldsymbol{v}\cdot\left(\boldsymbol{T}\boldsymbol{v}\right) = \boldsymbol{T}_{\boldsymbol{v}\boldsymbol{v}} \qquad (2.43)$$

has been used.

Time continuity means that the stress and displacement fields along a new crack surface are continuous in time throughout the rupture process. When traction locking takes place, the cohesive traction will be forced to act to increase the displacement across the fracture. Thus, initially rigid closing tractions that obey (2.17) do not obey (2.16). Further, immediately after a rupture involving shear stress, tensile stress that promotes interpenetration of the crack surfaces begins, and exacerbates the unphysical simulation results.
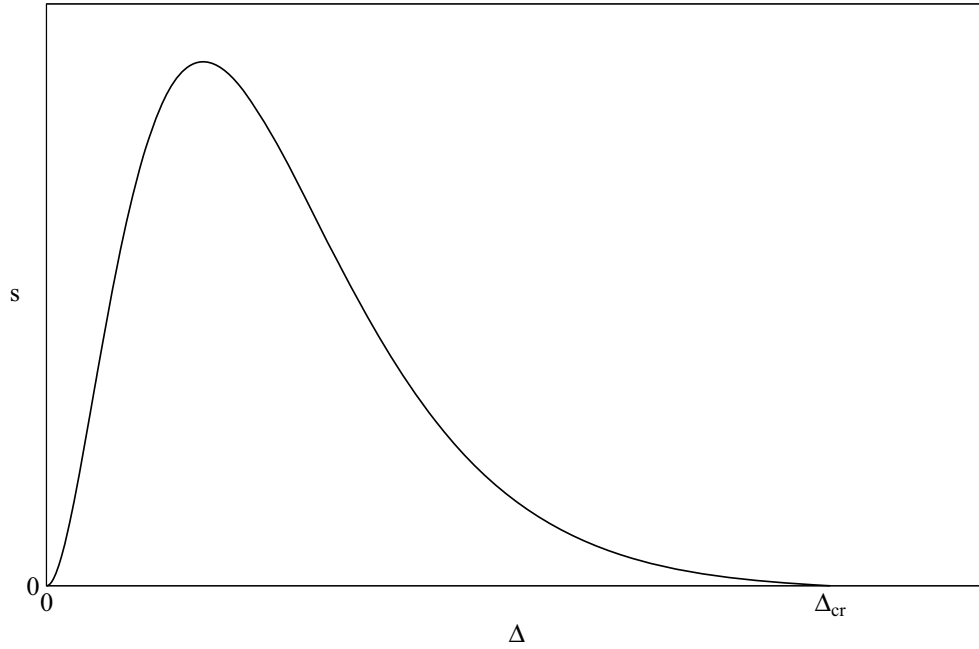
Fig. 2.9: An example initially elastic traction-separation law with critical crack separation length Δ.

On the other hand, an initially elastic traction-separation law (Fig. 2.9) has $s \to 0$ as $\Delta \to 0$. Unfortunately, this approach breaks down when arbitrary crack growth is allowed, regardless of the rest of the form of the traction-separation law. An initially elastic traction-separation law's zero traction strength at zero separation means every interface will be pulled apart by any finite stress that arises in the material. If all possible potential crack faces are considered, then the body will dissemble into a host of cracks with the slightest loading. In other words, the stiffness of the material decreases with the number of potential crack faces considered; as the number of potential crack faces approaches infinity the material stiffness approaches zero

In order to mitigate this problem, only a select number of potential interfaces are typically considered. In particular, it can be shown that the Young's modulus of the material

transforms as

$$E \to E \frac{1}{1 + \frac{E}{kd_i}} \tag{2.44}$$

where d_i is the average spacing between considered crack surfaces and k is the initial slope of the traction-separation law [2.11]. So, in order to maintain the stiffness of the material within an initially elastic simulation, the relationship

$$d_i k \gg E \tag{2.45}$$

should be satisfied. However, since the Young's modulus is determined by the bulk material, and the initially slope of the traction-separation law is formulated to model the fracture properties, this requirement is often essentially $d_i \to \infty$. Initially elastic traction-separation laws are still useful in cases where the avenues of crack progress are well known and few (e.g. by symmetry), but that is a severe limitation in the applicability of the cohesive zone model for design purposes.

Further, there is some subtlety to the limitations produced when few potential crack surfaces are considered. Beyond the potential lack of spatial resolution to find the precise location of a crack, it is crucial to be able to have fine angular resolution in the surface normal defining a potential crack plane. It has been shown that the number and variety of outward surface normals considered for potential crack surface planes strongly influences the form of the crack produced, and this pitfall is largely indifferent to spatial resolution [2.22]. With greater angular resolution required, the restriction of coarse-grained potential crack surfaces worsens, rendering most complicated problems intractable.

Cohesive zone models have proven and continued successes as fracture simulation models. However, the limitations on traction-separation laws has provided strict restrictions on how cohesive zone models can be used. These limitations are no small matter, as they are applied to the earlier limitation that the closing tractions must regularize the fields within

the material. Then, from within the remaining traction-separation law possibilities, desired material behaviors must often be integrated into the closing tractions. Clearly there is room for improved flexibility and hope for a greater control of the descriptive power of both closing tractions and rupture criterion.

Bibliography

[2.1] Z. P. Bažant. Scaling theory for quasibrittle structural failure. *Proceedings of the National Academy of Sciences of the United States of America*, 101:13400–13407, 2004.

[2.2] R. D. Borst, L. J. Sluys, H.-B. Mühlhaus, and J. Pamin. Fundamental issues in finite element analyses of localization of deformation. *Engineering Computations*, 10:99–121, 1993.

[2.3] B. Budiansky, J. C. Amazigo, and A. G. Evans. Small-scale crack bridging and the fracture toughness of particulate-reinforced ceramics. *Journal of the Mechanics and Physics of Solids*, 36:167–187, 1988.

[2.4] G. T. Camacho and M. Ortiz. Computational modelling of impact damage in brittle materials. *International Journal of Solids and Structures*, 33:2899–2938, 1996.

[2.5] F. Costanzo. A continuum theory of cohesive zone models: Deformation and constitutive equations. *International Journal of Engineering Science*, 36:1763–1792, 1998.

[2.6] F. Costanzo and D. H. Allen. A continuum thermodynamic analysis of cohesive zone models. *International Journal of Engineering Science*, 33:2197–2219, 1995.

[2.7] D. S. Dugdale. Yielding of sheets containing slits. *Journal of the Mechanics and Physics of Solids*, 8:100–104, 1960.

[2.8] W. L. Fourney, D. C. Holloway, and J. W. Dally. Fracture initiation and propagation from a center of dilatation. *International Journal of Fracture*, 11:1011–1029, 1975.

[2.9] A. Hillerborg, M. Modér, and P.-E. Petersson. Analysis of crack formation and crack growth in concrete by means of fracture mechanics and finite elements. *Cement and Concrete Research*, 6:773–782, 1976.

[2.10] A. E. Huespe, J. Oliver, M. D. G. Pulido, S. Blanco, and D. Linero. On the fracture models determined by the continuum-strong discontinuity. *International Journal of Fracture*, 137:211–229, 2006.

[2.11] P. A. Klein, J. W. Foulk, E. P. Chen, S. A. Wimmer, and H. Gao. Physics-based modeling of brittle fracture: Cohesive formulations and the application of meshfree methods. Technical Report 8099, Sandia National Laboratories, 2000.

[2.12] B. Lawn and R. Wilshaw. Indentation fracture: Principles and applications. *Journal of Materials Science*, 10:1049–1081, 1975.

[2.13] R. Maranganti and P. Sharma. Length scales at which classical elasticity breaks down for various materials. *Physical Review Letters*, 98(195504):1–4, 2007.

[2.14] R. E. Miller and V. B. Shenoy. Size-dependent elastic properties of nanosized structural elements. *Nanotechnology*, 11:139–147, 2000.

[2.15] A. I. Murdoch. On material frame-indifference. *Proceedings of the Royal Society of London A*, 380:417–426, 1982.

[2.16] A. Nadai. *Plasticity: A Mechanics of the Plastic State of Matter*. McGraw-Hill, 1931.

[2.17] J. Oliver, A. Huespe, M. D. G. Pulido, and E. Chaves. From continuum mechanics to fracture mechanics: The strong discontinuity approach. *Engineering Fracture Mechanics*, 69:113–136, 2002.

[2.18] M. Ortiz and A. Pandolfi. Finite-deformation irreversible cohesive elements for three-dimensional crack-propagation analysis. *International Journal for Numerical Methods in Engineering*, 44:1267–1282, 1999.

[2.19] K. D. Papoulia, C.-H. Sam, and S. A. Vavasis. Time continuity in cohesive finite element modeling. *International Journal for Numerical Methods in Engineering*, 58: 679–701, 2003.

[2.20] J. R. Rice. The localization of plastic deformation. *Proceedings of the 14th International Congress on Theoretical and Applied Mechanics*, pages 207–220, 1976.

[2.21] J. C. Simo, J. Oliver, and F. Armero. An analysis of strong discontinuities induced by strain-softening in rate-independent inelastic solids. *Computational Mechanics*, 12: 277–296, 1993.

[2.22] M. G. A. Tijssens, L. J. Sluys, and E. V. D. Giessen. Numerical simulation of quasi-brittle fracture using damaging cohesive surfaces. *European Journal of Mechanics A/Solids*, 19:761–779, 2000.

[2.23] Y. P. Zheltov and S. A. Khristianovitch. On the mechanism of hydraulic fracturing of an oil-bearing stratum. *Izvestiya Akademii Nauk Soyuz Sovetskikh Sotsialisticheskikh Respublik (Bulletin of the Academy of Science of the USSR)*, 5:3–41, 1995.

Chapter 3

The Continuum Geometric-Decohesion Model

The continuum geometric-decohesion model was developed in an attempt to address many of the shortcomings of other (particularly cohesive) fracture mechanics models. A key feature of the continuum geometric-decohesion model is that it does not couple the regularization and fracture processes. This feature alone provides the flexibility necessary for the continuum geometric-decohesion model to tackle some of the challenges that all fracture mechanics models must face.

3.1   Rupture Criterion

The crux of the continuum geometric-decohesion model is its rupture criterion, the feature that ultimately gives the model the ability to predict rupture. A rupture variable Θ is introduced, given by

$$\Theta = \Theta(\mathbb{S}(\boldsymbol{X}), \hat{\boldsymbol{\eta}}) \tag{3.1}$$

where $\mathbb{S}$ symbolically represents the material state at the given physical location $\boldsymbol{X}$ in the reference configuration, and $\hat{\boldsymbol{\eta}}$ is the unit normal to a potential local rupture plane. To allow for freedom of crack genesis and propagation, all points in the body and every material surface are considered potential rupture surfaces. To be sure, specifying planar crack formations and extensions with a well defined unit normal does not prevent an arbitrary crack path, since the extent of crack growth is infinitesimal. The exact form of Θ is left purposefully unspecified here, and will be created such that the fracture properties of the material body are properly captured. Those that implement the continuum geometric-decohesion model can and must decide what functional form they will give to the rupture variable.

When evaluating the rupture variable at any point, it must be checked against the condition

$$\Theta(\mathbb{S}(\boldsymbol{X}), \boldsymbol{\eta}) \leq 1 \tag{3.2}$$

where equality indicates fracture should be initiated at $\boldsymbol{X}$, on the surface with normal $\hat{\boldsymbol{\eta}}$ (thereby changing the topology of the body).
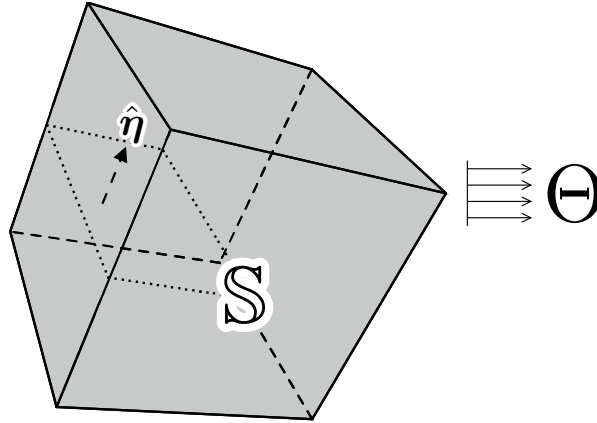

Fig. 3.1: An arbitrary infinitesimal piece of the body $\mathcal{B}$ being considered for crack development (growth or initiation) by generating a rupture variable value for the material state and potential crack plane.

Now, if an initially inelastic traction-separation law rupture criterion (as in Section 2.4) is desired, then the rupture variable is simply

$$\Theta = \frac{\hat{\boldsymbol{\eta}} \cdot \boldsymbol{T} \hat{\boldsymbol{\eta}}}{T_{\mathrm{cr}}} \tag{3.3}$$

where T_{cr} is the stress magnitude that must be achieved for fracture to occur. Next, if the material model were to be modified such that heated sections of the material were less likely to fracture, then a rupture variable like

$$\Theta = \exp\left(Q_{\mathrm{ref}} - Q\right) \frac{\hat{\boldsymbol{\eta}} \cdot \boldsymbol{T} \hat{\boldsymbol{\eta}}}{T_{\mathrm{cr}}} \tag{3.4}$$

could be adopted, where Q is the local temperature of the material and Q_{ref} is a reference temperature. When $Q \to Q_{\mathrm{ref}}$ the rupture variable (3.4) will be the same as (3.3). This would be a difficult feature to implement if closing tractions were linked with the rupture criterion. Yet the stress state need not be directly involved in the rupture variable function; instead the strain could be used as

$$\Theta = \frac{\hat{\boldsymbol{\eta}} \cdot \boldsymbol{e} \hat{\boldsymbol{\eta}}}{e_{\mathrm{cr}}} \tag{3.5}$$

where $\boldsymbol{e}$ is the Eulerian strain tensor and e_{cr} is the strain magnitude that must be reached for fracture to occur. This way the constitutive model will play a large role in mapping the rupture variable back to a stress formulation (if so desired). The possibility of using strain as a part of the rupture criterion is not common in fracture mechanics models, and is generally impossible to implement within cohesive zone models.

The continuum-geometric decohesion model allows the rupture criteria to be defined in a straightforward manner: when a critical condition occurs, relative to a candidate rupture surface, the material comes apart. Now, for the rupture criterion (3.2) to be usable for whichever constitutive model the continuum geometric-decohesion model is applied, the fields

in the body must be regularized. To regularize the fields, a closing traction is introduced on the crack surfaces, but in a manner that is quite distinct from existing cohesive zone models. In particular, the rupture criterion is not directly dependent on the bulk constitutive model, but depends only on the state parameters that the bulk constitutive model provides.

3.2   Closing Tractions

The closing traction in the continuum geometric-decohesion model is defined by the geometry of the crack it is applied to, as to be completely divorced from the material properties and constitutive equations that apply in the bulk continuum. So, using the crack description laid out in Section 2.1, the regularizing closing traction is of the general form

$$\boldsymbol{s}^{\pm} = \mp \boldsymbol{p} \tag{3.6}$$

where $\boldsymbol{p}$ is a vector that will be defined. Thus, the traction distribution will always resist the expansion of the crack, and conditions (2.13) and (2.16) are satisfied. This formulation also ensures that the closing traction requirement (2.18), that insists the traction remains unchanged under rigid rotations, is met.

Now, the traction distribution is to be localized around the crack tip such that, primarily, the divergent portions of the stress and strain fields are effected. For this purpose, $\boldsymbol{p}$ is chosen as to minimize the function $\Sigma_{\mathrm{c}}(\boldsymbol{p})$ given by

$$\Sigma_{\mathrm{c}}(\boldsymbol{p}) = \int_{\mathcal{C}} [\overline{\boldsymbol{\nabla}} p_i \overline{\boldsymbol{\nabla}} p_i + \alpha^2 p_i p_i] \, da \tag{3.7}$$

where

$$\overline{\boldsymbol{\nabla}} p_i = \boldsymbol{\nabla} p_i - [\hat{\boldsymbol{\eta}} \cdot \boldsymbol{\nabla} p]_i \hat{\boldsymbol{\eta}} \tag{3.8}$$

and α is a calibration parameter. Expanding Σ_c, it can be shown that

$$\Sigma_\text{c}(\boldsymbol{p}) = \int_{\partial\mathcal{C}} [p_i \overline{\boldsymbol{\nabla}} p_i] \cdot d\boldsymbol{l} + \int_{\mathcal{C}} [\alpha^2 p_i p_i - p_i \overline{\boldsymbol{\nabla}}^2 p_i] \, da \tag{3.9}$$

Now, the closing traction design calls for all components of $\boldsymbol{p}$ to decrease in magnitude as the point of evaluation moves away from the crack front, requiring $p_i \overline{\boldsymbol{\nabla}} p_i$ to be negative. Thus, by construction one must have

$$\int_{\partial\mathcal{C}} [p_i \overline{\boldsymbol{\nabla}} p_i] \cdot d\boldsymbol{l} \leq 0 \tag{3.10}$$

and so

$$\Sigma_\text{c}(\boldsymbol{p}) \leq \int_{\mathcal{C}} p_i [\alpha^2 p_i - \overline{\boldsymbol{\nabla}}^2 p_i] \, da \tag{3.11}$$

And since (3.7) shows Σ_c to be positive definite, (3.11) gives rise to the differential equation

$$\overline{\boldsymbol{\nabla}}^2 p_i = \alpha^2 p_i \tag{3.12}$$

that constrains the traction distribution. This differential equation bears strong similarities to Poisson's equation, and expectations can be drawn from the extensive knowledge associated with that equation. So, it can be expected that as the closing tractions are evaluated increasingly far from the crack front, (3.12) will enforce exponential decay in the magnitude of the closing tractions.

The variable α that was introduced in (3.7) is an inverse length-scale calibration parameter, or inverse characteristic-length, and as such it can be adjusted to tune results to a particular material. By raising α, the traction distribution can be increasingly localized around the crack front. And by lowering α, the traction distribution becomes more diffuse. In the extremums $\alpha \to 0$ and $\alpha \to \infty$, the closing tractions cover the entire surface and are

entirely constrained to the crack front, respectively. The calibration parameter α is the only possible link between the closing tractions and the material properties, and in particular provides a connection to the scaling effect discussed in Section 2.2.

The closing tractions are not quite fully defined yet, since they lack a boundary condition to pair with (3.12). In order to maintain independence from the specifics of the material body being modeled, the boundary condition required is chosen as

$$\lim_{a \to 0} \left| \left(\overline{\boldsymbol{\nabla}} \boldsymbol{\Delta}_i \right) \cdot \hat{\boldsymbol{\gamma}} \right|_{\boldsymbol{X} \in \mathcal{C}(a)} \to 0 \tag{3.13}$$

which requires the crack surfaces to smoothly come together at the crack front. This requirement is necessary and sufficient for regularized, finite stresses at the crack front, and throughout the body in linear-elastic materials (as proposed by Y. P. Zheltov and S. A. Khristianovich [3.2], then shown by G. I. Barenblatt [3.1]). Proof for other constitutive models is generally much more difficult to show, and cannot be done in a truly general manner. However, the boundary condition (3.13) has been observed to produce finite stresses in practice.
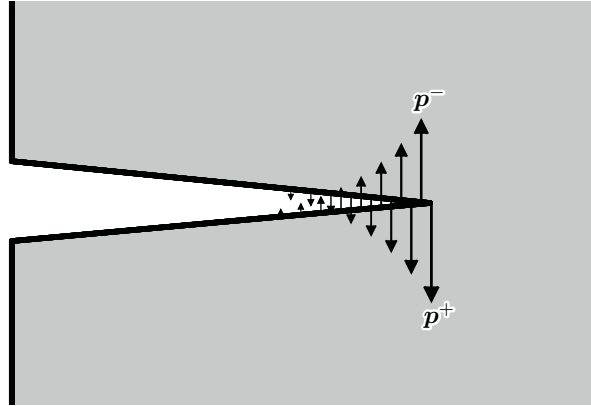

Fig. 3.2: A planar slice of an infinitesimal piece of the body $\mathcal{B}$ containing a fracture $\mathcal{C}$ in the deformed configuration. Along the crack surface one possible version of the closing tractions $\boldsymbol{p}$ (with a finite, non-zero α) is depicted.

The closing tractions previously described are completely divorced from the rupture criterion. This feature is powerful for a variety of reasons, with the first being the flexibility of regularization. The only necessary restriction on the closing tractions are the regularization of the fields, the enforcement of which is guaranteed by (3.13). Another feature is the ability to take into account the scaling effect (which would not naturally fit within any continuum theory) through the calibration parameter α.

The flexibility afforded by to the closing tractions is taken advantage of in (3.12). If another partial differential equation proves to provide faster or more accurate results than (3.12), then it could be directly inserted into the continuum geometric-decohesion model with no other changes required. The partial differential equation here is chosen for based on linearity and simplicity, while still preventing overly large and sharply peaked closing tractions.

This concludes the overview of all the necessary machinery to apply the continuum geometric-decohesion model to a ccontinuum model of solid mechanics. The succinctness with which the continuum geometric-decohesion model can be stated originates from its design. The model serves to provide a rupture criterion by which the topology of a material body can be changed, and to regularize the fields in the material body such that they remain finite as the crack front is approached. The goal is that these features should blend seamlessly into whichever constitutive model they are applied.

3.3   Distinctions from Cohesive Zone Models

There are similarities that tempt the thought of equivalence between the continuum-geometric decohesion model and cohesive zone models. However, while the distinctions may not be particularly numerous, they are particularly significant.

The closing tractions in cohesive zone models are descriptive in nature. They describe how the material fractures, are often built to describe material properties (plastic zones, fracture-

bridging filaments, etc.), and regularize the fields present. In the continuum-geometric deco-hesion model the closing tractions serve the primary purpose of regularizing the fields, with a secondary feature of describing the scaling effect. This is why the defining equations of the closing traction are based upon the geometry of the material body considered.

The rupture variable is another key distinction from cohesive zone models. The closing tractions defined by $\boldsymbol{p}$ can be thought of as initially elastic, but the continuum geometric-decohesion model need not suffer from coarse-grained potential crack mesh problems that initially elastic cohesive zone models face (Section 2.4). Instead the continuum geometric-decohesion model has a stand-alone rupture criterion that need not be tied to any feature of the closing tractions (or material model if so desired).

In traditional cohesive zone models, the rupture criterion is tied in a complicated manner to closing tractions, and producing a desired rupture criterion is a difficult task to manage while ensuring the closing tractions also regularize the fields inside the body in a numerically desirable way. Moreover, there are many classes of rupture criteria like (3.5), available to the continuum geometric-decohesion that are effectively excluded by the cohesive zone formulation. And there are many such prohibited formulations that would have no other conceivable reason for exclusion beyond the connection to the closing tractions.

So, while cohesive zone models as a whole bear some resemblance to the continuum geometric-decohesion model, there are key distinctions. And it is the disconnect between rup-ture criteria and closing tractions that allows all of the significant distinctions present. The connections (both in the creation of and practical application of the continuum geometric-decohesion model) to cohesive zone models should not be forgotten, but they do not amount to equivalence.

Bibliography

[3.1] G. I. Barenblatt. On the conditions of finiteness in the continuum mechanics: Static problems of elasticity. *Prikladnaya Matematika I Mekhanika (Applied Mathematics and Mechanics)*, 24:316–322, 1960.

[3.2] Y. P. Zheltov and S. A. Khristianovitch. On the mechanism of hydraulic fracturing of an oil-bearing stratum. *Izvestiya Akademii Nauk Soyuz Sovetskikh Sotsialisticheskikh Respublik (Bulletin of the Academy of Science of the USSR)*, 5:3–41, 1995.

Chapter 4

Applying the Continuum Geometric-Decohesion Model

The continuum geometric-decohesion model opens up a wide variety of unexplored avenues in fracture mechanics. However, before looking for new results, it is important to ensure the continuum geometric-decohesion model can reproduce already known results. For this purpose an analytic solution is obtained for the continuum geometric-decohesion model applied to a linear-elastic model problem and a comparison is made with standard linear-elastic fracture mechanics. In addition, a Finite Element Method method solution is obtained using the continuum geometric-decohesion model applied to a J2 elastic-plastic (with isotropic, power-law hardening) model problem.

4.1   A Finite Crack in an Infinite 2D Plane
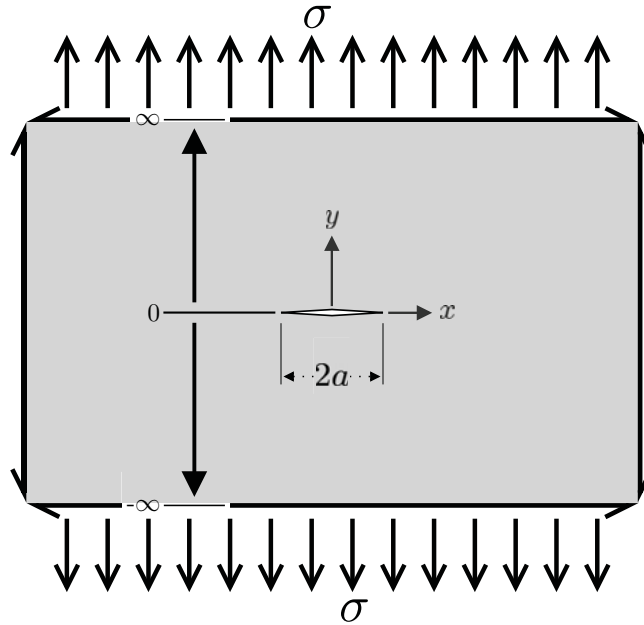
Fig. 4.1: A finite representation of a center-cracked infinite two dimensional plane with far-field uniaxial loading.

A model problem is examined to demonstrate some of the characteristics of the continuum geometric-decohesion model. A simple linearly elastic problem is chosen, that is amenable to analytic solution, consisting of a straight finite crack (of length $2a$) in an infinite two dimensional plane (Fig. 4.1). The material plane is subject to uniaxial normal loading (of magnitude σ) applied at the edges of the plate ($y \to \pm\infty$) perpendicular to the crack direction. The origin of the Cartesian coordinate system used in solving this problem is placed at the center of the crack.

As a fundamental solution upon which to attach the continuum geometric-decohesion model, the linearly elastic analytic solution for the stress and displacement distributions, of the boundary value problem pictured in (Fig. 4.1), provided by Benthem and Koiter [4.1] is

used. This solution provides that the stress distribution is

$$T_{11}^{\text{le}} = \text{Re } \Phi' - y \text{ Im } \Phi'' \tag{4.1}$$

$$T_{12}^{\text{le}} = -y \text{ Re } \Phi'' \tag{4.2}$$

$$T_{22}^{\text{le}} = \sigma + \text{Re } \Phi' + y \text{ Im } \Phi'' \tag{4.3}$$

and the expressions for the displacement distribution are

$$u_1^{\text{le}} = \sigma \frac{\kappa - 3}{8\mu} x + \frac{\kappa - 1}{4\mu} \text{ Re } \Phi + \frac{y}{2\mu} \text{ Im } \Phi' \tag{4.4}$$

$$u_2^{\text{le}} = \sigma \frac{\kappa + 1}{8\mu} y + \frac{\kappa + 1}{4\mu} \text{ Im } \Phi - \frac{y}{2\mu} \text{ Re } \Phi' \tag{4.5}$$

where

$$\Phi = \sigma \left(\sqrt{z^2 - a^2} - z \right) \tag{4.6}$$

$$\Phi' = \sigma \left(\frac{z}{\sqrt{z^2 - a^2}} - 1 \right) \tag{4.7}$$

$$\Phi'' = \sigma \left(\frac{1}{\sqrt{z^2 - a^2}} - \frac{z^2}{(z^2 - a^2)^{3/2}} \right) \tag{4.8}$$

for z in the first quadrant of the complex plane.

The normal stress along the x-axis is then

$$T_{22}^{\text{le}}\big|_{y \to 0} = \sigma \frac{|x|}{\sqrt{x^2 - a^2}} \qquad\qquad \forall \, |x| > a \tag{4.9}$$

which is unbounded at the crack tips $(x = \pm a)$, as expected.

4.2 Applying the Continuum Geometric-Decohesion Model

Turning to the continuum geometric-decohesion model to augment the linearly elastic so-
lution, in the present symmetric two dimensional case of the traction distribution applied

across the crack surface (3.12) is governed by

$$\frac{\partial^2 p}{\partial x^2} = \alpha^2 p. \tag{4.10}$$

The general solution is

$$p = A \sinh(\alpha x) + B \cosh(\alpha x) \tag{4.11}$$

Then, noting the symmetry of the problem across the y-axis, it is apparent that the traction distribution must be of the form

$$p = B \cosh(\alpha x) \tag{4.12}$$

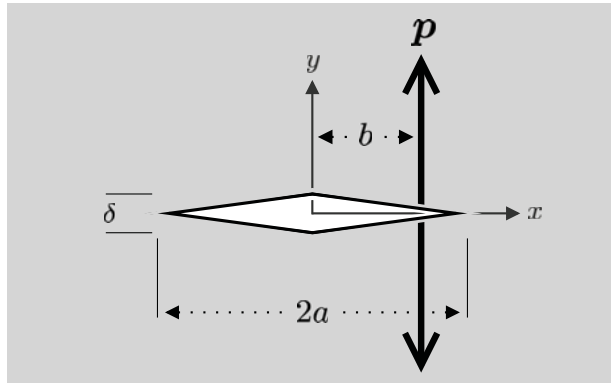where the scaling factor B will later be determined by the crack-front kinematic condition (3.13).

Fig. 4.2: Opposing point loads applied to the surface of the crack at the center of the infinite two dimensional plane.

Next, for the purpose of generating the stress and displacement field solutions from the functional form of the crack-face traction distribution, a kernel function is needed. To take advantage of the symmetry of the problem, the chosen kernel solution consists of equal and opposite point loads (of magnitude p) placed symmetrically across the x-axis on the crack

surface at a distance b in the positive direction from the y-axis (Fig. 4.2). The analytic, linear-elastic solution provided by Chang and Ma [4.2] is used to provide the stress field

$$T_{11}^{\mathrm{k}} = \mathrm{Re}\ F' - y\ \mathrm{Im}\ F'' \tag{4.13}$$

$$T_{12}^{\mathrm{k}} = -y\ \mathrm{Re}\ F'' \tag{4.14}$$

$$T_{22}^{\mathrm{k}} = \mathrm{Re}\ F' + y\ \mathrm{Im}\ F'' \tag{4.15}$$

and the displacement field

$$u_1^{\mathrm{k}} = \frac{\kappa - 1}{4\mu}\ \mathrm{Re}\ F + \frac{y}{2\mu}\ \mathrm{Im}\ F' \tag{4.16}$$

$$u_2^{\mathrm{k}} = \frac{\kappa + 1}{4\mu}\ \mathrm{Im}\ F - \frac{y}{2\mu}\ \mathrm{Re}\ F' \tag{4.17}$$

where

$$F = -p\frac{i}{\pi}\log\left(\frac{2\sqrt{z^2 - a^2}}{z - b} - i\frac{2[a^2 - zb]}{[z - b]\sqrt{a^2 - b^2}}\right) \tag{4.18}$$

$$F' = p\frac{1}{\pi}\frac{\sqrt{a^2 - b^2}}{[z - b]\sqrt{z^2 - a^2}} \tag{4.19}$$

$$F'' = -p\frac{1}{\pi}\sqrt{a^2 - b^2}\left[\frac{z}{[z - b][z^2 - a^2]^{3/2}}\right.$$

$$\left. +\frac{1}{[z - b]^2\sqrt{z^2 - a^2}}\right] \tag{4.20}$$

for z in the first quadrant of the complex plane.

Taking the symmetry of the problem into further consideration (to include the symmetry across the y-axis), a complementary point load is introduced at a distance b on the opposite

side of the y-axis. Then (4.18)-(4.20) can be rewritten as

$$F = p\frac{i}{\pi}\log\left(\frac{1 - i\frac{\sqrt{z^2 - a^2}}{\sqrt{a^2 - b^2}}}{1 + i\frac{\sqrt{z^2 - a^2}}{\sqrt{a^2 - b^2}}}\right) \tag{4.21}$$

$$F' = p\frac{2}{\pi}\frac{z\sqrt{a^2 - b^2}}{[b^2 - z^2]\sqrt{z^2 - a^2}} \tag{4.22}$$

$$F'' = -p\frac{2}{\pi}\frac{[a^2[b^2 + z^2] - 2z^4]\sqrt{a^2 - b^2}}{[b^2 - z^2]^2[z^2 - a^2]^{3/2}} \tag{4.23}$$

Now, the stress field for the full traction distribution utilized by the continuum geometric-decohesion model is produced by

$$T_{ij}^{\text{cgd}} = \int_0^a T_{ij}^{\text{k}}db \tag{4.24}$$

when using the fully symmetric solutions (4.21)-(4.23). The displacement field is similarly produced by

$$u_i^{\text{cgd}} = \int_0^a u_i^{\text{k}}db \tag{4.25}$$

Next, the far-field loading solution of Section 4.1 is combined with the solution of this section, and the crack-front condition (3.13) is applied at the crack tips ($x = \pm a$ and $y = 0$):

$$\left[\frac{\partial u_2^{\text{le}}}{\partial x} + \frac{\partial u_2^{\text{cgd}}}{\partial x}\right]_{\substack{x\to\pm a \\ y\to 0}} \to 0 \tag{4.26}$$

Or, more explicitly,

$$\left[[\kappa + 1]\,\text{Im}\,\Phi' - 2y\,\text{Re}\,\Phi'' + \right.$$
$$\left.\int_0^a [[\kappa + 1]\,\text{Im}\,F' - 2y\,\text{Re}\,F'']\,db\right]_{\substack{x\to\pm a \\ y\to 0}} \to 0 \tag{4.27}$$

This equation allows for the scaling factor of the traction distribution (B) to be calculated for

any given experimental parameter (α) and crack length ($2a$). Thus, with (4.12) and (4.27) the closing traction is fully defined by the continuum problem (independent of rupture criterion).

4.3   Linear-Elastic Field Solutions of a Center-Cracked Infinite 2D Plane

For purposes of later comparisons, all values are provided in unitless representations. Accordingly, distances are normalized by half the crack length as

$$x \rightarrow xa \tag{4.28}$$

$$y \rightarrow ya \tag{4.29}$$

$$b \rightarrow ba \tag{4.30}$$

stresses are normalized by the applied far-field traction as

$$T_{ij} \rightarrow T_{ij}\sigma \tag{4.31}$$

and displacements are normalized as

$$u_i \rightarrow u_i \frac{\sigma}{\mu} a \tag{4.32}$$

Finally, the length-scale parameter is normalized as

$$\alpha \rightarrow \frac{\alpha}{a} \tag{4.33}$$

Next, it is noted that the kernel functions are not unmanageable they are not analytically integrable. So, Gauss-Kronrod numerical integration [4.3, 4.4] is used in order to calculate the integrals required to attain the complete solution for the stress and displacement fields.

The integrals (4.24), (4.25), and (4.27) are weakly singular, and as such care must be taken when applying numerical quadrature to segregate the portion of the integration region where the integrand is strongly divergent.

αa	0	1	2	3	4	5
B	-1.000	-0.7898	-0.4387	-0.2049	-0.08848	-0.03671

Table 4.1: The resultant values of the traction distribution scaling factor B for differing values of the length-scale parameter α. The variable product αa is used instead of α alone for the purpose of providing unitless solutions. 1,000,000 101-point Gauss-Kronrod elements were employed in the process of numerical integration. All values of the traction distribution scaling factor B are exact to the precision given.

Before field values can be calculated, the scaling factor (B) for a range of calibration variable (α) values must be computed (Table 4.1).
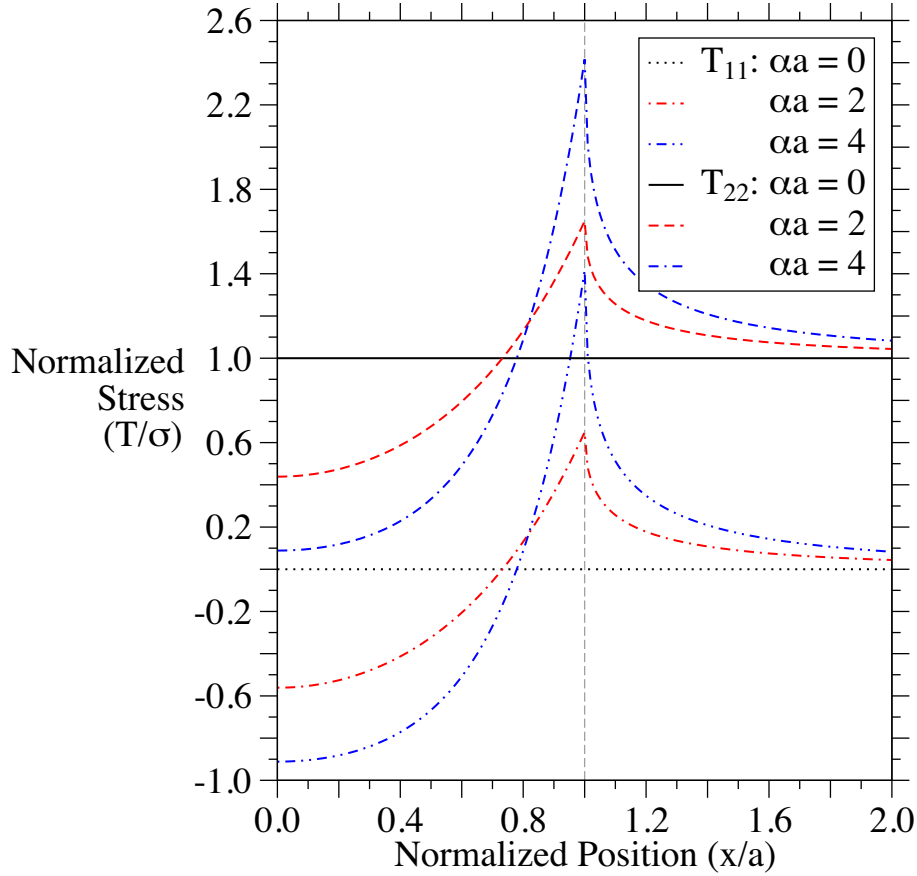
Fig. 4.3: Two components of the normalized stress field along the crack surface for a center-cracked infinite 2D plate comprised of a linearly elastic material. The coordinate origin is placed at the center of the crack. For the purposes of taking $y \to 0$ the evaluation is taken at $y = a/1,000,000$. All values are symmetric across the x-axis and y-axis. 1,000,000 101-point Gauss-Kronrod elements were employed in the process of numerical integration. The error is within the size of the symbols for all values plotted.

The stress field results along the x-axis (Fig. 4.3) are both continuous and bounded while crossing the crack front, as expected. Further, the limiting case of $\alpha \to 0$, which means the continuum geometric-decohesion model closing traction is constant along the entire crack surface, produces the intuitively correct result of $T_{11} \to 0$ and $T_{22} \to \sigma$. And, for non-zero α the results are physically reasonable; the minimum stress value occurs at the center of the crack, the peak stress value occurs at the crack tip, and the stress field approaches $T_{11} \to 0$ and $T_{22} \to \sigma$ as $x \to \infty$. Notably, while the first derivative of the stress field remains finite,

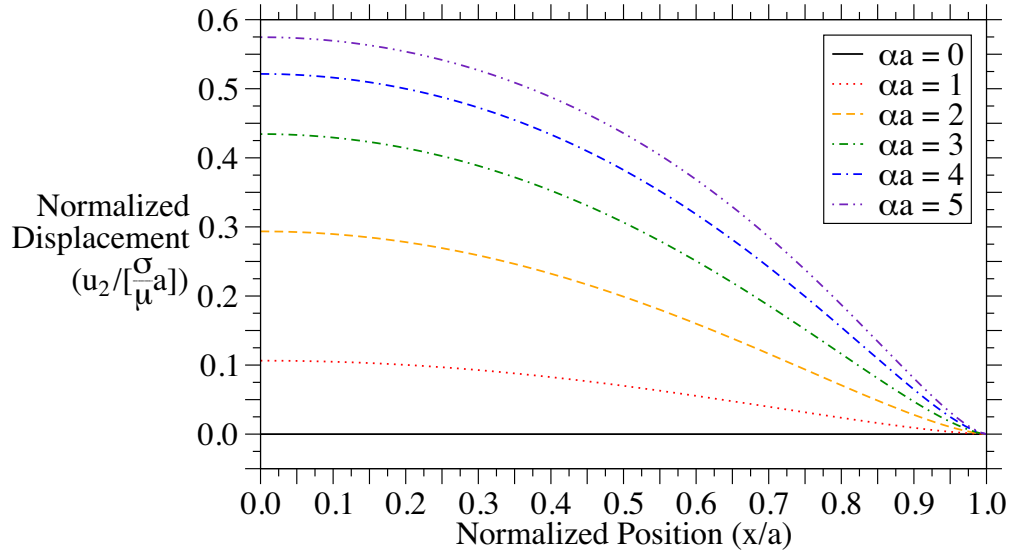it is discontinuous across the crack front.

Fig. 4.4: The normalized displacement field along the crack surface for a center-cracked infinite 2D plate comprised of a linearly elastic material. The coordinate origin is placed at the center of the crack. For the purposes of taking $y \to 0$ the evaluation is taken at $y = a/1,000,000$. To determine the displacement response, Poisson's ratio is given by $\nu = 1/3$. All values are antisymmetric across the x-axis and symmetric across the y-axis. 1,000,000 101-point Gauss-Kronrod elements were employed in the process of numerical integration. The error is within the size of the symbols for all values given.

The displacement field results along the x-axis (Fig. 4.4) correctly mirror those of the stress field. As required by symmetry across the x-axis and the crack-front condition (3.13), the displacement and its first derivative go to zero at the crack tips. Further, as expected from symmetry across the y-axis, the peak displacement values occur in the middle of the crack surface. Finally, in the $\alpha \to 0$ limit, signaling a constant closing traction p across the crack surface for arbitrary crack length a, u_2 is found to be 0, corresponding to a uniform traction condition that simulates the absence of a crack.

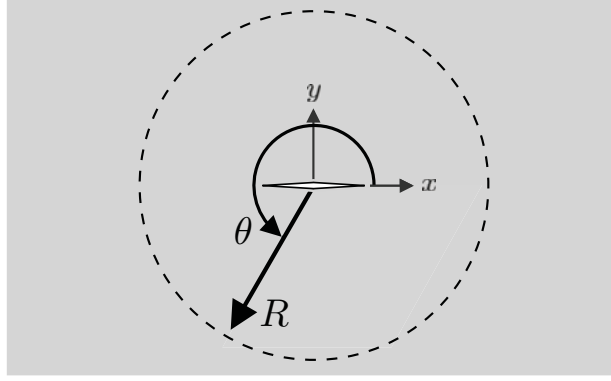## 4.4 Linear-Elastic Strain Energy Release Rate for a Center-Cracked Infinite 2D Plane

Fig. 4.5: The circular integration contour used to calculate the strain energy release rate for quasi-static crack growth.

In addition to the stress and displacement distributions, it is worthwhile to compute the strain energy release rate. In order to calculate the strain energy release rate, the work done along a circular contour (Fig. 4.5) is examined through a loading, crack extension, and unloading process. The contour is centered at the middle of the crack and has a radius R. Since the material is treated as linearly elastic, any dissipation of energy evinced in this closed process must be due to the topology change. This allows consideration of only the selected disc (containing the crack) when calculating the strain energy release rate, instead of the entire body.

Turning first to the loading process, where the applied load is brought from zero to the loading value necessary for crack extension $\sigma_{\rm c}$, the work done on the contour is

$$W^1 = \frac{1}{2} \int_0^{2\pi} \left[\boldsymbol{t}(a, \theta) \cdot \boldsymbol{u}(a, \theta) \right] R \, d\theta \tag{4.34}$$

where $\boldsymbol{t}(l, \theta)$ and $\boldsymbol{u}(l, \theta)$ are the traction and displacement vectors on the contour when the crack has length $2l$, at the point given by the polar coordinates R and θ.

Now, during crack growth the change in $\boldsymbol{t}$ and $\boldsymbol{u}$ will not necessarily be linear, but by enforcing the increment of crack extension to be an infinitesimal $2da$ the work done can be well approximated by

$$W^2 = \frac{1}{2} \int_0^{2\pi} [\boldsymbol{t}(a + da, \theta) + \boldsymbol{t}(a, \theta)] \cdot [\boldsymbol{u}(a + da, \theta) - \boldsymbol{u}(a, \theta)] \, R \, d\theta$$

Finally, similar to the loading process, the work done for the unloading process is

$$W^3 = -\frac{1}{2} \int_0^{2\pi} [\boldsymbol{t}(a + da, \theta) \cdot \boldsymbol{u}(a + da, \theta)] \, R \, d\theta \tag{4.35}$$

So, the amount of work dissipated by the crack extension process is

$$W = \sum_i W^i \tag{4.36}$$

$$= \frac{1}{2} \int_0^{2\pi} [\boldsymbol{t}(a, \theta) \cdot \boldsymbol{u}(a + da, \theta)$$

$$-\boldsymbol{t}(a + da, \theta) \cdot \boldsymbol{u}(a, \theta)] \, R \, d\theta \tag{4.37}$$

and the strain energy release rate is therefore

$$G = \left. \frac{W}{2da} \right|_{da \to 0} \tag{4.38}$$

$$= \frac{1}{2} \int_0^{2\pi} \left[\boldsymbol{t}(a, \theta) \cdot \frac{d\boldsymbol{u}}{da}(a, \theta) - \frac{d\boldsymbol{t}}{da}(a, \theta) \cdot \boldsymbol{u}(a, \theta) \right] R \, d\theta$$

which can then be rewritten, by making use of the problem symmetry, as

$$G = 2 \int_0^{\pi/2} \left[\boldsymbol{t}(a, \theta) \cdot \frac{d\boldsymbol{u}}{da}(a, \theta) \right.$$

$$\left. -\frac{d\boldsymbol{t}}{da}(a, \theta) \cdot \boldsymbol{u}(a, \theta) \right] R \, d\theta \tag{4.39}$$

Next, the far-field loading stress field derivates

$$\frac{dT_{11}^{\text{le}}}{da} = \text{Re } \frac{d\Phi'}{da} - y \text{ Im } \frac{d\Phi''}{da} \tag{4.40}$$

$$\frac{dT_{12}^{\text{le}}}{da} = -y \text{ Re } \frac{d\Phi''}{da} \tag{4.41}$$

$$\frac{dT_{22}^{\text{le}}}{da} = \text{Re } \frac{d\Phi'}{da} + y \text{ Im } \frac{d\Phi''}{da} \tag{4.42}$$

and displacement field derivatives

$$\frac{du_1^{\text{le}}}{da} = \frac{\kappa - 1}{4\mu} \text{ Re } \frac{d\Phi}{da} + \frac{y}{2\mu} \text{ Im } \frac{d\Phi'}{da} \tag{4.43}$$

$$\frac{du_1^{\text{le}}}{da} = \frac{\kappa + 1}{4\mu} \text{ Im } \frac{d\Phi}{da} - \frac{y}{2\mu} \text{ Re } \frac{d\Phi'}{da} \tag{4.44}$$

can be calculated by using

$$\frac{d\Phi}{da} = -\sigma \frac{a}{\sqrt{z^2 - a^2}} + \frac{d\sigma}{da} \frac{\Phi}{\sigma} \tag{4.45}$$

$$\frac{d\Phi'}{da} = \sigma \frac{az}{(z^2 - a^2)^{3/2}} + \frac{d\sigma}{da} \frac{\Phi'}{\sigma} \tag{4.46}$$

$$\frac{d\Phi''}{da} = -\sigma \frac{a(a^2 + 2z^2)}{(z^2 - a^2)^{5/2}} + \frac{d\sigma}{da} \frac{\Phi''}{\sigma} \tag{4.47}$$

where σ is the far-field applied traction that results in continuous satisfaction of the rupture criterion, and is a function of a.

Further, using the Leibniz integral rule [4.5] the continuum geometric-decohesion stress field derivatives are

$$\frac{dT_{ij}^{\text{cgd}}}{da} = \int_0^a \frac{dT_{ij}^{\text{k}}}{da} db \tag{4.48}$$

and the displacement field derivatives are

$$\frac{du_1^{\text{cgd}}}{da} = \int_0^a \frac{du_1^{\text{k}}}{da} db + \frac{\kappa - 1}{4\mu} \cosh(\alpha a) \tag{4.49}$$

$$\frac{du_2^{\text{cgd}}}{da} = \int_0^a \frac{du_2^{\text{k}}}{da} db \tag{4.50}$$

where the derivatives of the kernel functions for the stress field are

$$\frac{dT_{11}^{\text{k}}}{da} = \text{Re} \frac{dF'}{da} - y \, \text{Im} \frac{dF''}{da} \tag{4.51}$$

$$\frac{dT_{12}^{\text{k}}}{da} = -y \, \text{Re} \frac{dF''}{da} \tag{4.52}$$

$$\frac{dT_{22}^{\text{k}}}{da} = \text{Re} \frac{dF'}{da} + y \, \text{Im} \frac{dF''}{da} \tag{4.53}$$

and the derivatives of the kernel functions for the displacement field are

$$\frac{du_1^{\text{k}}}{da} = \frac{\kappa - 1}{4\mu} \, \text{Re} \frac{dF}{da} + \frac{y}{2\mu} \, \text{Im} \frac{dF'}{da} \tag{4.54}$$

$$\frac{du_1^{\text{k}}}{da} = \frac{\kappa + 1}{4\mu} \, \text{Im} \frac{dF}{da} - \frac{y}{2\mu} \, \text{Re} \, . \frac{dF'}{da} \tag{4.55}$$

These can be calculated using

$$\frac{dF}{da} = -p\frac{2}{\pi} \frac{a}{\sqrt{z^2 - a^2}\sqrt{a^2 - b^2}} + \frac{dp}{da} \frac{F}{p} \tag{4.56}$$

$$\frac{dF'}{da} = p\frac{2}{\pi} \frac{az}{(z^2 - a^2)^{3/2}\sqrt{a^2 - b^2}} + \frac{dp}{da} \frac{F'}{p} \tag{4.57}$$

$$\frac{dF''}{da} = -p\frac{2}{\pi} \frac{a^3 + 2az^2}{(z^2 - a^2)^{5/2}\sqrt{a^2 - b^2}} + \frac{dp}{da} \frac{F''}{p} \tag{4.58}$$

For the strain energy release rate to be calculated, the functional form of the rupture variable (Θ) must be defined, so that the the necessary applied load σ_{c} for crack extension

can be determined. To this end, a simple rupture variable is chosen as

$$\Theta = \boldsymbol{m} \cdot \boldsymbol{Tm} \tag{4.59}$$

and by examining the stress fields in this problem, the rupture variable reduces to simply

$$\Theta = T_{22}\big|_{\substack{x \to \pm a \\ y \to 0}} \tag{4.60}$$

since the stress peaks most strongly at $\boldsymbol{x} \to (0, \pm a)$ and $\boldsymbol{m} \to \hat{y}$. So, the necessary applied load can be written as

$$\sigma_{\mathrm{c}} = \left[T_{22}^{\mathrm{cgd}} + T_{22}^{\mathrm{le}} \right]_{\substack{x \to \pm a \\ y \to 0}} \tag{4.61}$$

and the necessary condition for crack extension is

$$\left[T_{22}^{\mathrm{le}} + T_{22}^{\mathrm{cgd}} \right]_{\substack{x \to \pm a \\ y \to 0}} \geq 1 \tag{4.62}$$

Non-dimensional representations are kept here, but for the purpose of calculating the strain energy release rate the transformation $z \to za$ must be performed before the derivative of σ_{c} is taken. This ensures the derivative is still evaluated at the crack tip after extension.
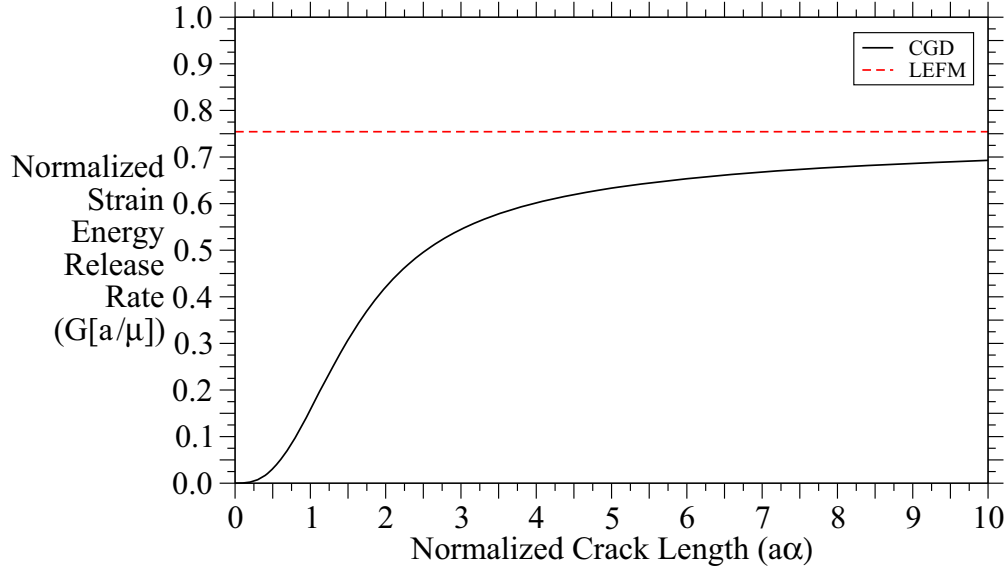
Fig. 4.6: The strain energy release rate for a center-cracked infinite 2D plate comprised of a linearly
elastic material. All values are calculated with the length-scale parameter $\alpha = 1$. Poisson's
ratio is given by $\nu = 1/3$. 1,000 101-point Gauss-Kronrod elements were employed in each
process of numerical integration.

Based on the foregoing, the strain energy release rate can be computed (Fig. 4.6). As
expected, the strain energy release rate and its first derivative are 0 when no crack is present
in the material. As the crack extends and its length (a) tends towards infinity, the strain
energy release rate asymptotically approaches the constant, linear-elastic fracture mechanics
solution.

The linear-elastic fracture mechanics solution is found by using the applied load σ deter-
mined by the continuum geometric-decohesion solution at $a \to \infty$, where both solutions will
match, and Young's modulus (E). These values are inserted into the rupture criterion

$$G_c = \frac{\sigma^2}{E} \pi a \qquad (4.63)$$

derived from (1.14) in order to produce the value for comparison.

The effect of the length-scale parameter (α) in this problem is restricted to linearly scaling the normalized crack length axis of the plot, and produces no other changes in the strain energy release rate. This is in agreement with its effect on the stress and displacement fields.

Thus, for the chosen example problem the continuum geometric-decohesion model is able to reproduce the familiar linear-elastic fracture mechanics results. Unfortunately, producing an analytic solution becomes too difficult for J2 elastic-plastic materials. So, the demonstration now turns to computational results produced using the Finite Element Method method (discussed in Chapter 5).

4.5 J2 Elastic-Plastic Field Solutions of a Center-Cracked Finite 2D Plane

Here the features of the continuum geometric-decohesion model solution using a J2 elastic-plastic constitutive model with isotropic, power-law hardening will be examined by utilizing the Finite Element Method. For consistency, it will first be shown that the Finite Element Method employed and analytic solution produce consistently comparable results. Fortunately, the modularity of the Continuum Geometric-Decohesion Model makes changing the constitutive model simple, even if the results are complex.
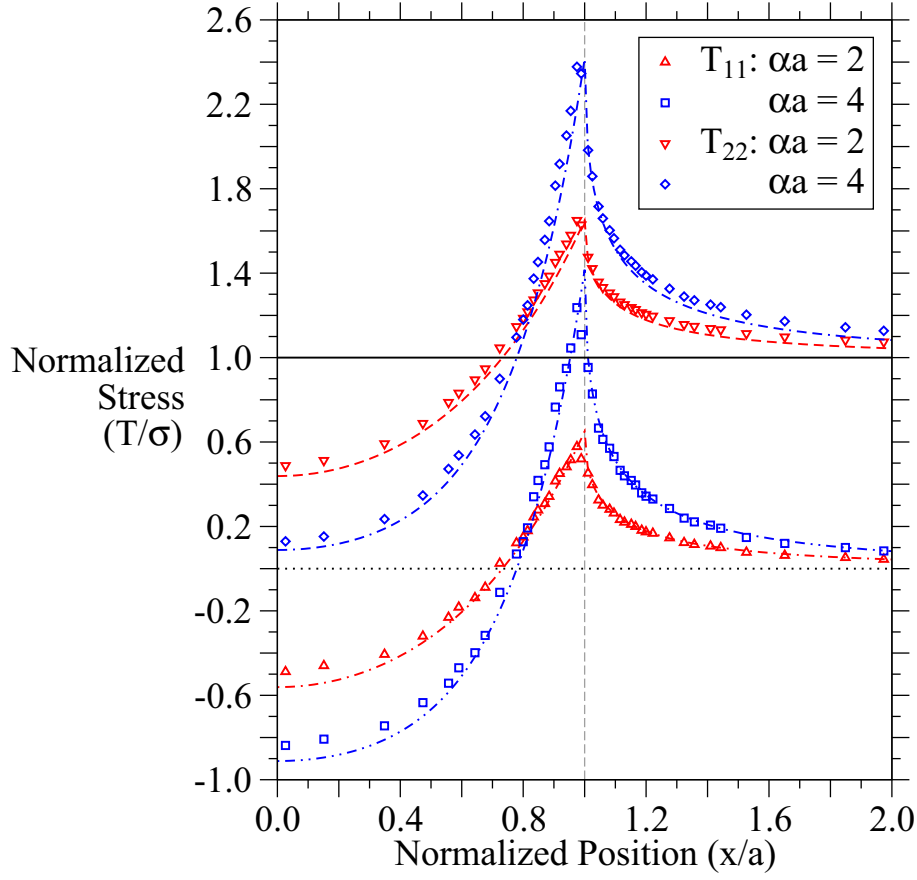
Fig. 4.7: Two components of the normalized stress field along the crack surface for a center-cracked finite 2D plate comprised of a linearly-elastic material. Analytic results 4.3 has been reproduced as lines, while the symbols depict data points from the Finite Element Method results. The lines represent the analytic linear-elastic results. For the purposes of taking $y \to 0$, the restriction $0 < y < 3a/100$ is enforced, with the exact location varying dependent on the mesh. All values are symmetric across the x-axis and y-axis. The error for all points lies within the size of the symbol.

To that end, the field solutions using linear-elastic constitutive equations have been reproduced (Figs. 4.7 and 4.8). While the results are generally quite similar between the two methods, the Finite Element Method results stray from the analytic results for a couple reasons. First, the analytic solution assumes a truly infinite two dimensional plate, which must be approximated in the Finite Element Method solution by a plate that is much larger than the crack that lies within it ($10a$ by $10a$). Second, the y location of the evaluation

point depends on the mesh construction, and it accordingly varies in exact location as well as strays further from the x-axis in general.
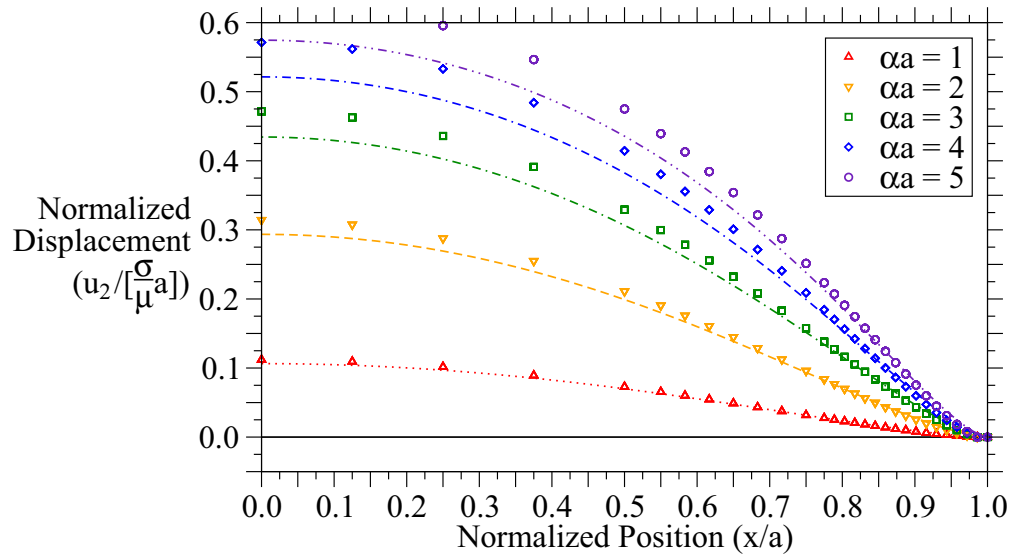

Fig. 4.8: The normalized displacement field along the crack surface for a center-cracked finite 2D plate comprised of a linearly-elastic material. Analytic results 4.4 has been reproduced as lines, while the symbols depict data points from the Finite Element Method results. The lines represent the analytic linear-elastic results. For the purposes of taking $y \to 0$, the restriction $0 < y < 3a/100$ is enforced, with the exact location varying dependent on the mesh. All values are antisymmetric across the x-axis and symmetric across the y-axis. The error for all points lies within the size of the symbol.

In addition to reproducing the analytic plots, the Finite Element Method solution can produce results that are not easily generated through analytic means. A burden of the Finite Element Method is that it requires the calculation of field values for a vast number of points in the body. But this wealth of data points is a boon for data visualization, and accordingly fringe plots for the stress and displacement fields have been produced (Figs. 4.9 and 4.10).
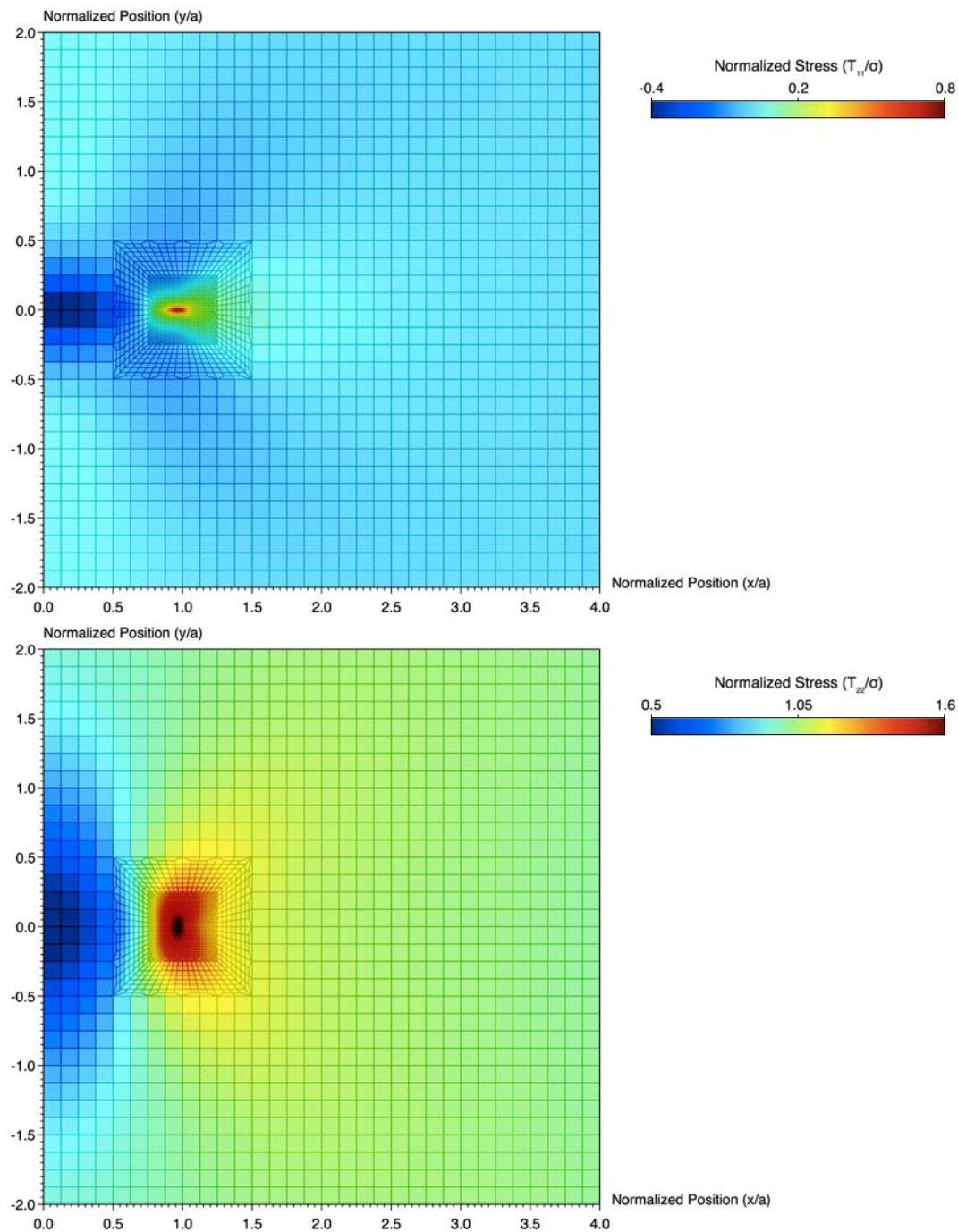
Fig. 4.9: Two components of the normalized stress field on a section of the linear-elastic finite 2D plate modeled containing half of the crack, with the computational mesh represented by dark lines. The length-scale parameter α has been set at 2. All values are symmetric across the y-axis. The values shown throughout the computational mesh are linear interpolations of the discrete data points available.
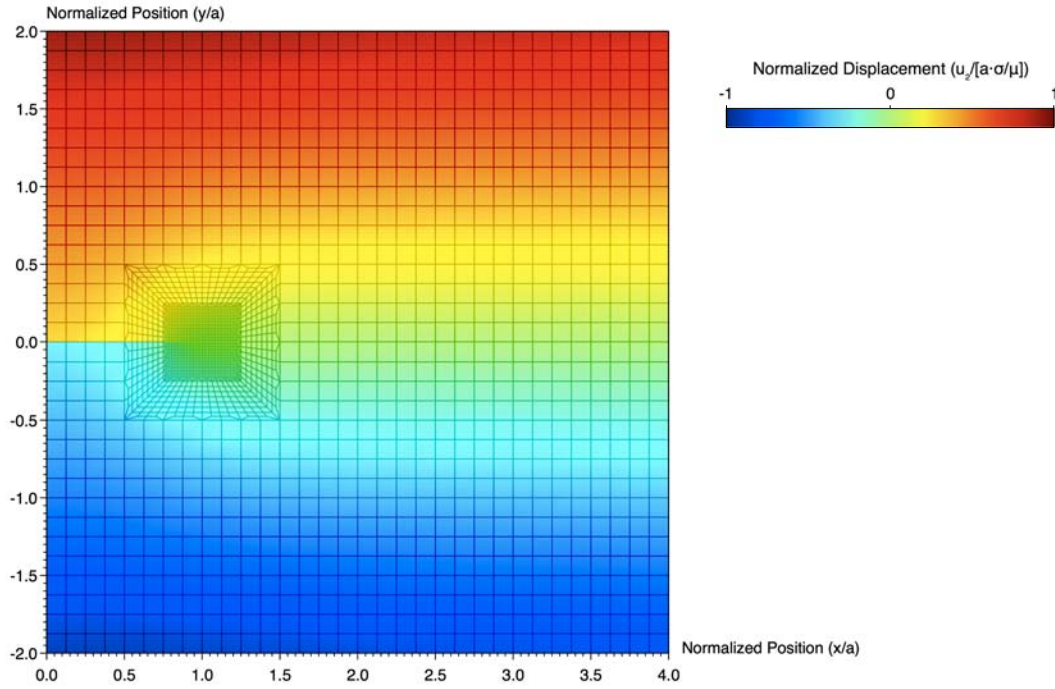
Fig. 4.10: The normalized displacement field on a section of the linear-elastic finite 2D plate modeled containing half of the crack, with the computational mesh represented by dark lines. The length-scale parameter α has been set at 2. All values are symmetric across the y-axis. The values shown throughout the computational mesh are linear interpolations of the discrete data points available.

A J2 elastic-plastic constitutive model with isotropic, power-law hardening has also been used in Finite Element analyses of the normal-opening crack problem. The yield stress σ_y in this model is

$$\sigma_y = \sigma_0 \left(1 + \frac{\epsilon}{\epsilon_0} \right)^{\chi} \tag{4.64}$$

where σ_0 is the initial yield stress, ϵ_0 is a reference strain, ϵ is the equivalent plastic strain, and χ is the power law hardening exponent.

For comparison purposes the stress, displacement, and equivalent plastic strain fields along the crack surface have been using the J2 elastic-plastic model (Figs. 4.11-4.13). As expected, the resulting stress values have decreased and the strain values have increased

when compared with the linear-elastic results. Also as expected, the effective plastic strain peaks at the same location that the stress is greatest. These results are reflected in the fringe plots generated by the Finite Element analyses for the J2 elastic-plastic simulations (Figs. 4.14-4.16).
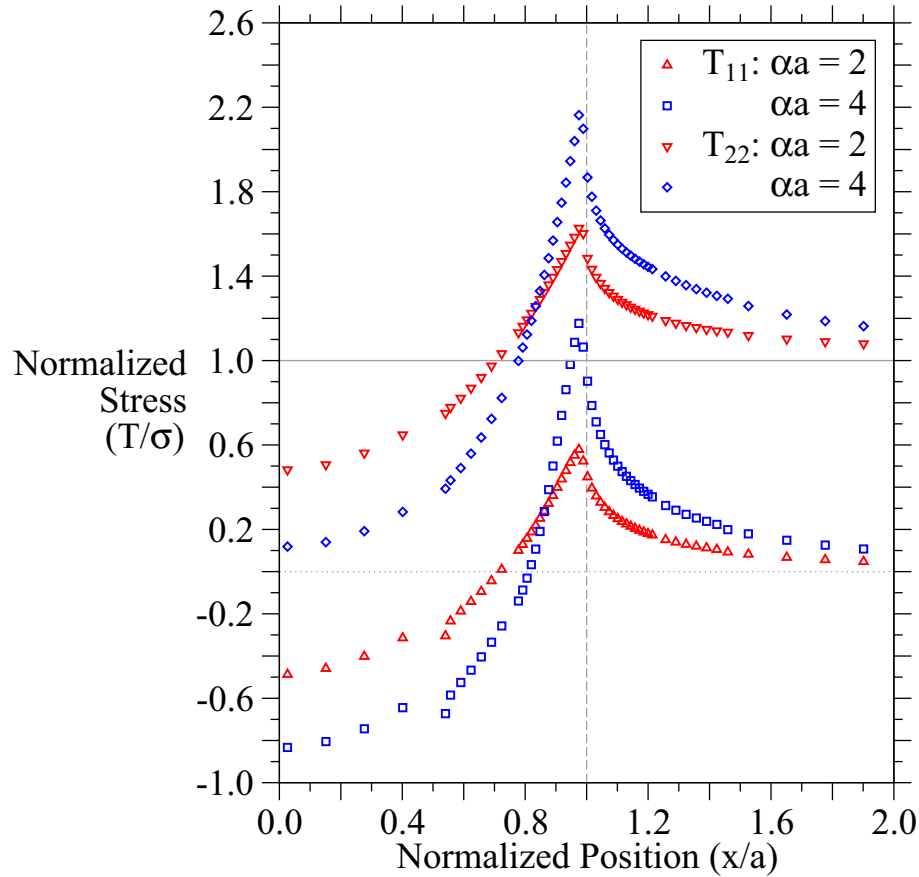

Fig. 4.11: Two components of the normalized stress field along the crack surface for a center-cracked finite 2D plate comprised of a J2 elastic-plastic material. Linearly elastic results 4.3 has been reproduced as lines, while the symbols depict data points from the Finite Element Method J2 elastic-plastic results with $\sigma_0 = 6\sigma/5$, $\epsilon_0 = 1/10$, and $\chi = 1/5$. The lines represent the analytic linear-elastic results. For the purposes of taking $y \to 0$, the restriction $0 < y < 3a/100$ is enforced, with the exact location varying dependent on the discretization mesh implemented. All values are symmetric across the x-axis and y-axis. The error for all points lies within the size of the symbol.
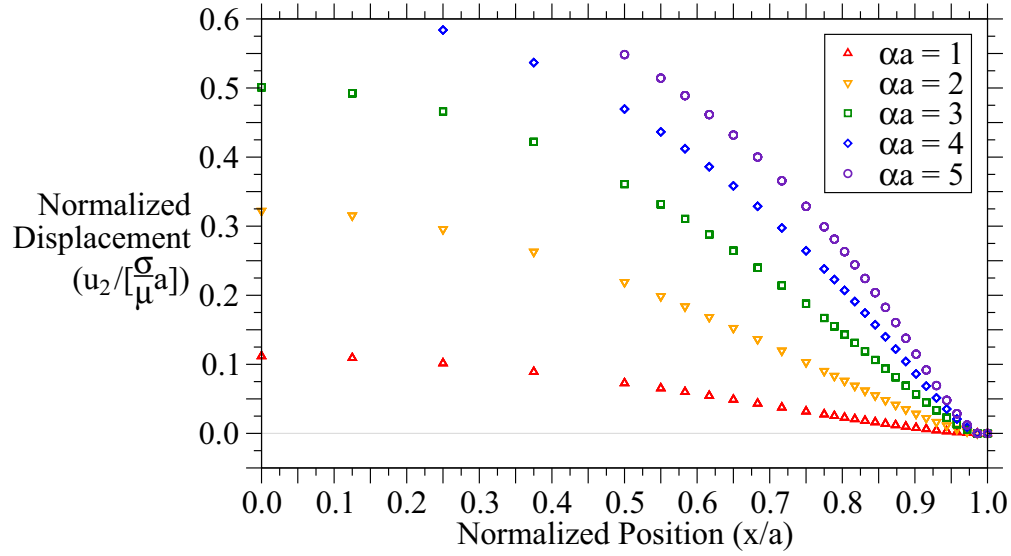
Fig. 4.12: The normalized displacement field along the crack surface for a center-cracked finite 2D plate comprised of a J2 elastic-plastic material. Linearly elastic results 4.4 has been reproduced as lines, while the symbols depict data points from the Finite Element Method J2 elastic-plastic results with $\sigma_0 = \sigma$, $\epsilon_0 = 1/10$, and $\chi = 1/5$. The lines represent the analytic linear-elastic results. For the purposes of taking $y \to 0$, the restriction $0 < y < 3a/100$ is enforced, with the exact location varying dependent on the discretization mesh implemented. All values are antisymmetric across the x-axis and symmetric across the y-axis. The error for all points lies within the size of the symbol.
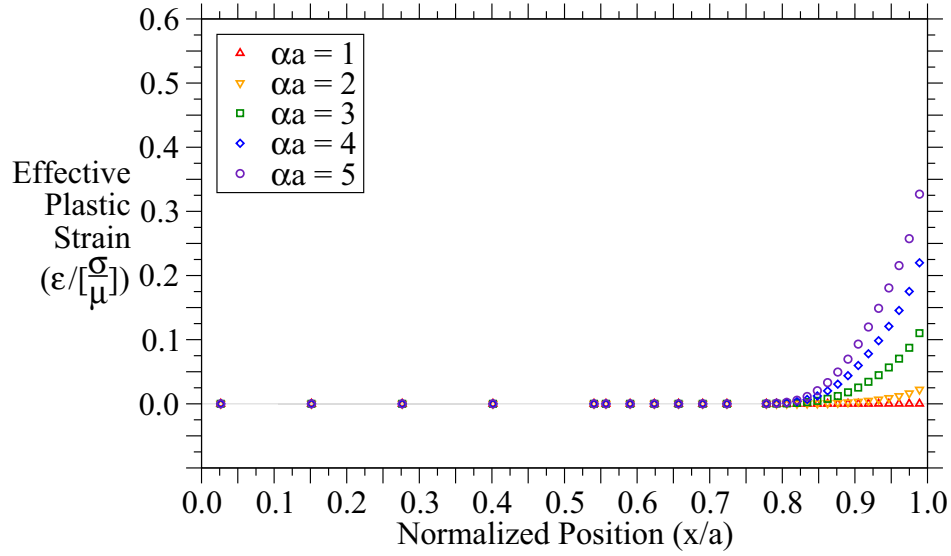
Fig. 4.13: The normalized effective plastic strain along the crack surface for the J2 elastic-plastic results with $\sigma_0 = \sigma$, $\epsilon_0 = 1/10$, and $\chi = 1/5$. For the purposes of taking $y \to 0$, the restriction $0 < y < 3a/100$ is enforced, with the exact location varying dependent on the discretization mesh implemented. All values are antisymmetric across the x-axis and symmetric across the y-axis. The error for all points lies within the size of the symbol.
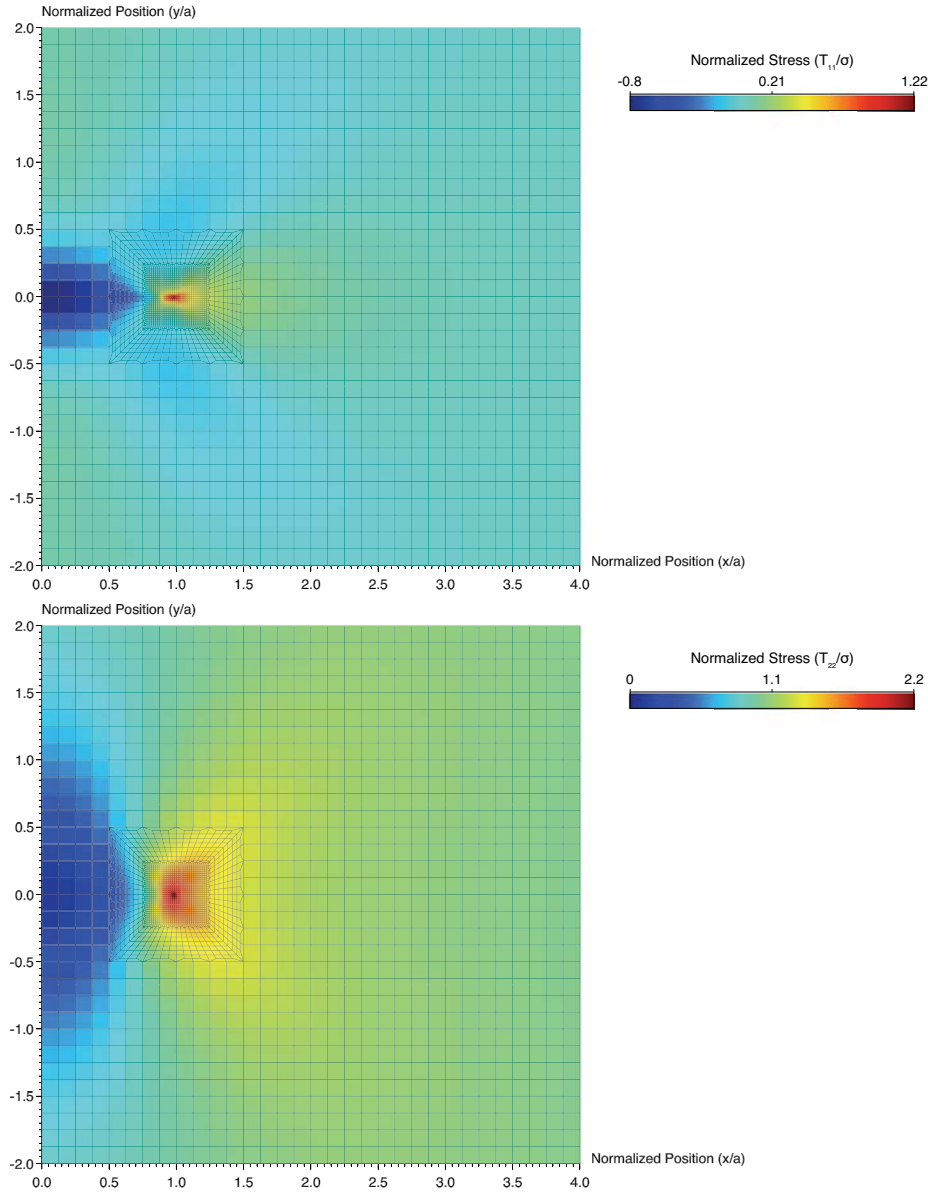
Fig. 4.14: Two components of the normalized stress field on a section of the J2 elastic-plastic finite 2D plate modeled containing half of the crack, with the computational mesh represented by dark lines. The length-scale parameter α has been set at 4, while the J2 plasticity parameters are set as $\sigma_0 = \sigma$, $\epsilon_0 = 1/10$, and $\chi = 1/5$. All values are symmetric across the y-axis. The values shown throughout the computational mesh are linear interpolations of the discrete data points available.
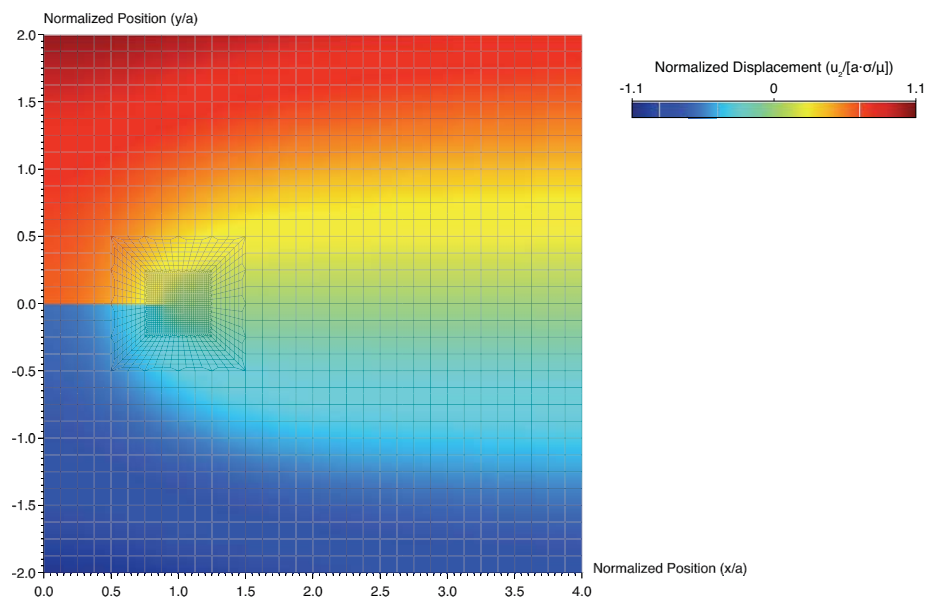
Fig. 4.15: The normalized strain field on a section of the J2 elastic-plastic finite 2D plate modeled containing half of the crack, with the computational mesh represented by dark lines. The length-scale parameter α has been set at 4, while the J2 plasticity parameters are set as $\sigma_0 = \sigma$, $\epsilon_0 = 1/10$, and $\chi = 1/5$. All values are symmetric across the y-axis. The values shown throughout the computational mesh are linear interpolations of the discrete data points available.
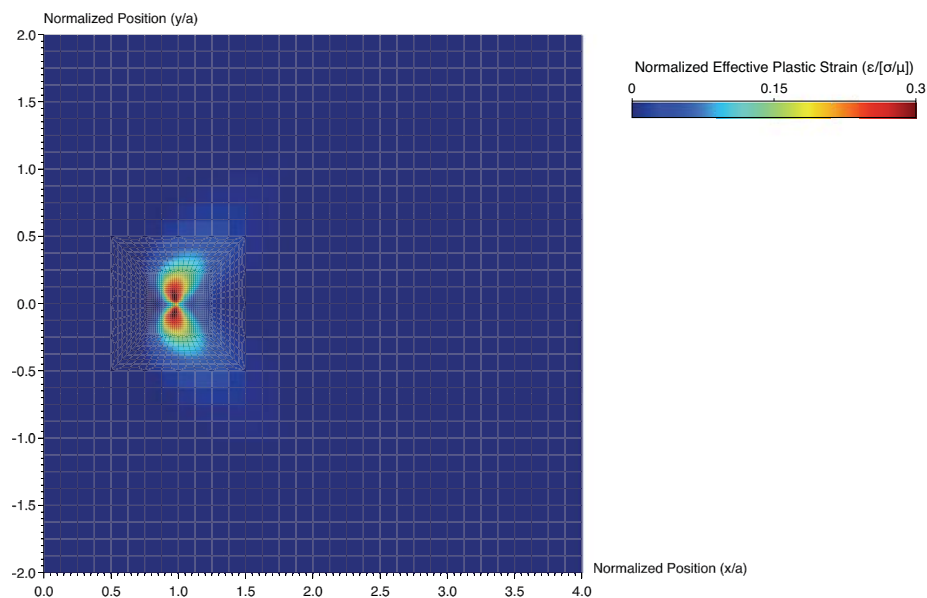
Fig. 4.16: The normalized effective plastic strain field on a section of the J2 elastic-plastic finite 2D plate modeled containing half of the crack, with the computational mesh represented by dark lines. The length-scale parameter α has been set at 4, while the J2 plasticity parameters are set as $\sigma_0 = \sigma$, $\epsilon_0 = 1/10$, and $\chi = 1/5$. All values are symmetric across the y-axis. The values shown throughout the computational mesh are linear interpolations of the discrete data points available.

Bibliography

[4.1] J. P. Benthem and W. T. Koiter. Asymptotic approximations to crack problem. *Mechanics of Fracture*, 1:131–178, 1973.

[4.2] C.-Y. Chang and C.-C. Ma. The mixed-mode fracture analysis of multiple embedded cracks in a semi-infinite plane by an analytical alternating method. *Journal of Pressure Vessel Technology*, 124:446–456, 2002.

[4.3] A. S. Kronrod. Integration with control of accuracy. *Doklady Akademii Nauk Soyuz Sovetskikh Sotsialisticheskikh Respublik (Presidium of the Russian Academy of Sciences)*, 154:283–286, 1964.

[4.4] A. S. Kronrod. *Nodes and Weights for Quadrature Formulae: Sixteen-Place Tables.* Consultants Bureau, 1965.

[4.5] F. S. Woods. *Advanced Calculus: A Course Arranged with Special Reference to the Needs of Students of Applied Mathematics*, pages 141–144. Ginn, 1962.

Chapter 5

Computational Methodology for Fracture Mechanics Applications

While analytical solutions for fracture mechanics problems can be desirable for the depth of information they provide, any but the simplest problems are too difficult to solve analytically. A large range of analytically unsolvable problems is not a feature of fracture mechanics specifically, but plagues standard continuum mechanics (and all boundary value) problems as well. Still, fracture mechanics has some special computational complications to deal with. For one, the fields being modeled have high curvature around crack fronts, requiring denser meshes than would be employed for standard continuum mechanics problems. Further, with many cohesive zone implementations, the boundary values due to closing tractions are not known explicitly beforehand, adding extra degrees of freedom to the problem. Finally, key to any fracture mechanics simulation is the changing topology of the problem domain.

Within the fracture mechanics field, there are a variety of numerical methods employed to solve complex problems. These include the Finite Element Method method [5.24, 5.14, 5.7, 5.21] and the boundary element method [5.28, 5.33, 5.12]. Mesh-free methods are a particularly active area of research [5.11, 5.26, 5.7], with prominent versions including the element-free Galerkin method [5.25, 5.10, 5.15, 5.16, 5.27, 5.32] and the natural element

method [5.38, 5.39, 5.19]. Bridging scale decompositions are also utilized in fracture mechanics, where the continuum mechanics simulation methods are paired with micromechanics simulations such as molecular dynamics [5.2, 5.3, 5.31, 5.31, 5.36]. However, in this dissertation it is the Finite Element Method method and some of its derivative forms (as used in sections 4.5) that will be discussed.

5.1 The Finite Element Method

The Finite Element Method has undergone decades of intense scrutiny and research, and is a widely used and highly popular numerical approximation method in continuum mechanics. It is so well established that courses about the Finite Element Method are regularly available in continuum mechanics related graduate curricula. A brief overview of the Finite Element Method is provided here as a point of reference for the following sections.

The Finite Element Method method is a procedure for finding numerical approximations of solutions to partial differential equations, and is thus readily useable for the difficult boundary value problems present in continuum mechanics. In order to find approximate solutions to the displacement field in a body, the problem domain (typically the physical coordinate space that a considered body occupies) must be discretized (Fig. 5.1). The space discretization produced for a given problem is termed a mesh, and its properties affect the quality and capability of the numerical method for which it is being created. The mesh itself is often an approximation of the true body geometry, with the mesh deviating the most at finely detailed, curved, and sharply varied geometric features.
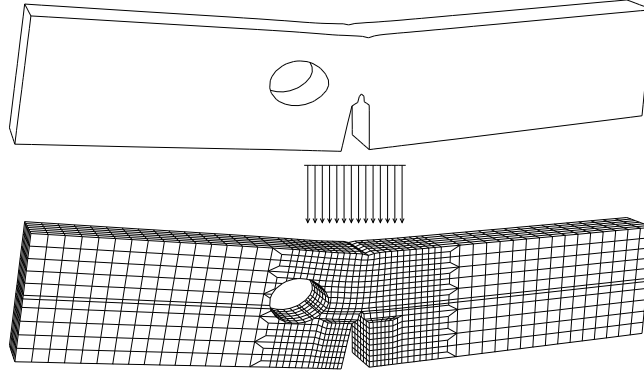
Fig. 5.1: An example body to be modeled for a three point bend analysis on top. At bottom, is the mesh discretization of the same body to be used for computation.

In three dimensions, a Finite Element mesh for a body $\mathcal{B}$ typically consists of tetrahedral or hexahedral elements $\mathcal{E}_i$ bounded by planar facets $\partial \mathcal{E}_{ij}$ that share a set of nodes. The term "element" is used to refer to the polyhedra that are used to discretize the domain. Let a Finite Element mesh be defined using the set of spatial locations $\mathbb{X}$, which define the positions of nodes. It is these nodes that comprise the vertices of polyhedra that discretize the body $\mathcal{B}$, and it is at their locations that some of the field values will be calculated. The approximate solution is to be constructed using a set of functions, called basis functions, whose structure is determined by the mesh. Together, these basis functions, along with the nodal data, create continuous functions that are the numerical field solutions across the entire body. There is one basis function for every node, and the ith basis function $\boldsymbol{N}_i(\boldsymbol{X})$ is associated with the ith node by the Kronecker delta property

$$\boldsymbol{N}_i(\boldsymbol{X}_j) = \delta_{ij} \tag{5.1}$$

where $\boldsymbol{X}_j$ is the reference position of the jth node. The basis function N_i is further required to obey

$$\boldsymbol{N}_i(\boldsymbol{X}) = 0 \qquad \qquad \boldsymbol{X} \in \{\mathcal{E} | \boldsymbol{X}_i \notin \mathcal{E}\} \tag{5.2}$$

and

$$\boldsymbol{N}_i(\boldsymbol{X}) = 0 \qquad\qquad \boldsymbol{X} \in \{\partial\mathcal{E}_{ij} | \boldsymbol{X}_i \notin \mathcal{E}_{ij}\} \qquad (5.3)$$

with the collection of basis functions and derivatives thus defined, the full approximate solution is then given as

$$\tilde{\boldsymbol{u}}(\boldsymbol{X}) = \tilde{\boldsymbol{u}}_i N_i(\boldsymbol{X}) \qquad (5.4)$$

where the index i indicates the node with associated basis function weights $\tilde{\boldsymbol{u}}_i$.

Now, the basis functions must collectively satisfy the requirement

$$\sum_i \boldsymbol{N}_i(\boldsymbol{X}) = \boldsymbol{1} \qquad\qquad \boldsymbol{X} \in \mathcal{B} \qquad (5.5)$$

termed the partition of unity property property.

A further condition on the Finite Element Method is that the basis functions have the approximability property. The approximability property can be loosely defined as requiring that the subspace of functions generate-able by a linear combination of the basis functions includes the exact solution as the size of the mesh elements goes to zero. It is possible to represent an arbitrary linear variation over each element, by setting the nodal values of the element consistent with the lienar function. The partition of unity and approximability properties are all that is required to assure that all solutions can be approximated, with no pertinent potential solution excluded. And these properties are generally sufficient for the approximation to converge to the exact solution as thed mesh becomes finer and the maximum element volume decreases [5.29, 5.42, 5.5, 5.6, 5.8].

Thus, the solution will be complete when the nodal values associated with each basis function are defined. In order to do so, it is convenient to frame the problem in the weak form of the partial different equation (1.9). The exact expression that the weak form takes

depends on the constitutive equations adopted, but the solution can always be put in the form

$$\boldsymbol{A}\tilde{\boldsymbol{u}} = \boldsymbol{b}. \tag{5.6}$$

The equation (5.6) is a linearization of the problem, such that $\tilde{\boldsymbol{u}}$ contains corrections to the increments of solution variables, if the problem is nonlinear. The components of $\boldsymbol{A}$ and $\boldsymbol{b}$ are determined by integration of the weak-form integrals, which in turn involve both the basis functions and their derivatives as well as the boundary conditions.

Fortunately, linear systems of equations are well researched, with many deeply studied computational solutions available [5.4, 5.13, 5.23]. With these highly-tuned algorithms on hand, helped by the fact that the matrix $\boldsymbol{A}$ is always sparse in Finite Element applications, very intricate bodies and meshes can be extensively examined within a reasonable timeframe.

Now, each basis function is typically broken up into shape functions ν, which are defined solely within one element, such that

$$N_i(\boldsymbol{X}) = \sum_j \nu_j^i(\boldsymbol{X}) \tag{5.7}$$

$$\nu_j^i(\boldsymbol{X}) = 0 \qquad\qquad \forall \boldsymbol{X} \notin \mathcal{E}_j \tag{5.8}$$

To make numerical integration (required to produce the linear system of equations) efficient to express algorithmically, the shape functions that comprise a basis function are usually not phrased as functions of physical coordinates. Instead, for the each shape function ν_j^i the coordinates are transformed according to the isoparametric mapping of element $\mathcal{E}_j$ onto a regular polyhedron of the same type. As such, tetrahedra and hexahedra are often chosen for having simple, straightforward isoparametric mappings and shape functions that produce accurate results. Even remaining within these two most popular element types there is a wealth of possible shape functions, although low-order polynomials are usually favored.

Low-order polynomials benefit from being uncomplicated, are often good approximations for the fields inside a body, and generally provide results that improve quickly under mesh refinement (avoiding Runge's phenomenon [5.34]). They are also useful for the small number points required by numerical integration to generate the system of linear equations, since they exhibit high quadrature efficiency [5.18].

Also, it's often useful to have a set of shape functions that are universal amongst elements after isoparametric mapping. This way, enforcing the Kronecker delta property (5.1) will also produce shape functions for a node that are continuous across element interfaces. Thus, continuous basis functions are produced, and in turn the entire approximate field solution will also be continuous within the body.

The Finite Element Method formulation briefly outlined here is an attractive method for continuum mechanics problems. Boundary conditions are easy to implement; only requiring the linear system of equations to be adjusted such that the boundary nodes to the specified value for essential boundaries. For a given amount of computational effort, a high degree of accuracy can be attained for incredibly complex body geometries. Moreover, a single algorithmic design can encompass all the processes needed for implementation.

While the Finite Element Method method has proven very successful in continuum mechanics, it suffers from some limitations in the realm of fracture mechanics. One major drawback is that the meshes required to implement the Finite Element Method are difficult to produce for bodies with complicated geometries. While automated mesh generation algorithms is a topic of continuing research [5.17, 5.30, 5.41], there is a dearth of existing methods that do not require minor or major human input for the level of complexity required in design. For a continuum mechanics discipline that centers on topology changes (e.g. fracture), the inability to fully automate the mesh generation required with every change in the body geometry can be crippling.

Many methods (particularly amongst cohesive zone implementations) only allow for crack propagation along existing element facets. However, this leads to mesh dependent crack

growth, where the mesh dependence is **not** lessened by creating a finer mesh [5.40]. Another approach is meshfree methods in order to provide greater flexibility when dealing with complicated or evolving geometry. These methods still must build a mesh-like structure to define the supports for efficient numerical integration, but they do provide relaxed conditions on the types of meshes allowed. However, the computational burden added by adopting a mesh-free method is significant, with complicated, time-intensive procedures required to build proper shape functions. In addition, meshfree methods generally exhibit quadrature efficiency that is far inferior to that of Finite Element methods.

In this dissertation, the benefits of the Finite Element Method are deemed great enough, but the cost of static meshes too great. So, a novel means for efficient fully-automated mesh generation will instead be pursued.

5.2   The Partitioned Element Method

One of the difficulties in preparing automatic mesh generation is the restriction that elements must take tetrahedral and/or hexahedral polyhedral form. These element types are exceedingly useful for the ease in which the shape functions can be generated. However, in order to ease automatic generation of meshes, having a variety of supplementary element constructions available is desirable. For this purpose, it is the goal of the Partitioned Element Method to allow general polyhedra to be incorporated in the computational mesh. For clarity, the Partitioned Element Method will be described in two dimensions, but the process can be extended to three dimensions.

Consider an arbitrary polygonal element that can be concave or non-simply connected, with its boundary formed by a collection of line segments. Traditionally, each node in the element has an associated shape function defined pointwise inside the element and on its boundary. But in the Partitioned Element Method the shape functions are not explicitly defined throughout the element, and instead are characterized discretely. To do this, the

element is broken into convex quadrature cells, with discrete information about each shape function defined for each cell. Intentionally, the shape function characterization is made with just enough detail to use in 'Finite Element Method'-like approximations of second-order variational boundary-value problems.

Consider an element $\mathcal{E}$ with N nodes that has been subdivided into Q convex quadrature cells $\mathcal{Q}^c$, where $Q \geq N$. Element integration points are defined as the cell centroids, and their weights are taken as the cell areas. For each quadrature cell, the shape functions ϕ^c and their gradients $\boldsymbol{g}^c$ are to be determined at the integration points without defining full functional forms for the shape functions.

The data given to a Partitioned Element Method element (as with traditional Finite Element Method elements) is a vector $\boldsymbol{u}$ of displacement values for each node. The Partitioned Element Method approach begins by applying the divergence theorem to each integration cell

$$|\mathcal{Q}^c|\,\boldsymbol{g}^c = \int_{\mathcal{Q}^c} \nabla\phi\,da \tag{5.9}$$

$$= \int_{\partial\mathcal{Q}^c} \phi\,\boldsymbol{n}\,ds. \tag{5.10}$$

The function ϕ is taken to be continuous and piecewise linear on $\partial\mathcal{E}$. Specifically, it is assumed to consist of one dimensional hat functions, as

$$\phi|_{\partial\mathcal{E}} = \sum_b u_b\psi_b \tag{5.11}$$

but is otherwise unknown. Here ψ_i is a continuous one dimensional hat function defined along the element boundary satisfying

$$\psi_i(\boldsymbol{X}_j) = \delta_{ij} \tag{5.12}$$

where $\boldsymbol{X}_j$ is the location of the jth node in the element.

Now, let $\partial \mathcal{E}$ be comprised of the set of line segments $\{\alpha_\gamma\}$. Further, let the set of line segments $\{\overline{\alpha}_{\overline{\gamma}}\}$ define the boundaries on the interior of $\partial \mathcal{E}$ that delineate the quadrature cells $\mathcal{Q}^c$. So, the boundary of each quadrature cell $\mathcal{Q}^c$ consists of some line segments from both sets as

$$\partial \mathcal{Q}^c = \left\{ \cup_{\gamma \in q^c} \, \alpha_{|\gamma|} \right\} \cup \left\{ \cup_{\overline{\gamma} \in \overline{q}^c} \, \overline{\alpha}_{\overline{\gamma}} \right\} \tag{5.13}$$

where q^c is a set of positive integers and $\overline{q}^c$ is a set of non-zero integers. The signs of $\overline{q}^c$ specify the sign adopted for unit normal associated with the indexed line segment. So, the unit normal vectors pointing in the out-of-cell direction of α_γ and $\overline{\alpha}_{\overline{\gamma}}$ are given as $\boldsymbol{n}^\gamma$ and $(\overline{\gamma}/|\overline{\gamma}|)\,\boldsymbol{n}^{\overline{\gamma}}$ respectively. The divergence theorem expression (5.10) can now be rewritten in a discrete manner as

$$|\mathcal{Q}^c|\,\boldsymbol{g}^c = \sum_{\gamma \in q^c} \Phi_\gamma \boldsymbol{n}^\gamma + \sum_{\overline{\gamma} \in \overline{q}^c} \frac{\overline{\gamma}}{|\overline{\gamma}|} \overline{\Phi}_{|\overline{\gamma}|} \overline{\boldsymbol{n}}^{|\overline{\gamma}|} \tag{5.14}$$

where the notations

$$\Phi = \int_{\alpha_\gamma} \phi ds \tag{5.15}$$

$$\overline{\Phi} = \int_{\alpha_{\overline{\gamma}}} \phi ds \tag{5.16}$$

have been adopted to help illustrate the discrete nature of the new expression.

Now, the expression (5.15) can also be phrased in terms of the nodal displacement values as

$$\Phi_\gamma = \boldsymbol{\Psi}_\gamma^T \boldsymbol{u} \tag{5.17}$$

where

$$\Psi_\gamma^T = \int_{\alpha_\gamma} [\psi_1, \ldots, \psi_N] \, ds \tag{5.18}$$

and ψ_i is a 1D hat function as in (5.12). So, all Φ_γ values are fully defined by the input displacement vector $\boldsymbol{u}$.

However, the $\overline{\Phi}_{\overline{\gamma}}$ values are still unknown, and can be used to enforce an optimal smoothness criterion. This criterion is chosen to be the minimization of the discrete form of the expression

$$\int_{\mathcal{E}} \nabla \phi \cdot \nabla \phi \, da \tag{5.19}$$

where $\phi|_{\partial \mathcal{E}}$ has been determined by the given nodal displacement input $\boldsymbol{u}$. From this minimization, integration point gradient values $\vec{\boldsymbol{g}}^c$ can be calculated.

Optimal smoothness provides the partition of unity property, where constant fields are exactly approximated. However, optimal smoothness does not generally satisfy linear approximability, where linear fields are exactly approximated. To correct this problem, a linear best-fit function $f = c + \boldsymbol{a}\boldsymbol{X}$ of the nodal data is generated by minimizing the expression

$$\sum_{\overline{\gamma}} |\overline{\alpha}_{\overline{\gamma}}| \left(\overline{f}_{\overline{\gamma}} - \overline{\Phi}_{\overline{\gamma}} \right)^2 \tag{5.20}$$

where

$$\overline{f}_{\overline{\gamma}} = \int_{\overline{\alpha}_{\overline{\gamma}}} f \, ds. \tag{5.21}$$

From the linear best-fit function a deviation vector $\tilde{\boldsymbol{u}}$ is defined, whose i^{th} nodal component

is

$$\tilde{\boldsymbol{u}}_i = \boldsymbol{u}_i - (c + \boldsymbol{a}\boldsymbol{X}_i) \tag{5.22}$$

where $\boldsymbol{X}_i$ is the position vector of the ith node. Then, the gradient values $\tilde{\boldsymbol{g}}^c$ associated with the deviation vector are used to determine the final integration point gradients as

$$\boldsymbol{g}^c = \vec{\boldsymbol{g}}^c + \tilde{\boldsymbol{g}}^c, \tag{5.23}$$

which ensures that the linear approximability property is achieved in the Partitioned Element Method.

Finally, the shape function values associated with each quadrature cell $\mathcal{Q}^c$ must be chosen. For this purpose an approximation function $\hat{\phi}$ is chosen to be

$$\hat{\phi} = \phi^c + \boldsymbol{g}^c \cdot (\boldsymbol{X} - \boldsymbol{X}^c) \tag{5.24}$$

where the gradient values are given by (5.23), $\boldsymbol{X}^c$ is an arbitrary fixed point inside $\mathcal{Q}^c$, and ϕ^c is a constant shape function value to be determined. For simplicity, the position vector of any node in the element that lies in the quadrature cell can be chosen for $\boldsymbol{X}^c$.

The shape function values ϕ^c are then chosen such that the decoupled functionals

$$\mathbb{J}^c = \int_{\partial \mathcal{Q}^c} \left(\hat{\phi} - \phi \right)^2 ds \tag{5.25}$$

are minimized, where ϕ is the same function as in (5.11). The function ϕ is known to be piecewise linear and continuous on the boundaries of all of the quadrature cells, but is otherwise unknown. By minimizing the functionals $\mathbb{J}^c$, the shape function values ϕ^c can be determined, and consequently the jump in the approximating function $\hat{\phi}$ across cell boundaries is minimized.

Through the F test of the F-E-M tests by Shi [5.35] (based on the Stummel generalized patch test [5.37]), it has been shown that minimizing the jump across cell boundaries is sufficient to enforce closedness. So, through minimizing the functionals $\mathbb{J}^c$ the Partitioned Element Method has the closedness property. Thus the Partitioned Element Method, like the Finite Element Method, has both the closedness and approximability properties and can be expected to converge to the exact solution as the discretization mesh becomes finer and the maximum element size decreases.

One benefit that the Partitioned Element Method holds over the Finite Element Method, is that it allows for a generalized algorithmic structure that can construct shape function and shape function gradient values for any polyhedral element with planar facets to be used in the computational mesh. The allowance for arbitrarily complex planar-faceted polyhedral elements grants more freedom when choosing elements to discretize a body, and eases the process of automating mesh generation. These are particularly valuable features for fracture problems where the shape and topology of the body are likely to change significantly. The Partitioned Element Method also strives to generate as little data as is necessary to generate an approximate solution, and promises an economy of stored data over the Finite Element Method when implemented. However, since no full implementation of the Partitioned Element Method is yet available, it is uncertain whether that promise will be fulfilled.

5.3   Half-Space Traversal Convex Subdivision

The key feature of the Partitioned Element Method formulation is that arbitrary polyhedral elements are allowed to form the computational mesh. However, a required step in the Partitioned Element Method is partition of the element into quadrature cells. Due to this requirement, concave and non-simply connected quadrature cells still prove difficult to incorporate when implementing numerical integration, even with the arbitrariness afforded by the Partitioned Element Method. So, a convex subdivision scheme called Half-Space Traversal

Convex Subdivision that forms multiple convex polyhedral quadrature cells out of a single concave polyhedral element input will now be outlined.

It will be assumed that the input element $\mathcal{E}$ for the Half-Space Traversal Convex Subdivision will be defined by F planar facets, S line segments, and N nodes. Each planar facet $\partial\mathcal{E}^i$ or $\mathcal{F}^i$ will in turn be defined by S^i line segments, N^i nodes, and a normal vector that points outside the input element. Finally, each line segment will be defined by two nodes, and will have two outward-facing normals defined, each pointing outside one of the facets of which the line segment is a part. For now non-simply connected elements will be left unaddressed by the Half-Space Traversal Convex Subdivision algorithm, but will be briefly discussed in Chapter 6.

In order to explain the convex subdivision algorithm it is important to first talk briefly about convex hulls. A robust convex hull algorithm is the backbone of the Half-Space Traversal Convex Subdivision algorithm. Fortunately, convex hulls have been thoroughly studied in computational geometry for years, and many viable algorithms for their construction are readily available [5.20, 5.22, 5.9, 5.1].
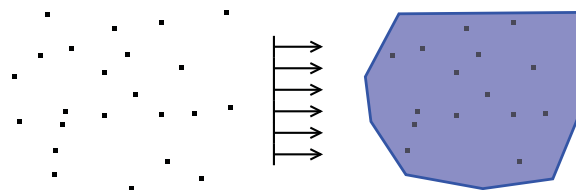

Fig. 5.2: A set of randomly place points (left), and the two dimensional convex hull in blue (right).

Given a set of points with an associated set of position vectors $\{\boldsymbol{X}\}$, the convex hull of those points is the minimal convex set that contains all points in the set (Fig. 5.2). A two dimensional convex hull of non-collinear points is thus a convex polygon whose boundary is composed of line segments, and a three dimensional convex hull of non-coplanar points will be a convex polyhedron whose boundary consists of planar facets. So, the convex hull found

from a given set of points can reasonably be expected to be permissible as a quadrature cell to be used in the Partitioned Element Method, so long as it lies entirely within the element.

In order to subdivide an input element $\mathcal{E}$ into quadrature cells, successive convex hulls will be created in a recursive manner. So, Half-Space Traversal Convex Subdivision concerns itself primarily with choosing nodes from $\mathcal{E}$ with which to create convex hulls. One benefit of this approach to convex subdivision is that it does not require any new nodes to be added to the input element in order to create its quadrature cells.

5.4   2D Convex Subdivision

The three dimensional form of Half-Space Traversal Convex Subdivision requires that all facets be convex, so before it begins, the two dimensional form must be applied to each facet. Thus, the discussion will begin with the two dimensional form of Half-Space Traversal Convex Subdivision as applied to one of the input element facets $\mathcal{F}$. In addition, many of the procedures and considerations required in two dimensions will have three dimensional analogs that will benefit from the clarity of visualization afforded in two dimensions.
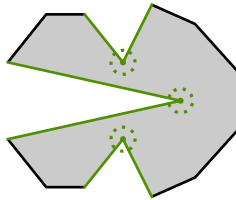

Fig. 5.3: An example input element facet with green dotted bullseyes placed on its reflex nodes, and all line segments in $\{\partial \mathcal{F}^r\}$ colored in green.

The first step in Half-Space Traversal Convex Subdivision is to find all reflex nodes in the facet and store them in the set $\{\mathcal{N}^r\}$. Reflex nodes are nodes which bound two line segments that have an inside angle greater than π. If no reflex nodes are found, then the facet must be convex, and no further calculations need to be performed. Next, create the

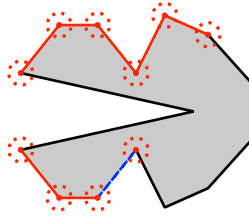set $\{\partial\mathcal{F}^r\}$ that contains all segments bounded by one and only one reflex node (Fig. 5.3).

Fig. 5.4: An example input element facet with the chosen line segment $\partial\mathcal{F}_i^r$ represented as a blue dashed line. All associated inside nodes have dotted red bullseyes placed on them, and all inside line segments in $\{\partial\mathcal{F}^n\}_i$ are colored in red.

Next, for each line segment $\partial\mathcal{F}_i^r$ in $\{\partial\mathcal{F}^r\}$, extend the line segment into a line such that the line divides the facet in two. All nodes that lie on the inside-the-facet side of, or on the dividing line formed from, $\partial\mathcal{F}_i^r$ are put into a set of inside nodes $\{\mathcal{N}^n\}_i$. Using this new set of nodes, a set of inside line segments $\{\partial\mathcal{F}^n\}_i$ is then created, containing all line segments that are bounded by two inside nodes (Fig. 5.4).
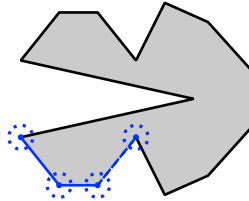

Fig. 5.5: An example input element facet with the chosen line segment $\partial\mathcal{F}_i^r$ represented as a blue dashed line. All line segments that will be placed in $\{\partial\mathcal{F}^t\}_i$ have been colored blue and all nodes that will be used to create a convex hull have been marked with dotted blue bullseyes.

Now, to choose which nodes will be selected for creating a convex hull, a new set of traversed line segments $\{\partial\mathcal{F}^t\}_i$ will be created. In the beginning, the traversed line segments set contains only the line segment $\partial\mathcal{F}_i^r$. Then, every line segment in $\{\partial\mathcal{F}^n\}_i$ that shares a

non-reflex bounding node with any segment in $\left\{\partial\mathcal{F}^t\right\}_i$ is added to the set of traversed line segments (Fig. 5.5); line segments are added in this manner until no new line segments can be added to the set of traversed line segments.
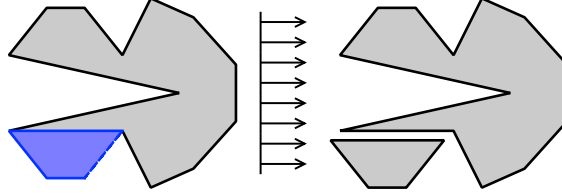

Fig. 5.6: An example input element facet with the chosen line segment $\partial\mathcal{F}_i^r$ represented as a blue dashed line, and the convex hull is represented in blue (left). The new facet produced by the convex hull and the remainder facet that will be input back into the Half-Space Traversal Convex Subdivision algorithm (right).

At this point the bounding nodes of all line segments in $\left\{\partial\mathcal{F}^t\right\}_i$ are used to generate a convex hull $\mathcal{H}_i$ (Fig. 5.6). If any inside node in $\left\{\mathcal{N}^n\right\}_i$ lies within the convex hull $\mathcal{H}_i$ then it must be discarded (Fig. 5.7). All remaining convex hulls can be graded by any criteria desired, then one convex hull is chosen to be recorded as a new element facet (or quadrature cell $\mathcal{Q}^c$ in the two dimensional Partitioned Element Method).
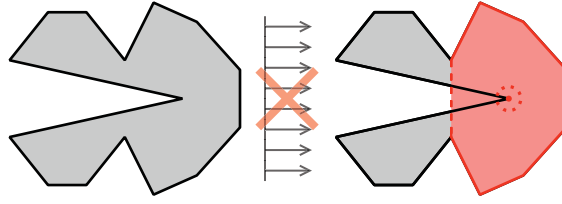
Fig. 5.7: On the left is an example input element facet, and on the right is a potential convex
           hull that is invalid for subdivision. The traversed line segments are colored red and the
           line segment created in order to construct the convex hull is represented as a dotted red
           line. The potential convex hull is rejected by the Half-Space Traversal Convex Subdivision
           algorithm for having an inside node, depicted with a dotted bullseye placed on it, that
           lies within the convex hull.

The selected convex hull is then subtracted from the input facet, resulting in a remainder
facet. The procedure begins again using the remainder as the new input element facet to be
"whittled down" using convex hulls. The algorithm stops when the remainder facet used as
a new input facet is found to be convex. This completes the 2D Half-Space Traversal Convex
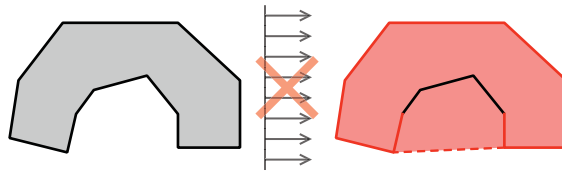Subdivision algorithm.

Fig. 5.8: On the left is an example input element facet, and on the right is a potential convex hull
          that is invalid for subdivision. The traversed line segments are colored red and the line
          segment created in order to construct the convex hull is represented as a dotted red line.
          The potential convex hull is avoided by the Half-Space Traversal Convex Subdivision
          algorithm by the construction of inside line segments used to create the traversed line
          segments set.

The Half-Space Traversal Convex Subdivision algorithm is constructed with the goal of creating as few convex hulls as possible for convex subdivision. For this purpose, the algorithm creates a convex hull that connects multiple reflex nodes when possible, removing these reflex nodes from the remainder facet. The generation of the inside line segments and the traversed line segments sets are designed to avoid constructing a convex hull that lies outside of the original input facet (Fig. 5.8). The final inside node check is provided to account for geometric features created by line segments disparate from the set of traversed line segments. Since all line segments are linear, the final check guarantees that no portion of the convex hull lies outside the input element facet.

Unfortunately , no validity proof is yet available for the two dimensional Half-Space Traversal Convex Subdivision algorithm. Instead, extensive case testing has been undertaken to search for simply-connected polygonal facets that the algorithm cannot subdivide; no such facets have been found yet (Fig. 5.9).
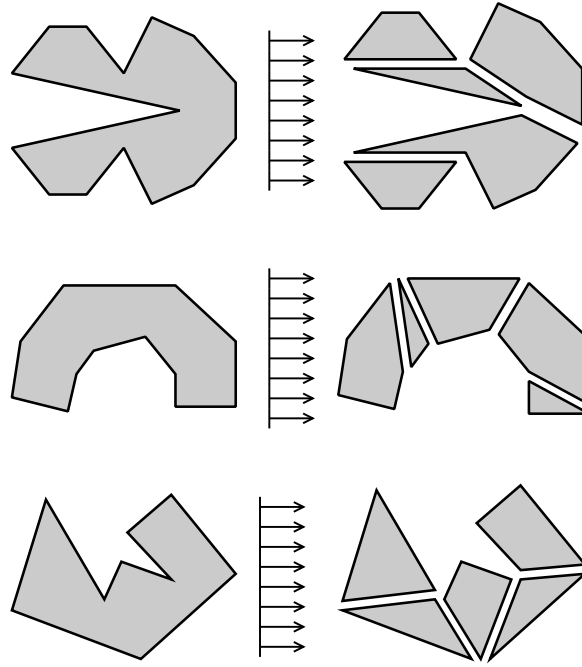
Fig. 5.9: On the left are example input element facets, and on the right are convex subdivisions produced by the 2D Half-Space Traversal Convex Subdivision algorithm. The particular convex hulls selected by the algorithm to form the convex subdivision were chosen at random.

5.5   3D Convex Subdivision

To support the three dimensional Partitioned Element Method, a three dimensional version of the Half-Space Traversal Convex Subdivision algorithm is needed. The three dimensional version of Half-Space Traversal Convex Subdivision bears many similarities to the two dimensional version. For variety of description, the three dimensional Half-Space Traversal Convex Subdivision algorithm is presented below as a step-by-step process.

   I Perform two dimensional Half-Space Traversal Convex Subdivision on all element facets of the input element $\mathcal{E}$. Replace each concave facet with the convex facets produced by the 2D Half-Space Traversal Convex Subdivision algorithm.

II Find all reflex line segments in the element, and store them in the set $\{\mathcal{S}^r\}$. Reflex line segments are line segments which bound two facets that have an inside angle greater than π. If no reflex line segments are found, then the element must be convex, and the algorithm may be exited.

III The set $\{\partial \mathcal{E}^r\}$ that contains all facets which are bounded by at least one reflex and one non-reflex line segment is constructed.

IV For each planar facet $\partial \mathcal{E}^r_i$ in $\{\partial \mathcal{E}^r\}$, extend the facet into a plane such that it divides the element in two. All line segments that have both of their bounding nodes lie on the inside-the-element side of, or on the dividing plane formed from, $\mathcal{S}^r_i$ will be put into a set of inside line segments $\{\mathcal{S}^n\}_i$.

V All facets that are bounded by inside line segments only will be placed into the inside facets set $\{\partial \mathcal{E}^n\}_i$.

VI A set of traversed facets $\{\partial \mathcal{E}^t\}_i$ is created, containing only the facet $\partial \mathcal{E}^r_i$.

VII Every facet in $\{\partial \mathcal{E}^n\}_i$ that shares a non-reflex bounding line segment with any facet in $\{\partial \mathcal{E}^t\}_i$ is added to the set of traversed line facets.

VIII Step VII is repeated until no new facets are added to the set of traversed facets.

IX Unfortunately the three dimensional nature of the problem allows for facets on both sides of a reflex line segment to be put into the set of traversed facets. This can happen when the two facets on either side of a reflex line segment are both inside facets, and share a neighboring inside facet. The first facet containing the reflex line segment could be put into the traversed facet set $\{\partial \mathcal{E}^t\}_i$, then the common neighbor would be put into $\{\partial \mathcal{E}^t\}_i$, and finally the second facet containing the reflex line segment would be put into $\{\partial \mathcal{E}^t\}_i$. A simple check must be performed to see if this has occurred.

X For every pair of facets $\partial \mathcal{E}_j^r$ and $\partial \mathcal{E}_k^r$ found in step IX that are bounded by the same reflex line segment and have been put into the set of traversed facets $\{\partial \mathcal{E}^t\}_i$, create two new sets of traversed facets through the intersections

$$\{\partial \mathcal{E}^t\}_{ij} = \{\partial \mathcal{E}^t\}_i \cap \{\partial \mathcal{E}^t\}_j \tag{5.26}$$

$$\{\partial \mathcal{E}^t\}_{ik} = \{\partial \mathcal{E}^t\}_i \cap \{\partial \mathcal{E}^t\}_k \tag{5.27}$$

and store the results as

$$\{\partial \mathcal{E}^t\}_i = \left\{ \{\partial \mathcal{E}^t\}_{ij}, \{\partial \mathcal{E}^t\}_{ik} \right\} \tag{5.28}$$

XI For every set inside $\{\partial \mathcal{E}^t\}_i$, the bounding nodes that comprise the boundary line segments of all facets are used to generated a convex hull $\mathcal{H}_i$. If any inside line segment in $\{\mathcal{S}^n\}_i$ lies within the convex hull $\mathcal{H}_i$ then it must be discarded.

XII All remaining convex hulls can be graded by any criteria desired so long as one convex hull is chosen to be recorded as a quadrature cell $\mathcal{Q}^c$.

XIII The selected convex hull is subtracted from the input facet, resulting in a remainder element.

XIV The procedure returns to step II using the remainder element constructed in step XIII as the new input element.

In order to construct as few divisions as possible when performing convex subdivision, the Half-Space Traversal Convex Subdivision algorithm creates a convex hull that connects multiple reflex segments when possible. By including reflex segments in the convex hull, they are removed from the remainder facet. The goal is to reduce the count of reflex segments in a polyhedron as quickly as possible to zero (i.e. full convex subdivision). The inside segment

check in step XI is provided to account for geometric features created by facets disparate from the set of traversed line segments. Since all facets are planar, the check in step XI guarantees that no portion of the convex hull lies outside the input element.

As in the two dimensional case, no validity proof is yet available for the three dimensional Half-Space Traversal Convex Subdivision algorithm. Further, the three dimensional form of the Half-Space Traversal Convex Subdivision relies on the two dimensional form, and accordingly the validity of the three dimensional form relies on the uncertain validity of the two dimensional form. Absent a rigorous proof, case testing has been undertaken to search for simply-connected polyhedral elements that the algorithm cannot subdivide; no such elements have yet been found (Fig. 5.10).

Of note, the convex pieces found by Half-Space Traversal Convex Subdivision are not intended to be the quadrature cells of an element. The convex pieces are to be further subdivided, by Voronoi tessellation with respect to the element's nodes, to make the quadrature cells for the Partitioned Element Method.
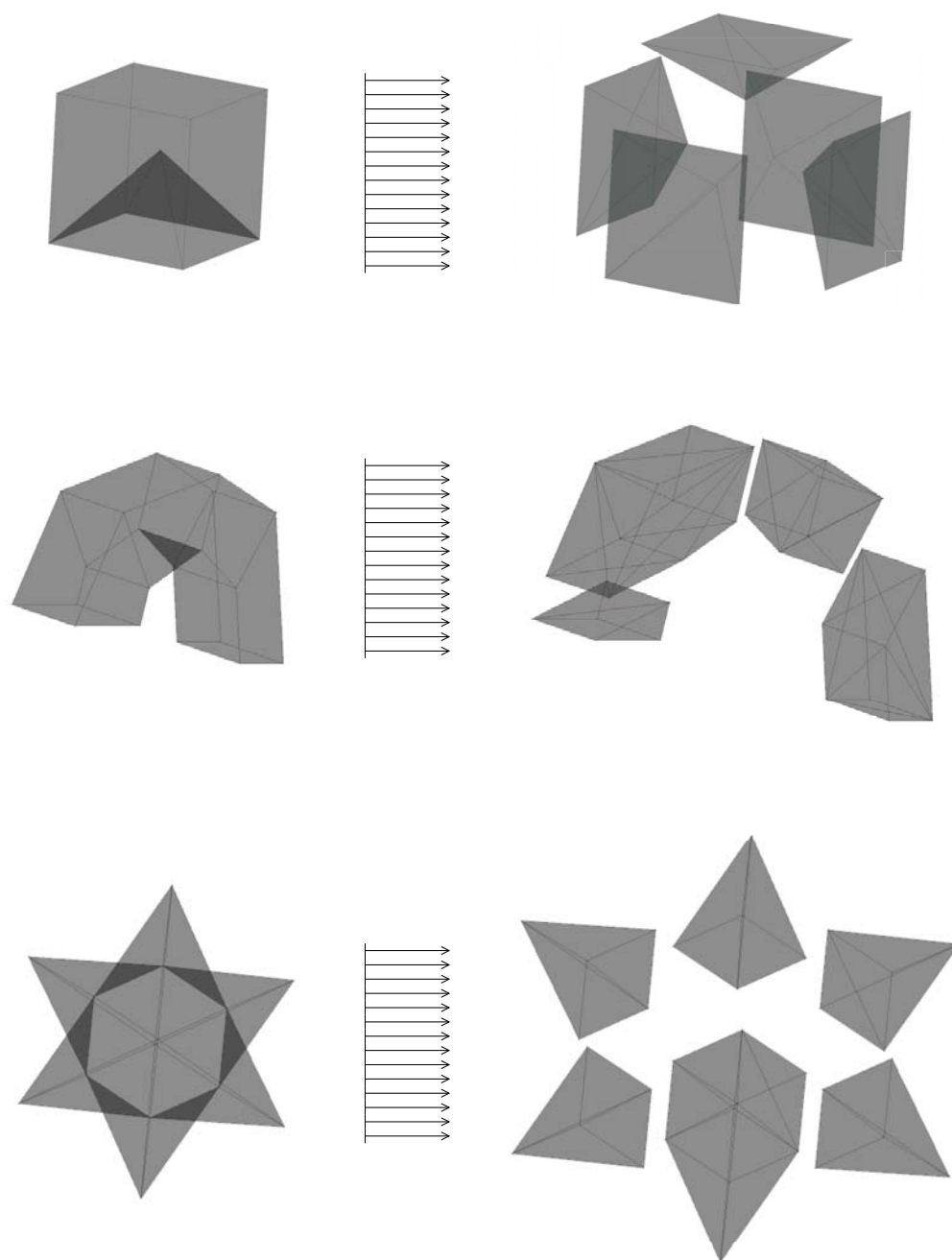
Fig. 5.10: On the left are example input elements, and on the right are quadrature cells produced by the 3D Half-Space Traversal Convex Subdivision algorithm. Both input elements and their quadrature cells are depicted as being translucent, so that the entire geometry is exposed. The convex hull construction algorithm implemented provided triangular bounding facets, and accordingly all quadrature cells are bounded as such. The particular convex hulls selected by the algorithm to form the quadrature cells were chosen at random.

Bibliography

[5.1] P. Afshani, J. Barbay, and T. M. Chan. Instance-optimal geometric algorithms. *2009 50th Annual IEEE Symposium on Foundations of Computer Science*, pages 129–138, 2009.

[5.2] B. J. Alder and T. E. Wainwright. Studies in molecular dynamics: I. general method. *The Journal of Chemical Physics*, 27:1208–1209, 1957.

[5.3] B. J. Alder and T. E. Wainwright. Phase transition for a hard sphere system. *The Journal of Chemical Physics*, 31:459–466, 1959.

[5.4] Anonymous. *Jiǔzhāng Suànshù (The Nine Chapters on the Mathematical Art)*, chapter Fang Cheng (The Rectangular Array). Han Dynasty, 179.

[5.5] I. Babuška. Error-bounds for finite element method. *Numerische Mathematik*, 16: 322–333, 1971.

[5.6] I. Babuška. The rate of convergence for the finite element method. *Society for Industrial and Applied Mathematics Journal on Numerical Analysis*, 8:304–315, 1971.

[5.7] I. Babuška, U. Banerjee, and J. E. Osborn. Survey of meshless and generalized finite element methods: A unified approach. *Acta Numerica*, 12:1–125, 2003.

[5.8] I. Babuška and B. Szabo. On the rates of convergence of the finite element method. *International Journal for Numerical Methods in Engineering*, 18:323–341, 1982.

[5.9] C. B. Barber, D. P. Dobkin, and H. Huhdanpaa. The quickhull algorithm for convex hulls. *Association For Computing Machinery Transactions On Mathematical Software*, 22:469–483, 1996.

[5.10] W. Barry and S. Saigal. A three-dimensional element-free galerkin elastic and elasto-plastic formulation. *International Journal for Numerical Methods in Engineering*, 46: 671–693, 1999.

[5.11] T. Belytschko, Y. Krongauz, D. Organ, M. Fleming, and P. Krysl. Meshless methods: An overview and recent developments. *Computer Methods in Applied Mechanics and Engineering*, 139:3–47, 1996.

[5.12] A. H.-D. Chenga and D. T. Cheng. Heritage and early history of the boundary element method. *Engineering Analysis with Boundary Elements*, 29:268–302, 2005.

[5.13] B.-I. Clasen. Sur une nouvelle méthode de résolution des Équations linéaires et sur l'application de cette méthode au calcul des déterminants (on a new method for solving linear equations with the application of the method of calculating determinants). *Annales de la Société Scientifique de Bruxelles (Annals of the Scientific Society of Brussels)*, 12:251–281, 1888.

[5.14] R. Courant. Variational methods for the solution of problems of equilibrium and vibrations. *Bulletin of the American Mathematical Society*, 49:1–23, 1943.

[5.15] J. Dolbow and T. Belytschko. Volumetric locking in the element free galerkin method. *International Journal for Numerical Methods in Engineering*, 46:925–942, 1999.

[5.16] C. A. Duarte and J. T. Oden. An h-p adaptive method using clouds. *Computer Methods in Applied Mechanics and Engineering*, 139:237–262, 1996.

[5.17] D. A. Field. The legacy of automatic mesh generation from solid modeling. *Computer-Aided Geometric Design*, 12:651–673, 1995.

[5.18] C. F. Gauss. Methodus nova integralium valores per approximationem inveniendi. *Commentationes Societatis Regiae Scientarium Gottingensis Recentiores*, 3:39–76, 1814.

[5.19] D. Gonzaález, E. Cueto, M. A. Martínez, and M. Doblaré. Numerical integration in natural neighbour galerkin methods. *International Journal for Numerical Methods in Engineering*, 60:2077–2104, 2004.

[5.20] R. L. Graham. An efficient algorithm for determining the convex hull of a finite planar set. *Information Processing Letters*, 1:132–133, 1972.

[5.21] K. K. Gupta and J. L. Meek. A brief history of the beginning of the finite element method. *International Journal for Numerical Methods in Engineering*, 39:3761–3774, 1996.

[5.22] R. A. Jarvis. On the identification of the convex hull of a finite set of points in the plane. *Information Processing Letters*, 2:18–21, 1973.

[5.23] W. Jordan. *Handbuch der Vermessungskunde.* J. B. Metzler Verlag, 3rd edition, 1888.

[5.24] F. W. Jr. An historical note on the finite element method. *International Journal for Numerical Methods in Engineering*, 15:930–934, 1980.

[5.25] P. Krysl and T. Belytschko. The element free galerkin method for dynamic propagation of arbitrary 3-d cracks. *International Journal for Numerical Methods in Engineering*, 44:767–800, 1999.

[5.26] S. Li and W.-K. Liu. Meshfree and particle methods and their applications. *Applied Mechanics Reviews*, 55:1–34, 2002.

[5.27] W.-K. Liu, S. Li, and T. Belytschko. Moving least-square reproducing kernel methods (i) methodology and convergence. *Computer Methods in Applied Mechanics and Engineering*, 143:113–154, 1997.

[5.28] N. I. Muskhelishvili. On the numerical solution of the plane problems of the theory of elasticity. *Trudy Tbilisskogo Matematicheskogo Instituta (Proceedings of Tbilisi Mathematical Institute)*, 1:83–87, 1937.

[5.29] L. A. Oganesjan. Convergence of difference schemes in case of improved approximation of the boundary. *Zhurnal Vychislitelnoi Matematiki i Matematicheskoi Fiziki (Computational Mathematics and Mathematical Physics)*, 6:1029–1042, 1966.

[5.30] S. J. Owen. A survey of unstructured mesh generation technology. *Proceedings of the 7Roundtable*, pages 239–267, 1998.

[5.31] A. Rahman. Correlations in the motion of atoms in liquid argon. *Physical Review*, 136:A405–A411, 1964.

[5.32] D. P. Recio, R. M. N. Jorge, and L. M. S. Dinis. Locking and hourglass phenomena in an element-free galerkin context- the b-bar method with stabilization and an enhanced strain method. *International Journal for Numerical Methods in Engineering*, 68:1329–1357, 2006.

[5.33] F. J. Rizzo. An integral equation approach to boundary value problems of classical elastostatics. *Quarterly of Applied Mathematics*, 25:83–95, 1967.

[5.34] C. Runge. Über empirische funktionen und die interpolation zwischen Äquidistanten ordinaten (about interpolation of empirical functions with equidistant ordinates). *Zeitschrift für Mathematik und Physik (Journal of Mathematics and Physics)*, 46:224–243, 1901.

[5.35] Z. C. Shi. The f-e-m test for convergence of nonconforming finite elements. *American Mathematical Society Mathematics of Computation*, 49:391–405, 1987.

[5.36] F. H. Stillinger and A. Rahman. Improved simulation of liquid water by molecular dynamics. *The Journal of Chemical Physics*, 60:1545–1557, 1974.

[5.37] F. Stummel. The generalized patch test. *Society for Industrial and Applied Mathematics Journal on Numerical Analysis*, 16:449–471, 1979.

[5.38] N. Sukumar, B. Moran, and T. Belytschko. The natural element method in solid mechanics. *International Journal for Numerical Methods in Engineering*, 43:839–887, 1998.

[5.39] N. Sukumar, B. Moran, A. Y. Semenov, and V. V. Belikov. Natural neighbour galerkin methods. *International Journal for Numerical Methods in Engineering*, 50:1–27, 2001.

[5.40] M. G. A. Tijssens, L. J. Sluys, and E. V. D. Giessen. Numerical simulation of quasi-brittle fracture using damaging cohesive surfaces. *European Journal of Mechanics A/Solids*, 19:761–779, 2000.

[5.41] M. Viceconti and F. Taddei. Automatic generation of finite element meshes from computed tomography data. *Critical Reviews in Biomedical Engineering*, 31:27–72, 2003.

[5.42] M. Zlámal. On the finite element method. *Numerische Mathematik*, 12:394–409, 1968.

Chapter 6

Future Work

THE novel fracture mechanics model and associated computational method discussed in this dissertation, the Continuum Geometric-Decohesion Model (Chapter 3) and the Partitioned Element Method (Section 5.2) are still in their infancy. And the Half-Space Traversal Convex Subdivision algorithm constructed in this dissertation (Sections 5.3-5.5) for use with the Partitioned Element Method is also in the early stages of development. As such, there isa great deal of work left that needs to be completed on model, method, and algorithm.

While the Continuum Geometric-Decohesion Model has been shown to be able to reproduce classical fracture mechanics models, its real strength lies in the unexplored paths in fracture mechanics it allows access to. There are a vast array of potential rupture criteria that should be considered, and promising candidates need be tested for viability against experimental results. The regularized stress and displacement field distributions produced by the geometry based closing tractions also need extensive comparisons against experimental results; both the results of different constitutive models and calibration parameters must be examined. Since the model allows for such great variety of exploration avenues, a system for rapid deployment and experimentation is desirable. For this purpose, numerical implementation of the Continuum Geometric-Decohesion model through the Partitioned Element

Method is ideal.

A complete implementation of the Partitioned Element Method, however, still lies in the future. Further work must be done to create efficient and robust methods for achieving each of the algorithmic steps required by the method. And, while the potential benefit of arbitrary polyhedral elements is important, it is also important that the computational performance of the Partitioned Element Method be compared extensively against existing other Finite Element Method based methods and meshfree methods.

The Half-Space Traversal Convex Subdivision algorithm is one component of the Partitioned Element Method that requires further algorithmic development. A modern convex hull algorithm implementation should be utilized for improved robustness and simplified quadrature cell geometry (e.g. combining coplanar triangular facets into larger convex polygonal facets). Further algorithmic development should be done on the rest of the current Half-Space Traversal Convex Subdivision implementation to improve robustness and efficiency. In particular, convex hull grading criteria that produce few, computationally effective quadrature cells must be found.

Regrettably, the author does not expect a proof or disproof of correctness will be forthcoming. A means for generating randomized concave three dimensional polyhedral should also be developed, such that many more, and more varied, test cases can be explored. In addition, the Half-Space Traversal Convex Subdivision algorithm should be extended to handle non-simply-connected polyhedral elements as well as concave elements.

Fortunately, non-simply-connected polyhedral elements can be recognized by creating groups of facets that each share a line segment with at least one other facet that resides in the same group. If more than one such group exists, the element must be non-simply-connected, and an inside-outside check can then be performed to find which group(s) of facets contain interior facets. An algorithm must be constructed in order to decide how the input element must be divided such that no more interior facets exist on the resultant polyhedra. A simple algorithm might cut the input element into two polyhedra using a dividing plane

that intersects at least two interior facets.

Clearly, there is a long journey ahead in the development of the aforementioned model, method, and algorithm. This dissertation represents only the first steps in their construction, but is intended that they have been represented in sufficient detail and with a level of completion sufficient to pique the interest of the reader. Still, it is the intention of the author to see model, method, and algorithm through to fruition.